공학박사학위논문

격자 볼츠만 법을 이용한 고분자 전해질막 연료전지의 기체확산층의 열 및 물질 전달 특성에 대한 수치해석

Numerical Analysis of Heat and Mass Transport Characteristics in Gas Diffusion Layer of Polymer Electrolyte Membrane Fuel Cell using Lattice Boltzmann Method

2023 년 2 월

서울대학교 대학원

기계항공공학부

이 승 훈

격자 볼츠만 법을 이용한 고분자 전해질막 연료전지의 기체확산층의 열 및 물질 전달 특성에 대한 수치해석

Numerical Analysis of Heat and Mass Transport Characteristics in Gas Diffusion Layer of Polymer Electrolyte Membrane Fuel Cell using Lattice Boltzmann Method

지도교수 김 찬 중

이 논문을 공학박사 학위논문으로 제출함

2022 년 10 월

서울대학교 대학원

기계항공공학부

이 승 훈

이승훈의 공학박사 학위논문을 인준함

2022 년 12 월

위 원 장 : 송 한 호 (인)

부위원장 : 김 찬 중 (인)

위 원 : 민 경 덕 (인)

위 원 : 남 진 현 (인)

위 원 : 김 형 민 (인)

Abstract

Numerical Analysis of Heat and Mass Transport Characteristics in Gas Diffusion Layer of Polymer Electrolyte Membrane Fuel Cell using Lattice Boltzmann Method

Seung-Hun Lee
Department of Mechanical and Aerospace Engineering
The Graduate School
Seoul National University

Polymer electrolyte membrane fuel cell (PEMFC) has the advantages of eco-friendliness, high efficiency, high power density, and relatively low operating temperature. These advantages make PEMFC the most promising alternative energy source for many applications, such as transportation, stationary power plants, and portable power. Research has been conducted to improve PEMFC performance over the past few decades, and it is essential to understand the electrochemical phenomena occurring in each cell component to improve cell performance and operate efficiently.

Since water vapor and heat generated by electrochemical reactions during cell operation escape to the gas channel (GC) through the gas diffusion layer (GDL), GDL is a crucial component that determines the performance of the PEMFC. Excessive liquid water floods the GDL and adversely affects PEMFC performance, and overheated temperature causes dehydration, resulting in performance degradation. Conversely, a dry condition lowers the efficiency of ion conductivity, and a lower temperature slows the reaction rate and lowers the saturation pressure, causing water vapor condensation. Thus, proper water and thermal management in the GDL are required to achieve better performance and efficiency of PEMFC.

In this dissertation, to analyze the mass transfer characteristics of GDL, the

invasion process of liquid water into GDL was investigated using the multicomponent multiphase (MCMP) lattice Boltzmann method (LBM). A three-dimensional (3D) structure regenerated by a stochastic reconstruction method was applied to consider the morphological characteristics of anisotropy GDL. The anisotropic characteristics of the reconstructed GDL were verified through permeability analysis. A total of four fiber polar angle ranges were adopted to investigate the effect of carbon fiber orientation on liquid water transportation, and the wettability of carbon fiber was assumed to be uniformly coated with a hydrophobic material, so a contact angle of 140° was applied.

The invasion pattern of liquid water showed capillary fingering flow due to the hydrophobic wettability. The dynamic behavior and average water saturation formed inside the GDL were almost similar in all conditions. Since the wettability and morphological conditions, except for the polar angle, were identical, it was identified that the preferential path formed during the liquid water transportation was more affected by the capillary pressure difference in the through-plane direction. In addition, the apparent angle of the liquid water droplet formed on the surface of the GDL after the liquid water broke through the GDL was measured. In all cases, it was observed that the apparent angle was formed lower than the contact angle applied to the carbon fiber, which was indicated as an effect of the surface variation of the GDL carbon fiber formed according to the fiber orientation.

Furthermore, in this dissertation, effective thermal conductivity (ETC) was investigated to understand the heat transfer characteristics of GDL, and the effect of liquid water content on ETC was also considered. The MCMP LBM model, in which the thermal and flow models were combined in two-way, was developed to conduct heat transfer and fluid flow simultaneously. The 3D GDL microstructure was also applied to the thermal model, and the dry and humidified conditions of the GDL were investigated, respectively. Additionally, a hydrophilic contact angle of 80° and a hydrophobic contact angle of 140° were applied under the humidified

condition.

This dissertation presented the temporal snapshot of the temperature distribution and the aggregation and separation of water components during heat conduction. It was confirmed that the ETC of GDL was greatly affected by the content and distribution of liquid water formed inside the GDL. In addition, the higher the initial water component mass fraction, the higher the liquid water content of GDL. It was observed that the liquid droplets act as a binder connecting the carbon fibers. Since the conductivity of liquid water is higher than that of air, it was identified that the more liquid water was distributed, the higher the ETC value. When the wettability of the carbon fibers was identical, the liquid water content inside the GDL was similar, and it was found that the distribution of liquid water played a more critical role in determining the ETC of GDL than the absolute liquid water content.

Finally, this dissertation applied the reconstructed 3D GDL structure considering the fiber orientation and well-represented the anisotropic GDL mass transfer, which could not be confirmed in the conventional 2D geometry. It suggests the importance of the morphological condition of the carbon fiber at the interface. In this dissertation, the phase change of the water component was not considered. However, the phase separation close to the almost identical phenomenon was included. Accordingly, the proposed model in this dissertation provides a framework that simultaneously performs thermal and phase segregation of fluids analysis in multicomponent, which could not be done in the existing MCMP LBM model.

Keywords : Polymer Electrolyte Membrane Fuel Cell (PEMFC); Gas Diffusion Layer (GDL); Lattice Boltzmann Method (LBM); Multicomponent Multiphase (MCMP) Model; Carbon Fiber Orientation; Liquid Water Transport; Effective Thermal Conductivity (ETC); Phase Segregation

Student Number: 2014-21840

Contents

List of Tables

List of Figures

Nomenclatures

A	area, m^2
c_s	speed of sound at lattice Boltzmann
c	lattice speed
$c_p,\ c_v$	specific heat, J kg^{-1} K^{-1}
C_{kc}	Kozeny-Carman constant
Ca	capillary number
d	mean fiber diameter, m
$\boldsymbol{e}$	lattice velocity
f	particle distribution function
f^{eq}	equilibrium distribution function
F	Faraday constant, 96,487 C mol^{-1}
$\boldsymbol{F}$	force
g	particle distribution for temperature
g^{eq}	equilibrium distribution function for temperature
$G_{\sigma\bar{\sigma}}$	coefficient of cohesion force
G_{adh}^{σ}	coefficient of adhesion force
$G_{\sigma\sigma}$	coefficient of interaction force
H_{fg}	latent heat of phase change, J kg^{-1}
j	current density, A m^{-1}
k	thermal conductivity, W m^{-1} K^{-1}
l	length, m
L	distance of temperature difference
m	lattice mass, kg
$\dot{m}_{H_20}$	interfacial phase change mass transfer rate, kg m^{-3} s^{-1}
M	dynamic viscosity ratio
M_{H_20}	molar mass of water, g mol^{-1}
$\dot{n}_{H_20}$	molar rate of water, mol s^{-1}
$\vec{p}$	position vector
P	pressure, Pa
∇P	pressure gradient

$\boldsymbol{q}$	heat flux, W m^{-2}
R	gas constant, 8.314 J mol^{-1}K^{-1} or droplet radius, m
Re	Reynolds number
s	wall function
S	phase transition source term
S_w	water saturation level
t	time, s
Δt	time step
T	temperature, K
ΔT	temperature difference along the heat flux direction
$\vec{u}$	orientation vector
$\bar{u}$	volume-averaged velocity, m s^{-1}
$\boldsymbol{u}$	physical velocity, m s^{-1}
$\boldsymbol{u}^{eq}$	equilibrium velocity
V_{GDL}	total lattice nodes of the GDL
W	width of droplet interface, m
Δx	lattice spacing
$\boldsymbol{x}$, $\boldsymbol{x}'$	particle position
x, y, z	3D coordinates

Greek letters

α	lattice direction or thermal diffusivity, m^2 s^{-1}
γ	surface tension, N m^{-1}
ε	porosity
σ, $\bar{\sigma}$	fluid component
θ	azimuthal angle, °
θ_c	contact angle, °
ρ	density, kg m^{-3}
κ	permeability
μ	dynamic viscosity, kg m^{-1} s^{-1}
ν	kinetic viscosity, m^2 s^{-1}

τ	relaxation time
ϕ	solid filler volume fraction
φ	potential function or polar angle, °
ψ	effective mass
ω	weight factor
ω_{ac}	acentric factor

Subscripts and superscripts

ac	accentric
adh	adhesion force
ap	apparent
avg	averaged value
c	critical value or capillary
coh	cohesion force
$cold$	cold temperature
e	equilibrium
eff	effective
eos	equation of state
eq	equilibrium
f	fluid
g	gas
GS	gas-solid
hot	hot temperature
i	component phase
in	inlet or inside of the droplet
int	interaction force
l	liquid or left
LB	lattice Boltzmann value
LG	liquid-gas
LS	liquid-solid
m	intermediate value

n	iteration number
out	outside of the droplet
phy	physical value
r	reduced value or right
s	solid
sat	saturation
0	initial value or center point
1	water component
2	air component
$+$	positive lattice direction
$-$	negative lattice direction

CHAPTER 1
INTRODUCTION

1.1 Polymer Electrolyte Membrane Fuel Cell

Growing concerns about global pollution and the depletion of energy sources have recently led to the development and research of clean and alternative energy sources. For many decades, fuel cells have been attracting attention as an eco-friendly next-generation energy source for carbon neutrality and the hydrogen economy due to their high performance and efficiency. As shown in Fig. 1.1, there are several types of fuel cells, such as Direct Methanol Fuel Cell (DMFC), Alkaline Fuel Cell (AFC), Phosphoric Acid Fuel Cell (PAFC), Molten Carbonate Fuel Cell (MCFC), Solid Oxide Fuel Cell (SOFC), and Polymer Electrolyte Membrane Fuel Cell (PEMFC). PEMFC has been considered one of the most promising power sources in many applications, such as automotive and stationary or portable power, due to its advantages, such as zero-emission, low operating temperature, high efficiency, and high power density (Wu et al., 2018).

PEMFC comprises a thin polymer electrolyte (PE) membrane with proton conductivity, as represented in Fig. 1.2. The hydrogen and oxygen are injected into the anode and cathode through the respective gas channel (GC) and penetrate the gas diffusion layer (GDL) of each electrode to the catalyst layer (CL). At the CL of the anode, the Hydrogen Oxidation Reaction (HOR) occurs in which hydrogen is oxidized and separated into hydrogen ions and electrons. Hydrogen ions move to the cathode through the PEM, whereas the electrons are conducted to the cathode through

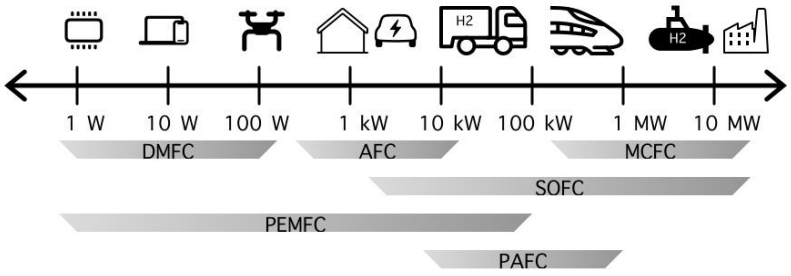

Fig.1.1. Applications and power spectrum by fuel cell type

an external electric circuit. The hydrogen ions and electrons then combine with oxygen in the CL of the cathode, which is called oxygen reduction reaction (ORR), and produces water vapor and heat as reactants (Bvumbe et al., 2016). The following electrochemical reaction equation expresses the overall reaction.

Anode (HOR): $H_2 \rightarrow 2H^+ + 2e^-$

Cathode (ORR): $\frac{1}{2}O_2 + 2H^+ + 2e^- \rightarrow H_2O$

Overall reaction: $\frac{1}{2}O_2 + H_2 \rightarrow H_2O + \text{heat} + \text{electicity}$ (1.1)

The water vapor is continuously generated as a result of the electrochemical reaction. The produced water vapor is liquefied over the saturation pressure and escapes into the GC through the GDL as a capillary flow. An adequate amount of liquid water is beneficial for the ion conductivities of PEM and maintains a reactive gas path from the GC to the CL. However, excessively accumulated water can block the porous channels of the CL and GDL, impeding the transport of reactants to the CL. This phenomenon, called "flooding," significantly contributes to PEMFC performance degradation (Kim et al., 2015).

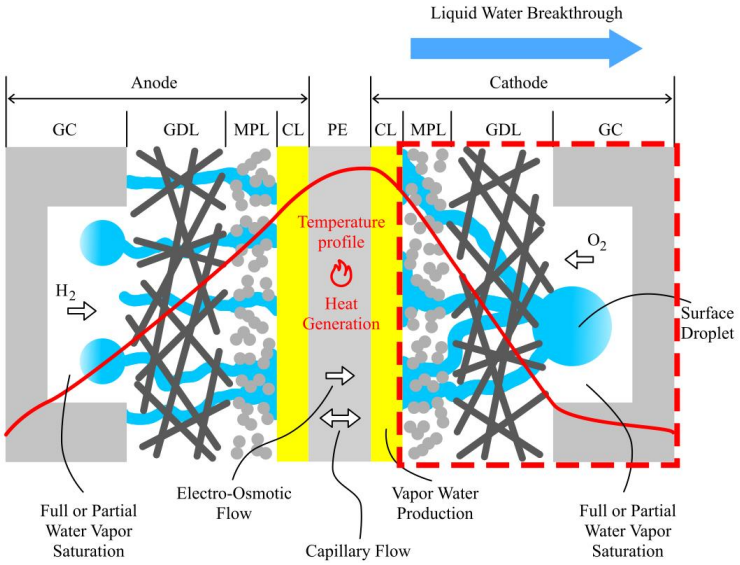

Fig.1.2. Schematic PEMFC components and heat and mass transportation

In addition, it is also essential to maintain an appropriate operating temperature to keep the GDL hydration (e.g., optimized liquid water saturation level, S_w). The temperature increases due to the electrochemical reaction, water phase changes, and ohmic heating, causing the GDL dryness and temperature gradients in a single cell and across the fuel cell stack (Hosseinzadeh et al., 2013; Sadeghifar et al., 2014; Bvumbe et al., 2016). Therefore, a comprehensive understanding of thermal management in GDL is critical to water management and enhancing and optimizing cell performance.

1.2 Backgrounds and Motivations

The GDLs are porous mediums usually composed of carbon fibers (paper or cloth). They are complicated microstructures with randomly distributed pore sizes and exhibit highly anisotropic properties. The pore morphology and wettability of the materials that make up the GDLs strongly influence the water management and mass transfer in the GDLs (Shojaeefard et al., 2016; Tayarani-Yoosefabadi et al., 2016; Fadzillah et al., 2017; Moqaddari et al., 2020). The heat transfer mechanism of GDLs is also very complicated because it has both solid (carbon fiber) and fluid (air/water) regions, and the pores formed by overlapping fibers are randomly distributed. Thermal processes in GDLs include heat conduction, convective heat transfer, and radiative heat transfer. Among them, thermal conductivity is the most crucial material property determining the thermal anisotropy characteristic of GDLs (Zamel et al., 2011; Li and Qu, 2015).

Several experimental studies have been conducted to investigate improving the water and thermal management of GDLs. Zenyuk et al. (2015) investigated the effects of geometric channel structure on the liquid water distribution in compressed GDLs using X-ray CT; they found that compression strongly influenced water distribution. They also tested the porosity and pore size distribution of commercial GDL materials at various compression ratios (Zenyuk et al., 2016). Shum et al. (2017) used synchrotron-based micro-CT to visualize and quantify water distribution inside a

GDL where a thermal gradient is applied. They demonstrated quantitative redistribution of water by plotting liquid water saturation as a function of through-plane distance.

Burheim et al. (2010) provided thermal conductivity and contact resistance under dry and humidified conditions. They found that the thermal contact resistance between carbon fibers was negligible compared to the contact resistance of the device. Teertstra et al. (2011) estimated the in-plane thermal conductivities of GDLs using a steady-state measurement method and considered the effect of polytetrafluoroethylene (PTFE) content. Sadeghifar et al. (2014) also studied the effect of PTFE, compression, and microporous layer (MPL) on thermal properties. They even developed a statistics-based mechanical model to predict the through-plane thermal conductivity of GDLs with PTFE treatment.

It is still challenging to examine various parameters affecting two-phase flow in GDL, even though liquid water transport in GDL has been conducted in several experimental types of research. In addition, it is difficult to directly control or measure a microporous medium with an experimental method due to the massive time consumption and the sensitivity to capture the impact of tiny microstructural changes. Furthermore, analytical and theoretical approaches also have restrictive application attributes to simplified and idealized morphological conditions.

Recently, the lattice Boltzmann method (LBM) has been developed due to its outstanding advantages in resolving complex fluid flows in porous materials at the microscale. It has also been successfully applied to study microporous media and composite materials' effective thermal conductivity (ETC). As a mesoscopic approach to fluid dynamics, LBM is more convenient, presents better performance, and requires less computational cost than other numerical methods and commercial tools. For example, Satjaritanun et al. (2017, 2018) used LBM combined with in-situ flow visualization to estimate the breakthrough pressure for GDL samples applied with MPL; they also studied the liquid water distribution, saturation, and breakthrough pressure inside the GDL, considering the rib-channel structures and single/multiple injection points. Niu et al. (2018) investigated the influence of the

compressive force on removing a water droplet from a GDL with an inter-digitated flow field; they further revealed that an optimum compression level exists for the fastest removal process.

Chen et al. (2010, 2012a, 2012b) considered the effect of GC's wettability on liquid water removal from GDL. They demonstrated that the liquid water accumulation in the GDL was more reduced under hydrophilic GCs than hydrophobic GCs. Moriyama and Inamuro (2011) utilized an arbitrarily generated porous media to investigate the effect of the hydrophobicity of the GDL on liquid water flooding. They applied the GDL composed of hydrophobic carbon fibers and the GC as a hydrophilic microscale duct. The above research demonstrated that liquid water saturation level in the GDL was generally reduced as a hydrophobicity of the GDL increased.

To make the GDL hydrophobic, the surface of the GDL is coated with a hydrophobic material such as PTFE. Molaeimanesh and Akbari (2014) reported the effects of varying PTFE distributions in a through-plane direction. They demonstrated that uniformly coated GDLs with PTFE could be accomplished effective water management. i.e., coating all carbon fibers inside the GDL is preferred to improve water management. Kakaee et al. (2018) showed the influence of PTFE distribution on liquid water removal from the GDL, which contained binders. They presented that adding binders with a specific PTFE distribution can effectively help fluid water drainage. However, achieving the uniform distribution of PTFE became more challenging as binder contents increased. Chen and Jiang (2016) demonstrated that liquid-gas flow in GDL and the relationship between relative permeability and phase saturation are significantly affected by the range and distribution of PTFE. Furthermore, Deng et al. (2019) studied the effects of spatial PTFE distribution by adding an MPL with various pressure differences between the inlet and outlet. They demonstrated that liquid water distribution in GDL significantly affects by PTFE drying treatments and liquid water stuck in the GDL near the MPL's macro cracks.

In terms of thermal management in GDL, Zhang and Zhang (2014) investigated the effective thermal conductivity and diffusion coefficient of a carbon-based GDL under different compressions, and the entire microstructures of the GDLs were obtained

using X-ray tomography. They showed material characteristics of both in-plane and through-plane directions and revealed the anisotropic of the GDLs. According to their results, the ETC of GDL increased more quickly in the through-plane direction than in the in-plane direction as the porosity decreased under compression. Wang et al. (2014) conducted the effects of the different particle sizes on the ETC of porous materials. They showed that increased particle size improves the connectivity of the particles along the heat flux direction and provides a preferential pathway for heat transfer, representing higher ETC.

Yablecki et al. (2012b) presented both in-plane and through-plane direction ETCs to reveal the anisotropic thermal properties of GDL. They used thermal LBM to explain the anisotropic thermal conductivity of GDL. They also used liquid water saturation patterns from the pore-network simulation to apply the effect of water content on thermal conductivity (Yablecki et al., 2012a). Lu et al. (2021) investigated the dependence of ETC on a 3D fibrous porous structure generated by a stochastic structural method. They were especially interested in the effect of two parameters (fiber diameter and orientation angle) on the ETC in a vacuum. Qin et al. (2020) also proposed a thermal LBM simulation and used the 3D fractal model results to compare with that. The proposed models revealed the relationship between heat transfer property and porosity and the thermal conductivity ratio of a solid to a fluid.

The LBM has been effectively used to study the water invasion patterns inside the GDL. However, little has been investigated about the effects of the anisotropic characteristics of GDL on water management in PEMFCs. Mass transportation, especially water management within PEMFCs, is affected by the structural properties of the GDL, including the alignment of carbon fibers. Among them, permeability is a crucial parameter for the characterization of fluid flow in the GDL. Due to variations in their manufacturing process, most GDLs are anisotropic, and their ability to lead a fluid in the through-plane and in-plane directions are different. (Hottinen et al., 2004). Several studies have demonstrated that PEMFC performance strongly depends on the in-plane permeability, especially in serpentine flow channels where crossflow occurs, owing to the pressure gradient between adjacent channels (Pharoah, 2005; Feser et

al., 2006; Inoue et al., 2006). However, previous studies on the effects of structural properties of GDLs on water management have not considered fiber orientation (fiber pitch) in the in-plane of the GDL by assuming that carbon fibers are parallel to the through-plane. Fiber pitch is defined by Hinebaugh and Bazylak (2017) as the angle between the fiber and the in-plane direction of the GDL material and describes the anisotropy of GDLs. Recently, a few studies considered the carbon paper anisotropy level in the thickness direction (Molaeimanesh and Akbari, 2014; Moqaddari et al., 2020; Nazemian and Molaeimanesh, 2020). However, to our knowledge, the study on the water invasion patterns visualized through the GDL with fibers aligned in the thickness direction has not been conducted so far.

In addition, most early studies did not consider the liquid water content when understanding and improving the thermal management of GDL. Even if they considered the water content, they brought or generated a steady-state water saturation distribution with reconstructed GDLs, instead of adopting the time-dependent dynamic behavior of saturated water vapor. In particular, the through-plane thermal conductivity of GDL is highly dependent on the water presence, and material properties (e.g., morphological condition and wettability of the GDL) influence the fluid flow characteristics. Therefore, it is necessary to investigate the effects of the water content under different conditions on the ETC of GDLs.

1.3 Thesis Outline

This thesis focuses on the morphological effects of GDL structures on the water invasion and heat transfer characteristics in GDL using the multicomponent multiphase (MCMP) LBM. Furthermore, it develops advanced MCMP LBM coupled with thermal LBM to investigate phase separation of non-ideal gas during the heat transfer in the GDL. It consists of five chapters, as described below.

Chapter 2 introduces a theoretical LBM model for MCMP fluid flow and conjugated heat transfer in GDL. This chapter explains the fundamental theories of a pseudopotential model with two different forcing schemes, Shan-Chen (SC) and

exact difference method (EDM) schemes. Furthermore, the Peng-Robinson equation of state (P-R EOS) for non-ideal gas will be introduced and adopted in the second scheme. Then, the second scheme is coupled with a thermal model considering pure conduction. The validity of the present models is proceeded by comparing with the theoretical models and experimental data at the beginning of each following chapter.

In Chapter 3, the numerical studies are conducted using the SC model in Chapter 2 to simulate the three-dimensional (3D) intrusion process of liquid water in the GDL. Considering the anisotropic characteristics of the GDL by applying the various fiber orientation ranges, the 3D GDL is reconstructed by the stochastic method, and the validity of the present 3D structures is conducted by estimating the permeability. The SC model introduced in Chapter 2 is used, and the cross-sectional average of the water saturation profile during water invasion in GDL pores is represented. It discusses the importance of morphological conditions, which are changed according to the arrangement of the fiber orientation.

In Chapter 4, the ETC of the 3D reconstructed GDL in Chapter 3 is predicted in dry and humidified conditions using the thermal LBM coupled with the EDM model in Chapter 2. Furthermore, the wettability of GDL, which affects the liquid water distribution in the GDL, is considered in humidified conditions. The predicted ETC is verified by comparing it with the theoretical ETC model and experimental data of uncompressed dry-condition GDLs. The numerical approach provides an alternative numerical analysis and a comprehensive understanding of the thermal and water management of the GDL. Finally, the conclusion of the present study and suggestions about future works are presented in Chapter 5.

CHAPTER 2.
LATTICE BOLTZMANN METHOD

In this chapter, it introduces the basic concept of the LBM model for multiphase flow and thermal LBM for heat transfer in the GDL. Two different forcing schemes, one is Shan and Chen's (SC) forcing scheme and the other is the exact difference method (EDM) scheme, are applied to deal with the interaction force between multicomponent and solid wall. The flow of phase separation of non-ideal gas at non-isothermal conditions is demonstrated by using the EDM forcing scheme. Finally, the boundary conditions for the MCMP and thermal models are introduced, and the unit parameters for converting the lattice scale to the physical scale are also presented in the last part.

2.1 Introduction

Many researchers have been interested in multiphase flow in natural phenomena and industrial processes such as chemical, electronic, and power generation industries. Simulating the behavior of multiphase flows is very difficult due to the inherent complexity of the phenomena associated with multiphase flows (Li et al., 2012).

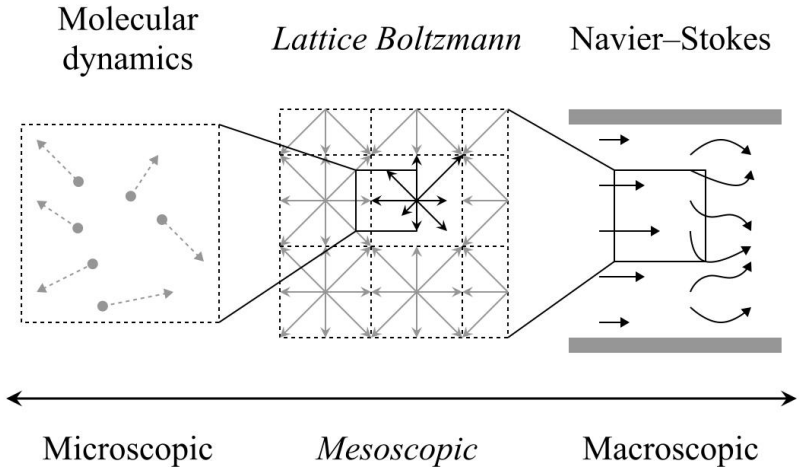

Fig.2.1. The numerical scale of the LBM simulation

There is always an MCMP form of water vapor or liquid water and air in the GDLs pores, even in the PEMFC operation. Therefore, it is necessary to develop a suitable MCMP model to investigate the interior of the GDLs.

The LBM has been developed over the past two decades. The LBM is a numerical method based on the mesoscopic kinetic theory and Boltzmann equations. The LBM is an appreciative CFD method suitable for flow simulations with complex boundaries and complicated multiphase dynamics. In general conventional CFD, the Navier-Stokes equations are used to solve continuity; on the other hand, the LBM solves the discretized Boltzmann equations in a lattice for fluid flow, as described in Fig. 2.1.

The LBM schemes are classified as a function of the spatial dimensions (n) and the number of distribution functions (b), each notated as DnQb. As shown in Fig. 2.2, two spatial dimensions and nine distribution functions (i.e., D2Q9) and three spatial dimensions and nineteen distribution functions (i.e., D3Q19) are most generally used as each dimensional solution. Streaming and collision procedures represent the main processes in the LBM and are described by distribution functions representing the probability of finding a fluid particle (Mohamad, 2011). At each node in the fluid domain, the distribution functions are given in different directions, and they move to a neighboring node with a discrete direction in the streaming procedure. Eventually, all probability distribution function streamed to each direction is collected and

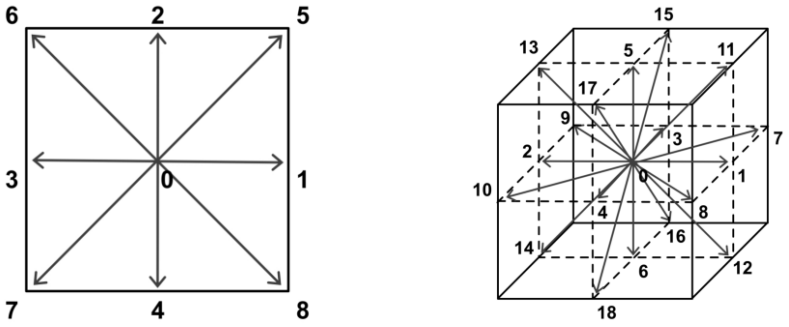

(a) D2Q9 (b) D3Q19

Fig.2.2. Schematic of representative 2D and 3D LBM schemes

converged at each node. This process is referred to as the collision procedure. The above processes are conducted explicitly and continuously at all steps of the LBM procedure and describe the kinetic nature of a system of fluid particles.

Several LBMs have been developed to simulate MCMP flows. The most widely used approaches include the color-gradient model proposed by Gunstensen et al. (1991), the pseudopotential model proposed by Shan and Chen (1993), and the free-energy model proposed by Swift et al. (1996). Among these models, the pseudopotential LB model is widely used for multiphase flow owing to its simplicity and versatility.

In the pseudopotential model, the motion of a fluid is described by a set of the discrete single-particle density distribution function, and for multicomponent, the double distribution function (DDF) is set for each component, σ (where σ = 1, 2, 3, …). With the BGK (Bhatnagar–Gross–Krook) collision operation, the discretized LB equation for each component is expressed as follows (He and Luo, 1997; Chen and Doolen, 1998):

$$f_\alpha^\sigma(\boldsymbol{x}+\boldsymbol{e}_\alpha\Delta t, t+\Delta t) - f_\alpha^\sigma(\boldsymbol{x},t) = -\frac{\Delta t}{\tau^\sigma}\left[f_\alpha^\sigma(\boldsymbol{x},t) - f_\alpha^{\sigma,eq}(\boldsymbol{x},t)\right] + \Delta t \boldsymbol{F}_\alpha^\sigma \quad (2.1)$$

where $f_\alpha^\sigma(\boldsymbol{x},t)$ is the particle distribution function (PDF) in the α lattice direction of the σth component, $\boldsymbol{x}$ is particle position, and t is time. τ^σ is the relaxation time of the σth component. It represents the elementary time of the collision procedure and is related to its viscosity such that, $\nu^\sigma = c_s^2(\tau^\sigma - 0.5)\Delta t$. c_s represents the speed of sound at the LB nodes, and it is given by $c_s = c/\sqrt{3}$ in the D2Q9 and D3Q19 models, where $c = \Delta x/\Delta t$ is the lattice speed calculated by lattice spacing and time step. Here, one lattice unit Δx is defined as 1 lu, and one time step Δt defined as 1 ts. $\boldsymbol{F}_\alpha^\sigma$ is the external force term acting on the σth component. $\boldsymbol{e}_\alpha$ denotes the velocity in the α lattice direction, and each velocity for D2Q9 and D3Q19 is defined as follows:

$$\boldsymbol{e}_\alpha = \begin{cases} (0,\ 0), & \alpha = 0; \\ (\pm 1,\ 0),\quad (0,\ \pm 1), & \alpha = 1-4; \\ (\pm 1, \pm 1), & \alpha = 5-8; \end{cases} \quad (2.2a)$$

and

$$\boldsymbol{e}_\alpha = \begin{cases} (0,\ 0,\ 0), & & & \alpha = 0; \\ (\pm 1,\ 0,\ 0), & (0,\ \pm 1,\ 0), & (0,\ 0,\ \pm 1), & \alpha = 1-6; \\ (\pm 1, \pm 1, 0), & (\pm 1, 0, \pm 1), & (0, \pm 1, \pm 1), & \alpha = 7-18; \end{cases} \tag{2.2b}$$

The collision process in the BGK collision scheme relaxes the PDF to an equilibrium distribution function, $f_\alpha^{\sigma,eq}$, which is described as

$$f_\alpha^{\sigma,eq} = \omega_\alpha \rho^\sigma \left[1 + \frac{\boldsymbol{e}_\alpha \cdot \boldsymbol{u}^\sigma}{c_s^2} + \frac{1}{2}\left(\frac{(\boldsymbol{e}_\alpha \cdot \boldsymbol{u}^\sigma)^2}{c_s^4} - \frac{\boldsymbol{u}^\sigma \cdot \boldsymbol{u}^\sigma}{c_s^2}\right)\right] \tag{2.3}$$

where ω_α is the weight factor for direction α and is defined for D2Q9 and D3Q19 as below:

$$\omega_\alpha = \begin{cases} 4/9, & \alpha = 0; \\ 1/9, & \alpha = 1-4; \\ 1/36, & \alpha = 5-8; \end{cases} \tag{2.4a}$$

and

$$\omega_\alpha = \begin{cases} 1/3, & \alpha = 0; \\ 1/18, & \alpha = 1-6; \\ 1/36, & \alpha = 7-18; \end{cases} \tag{2.4b}$$

The macroscopic values of Eq. (2.3) for each component, such as density, ρ^σ, and velocity, $\boldsymbol{u}^\sigma$ for $\boldsymbol{F}_\alpha^\sigma = 0$, can be obtained from f_a using the followin g equations:

$$\rho^\sigma = \sum_a f_a^\sigma \tag{2.5}$$

$$\boldsymbol{u}^\sigma = \frac{1}{\rho^\sigma} \sum_a f_a^\sigma \boldsymbol{e}_a \tag{2.6}$$

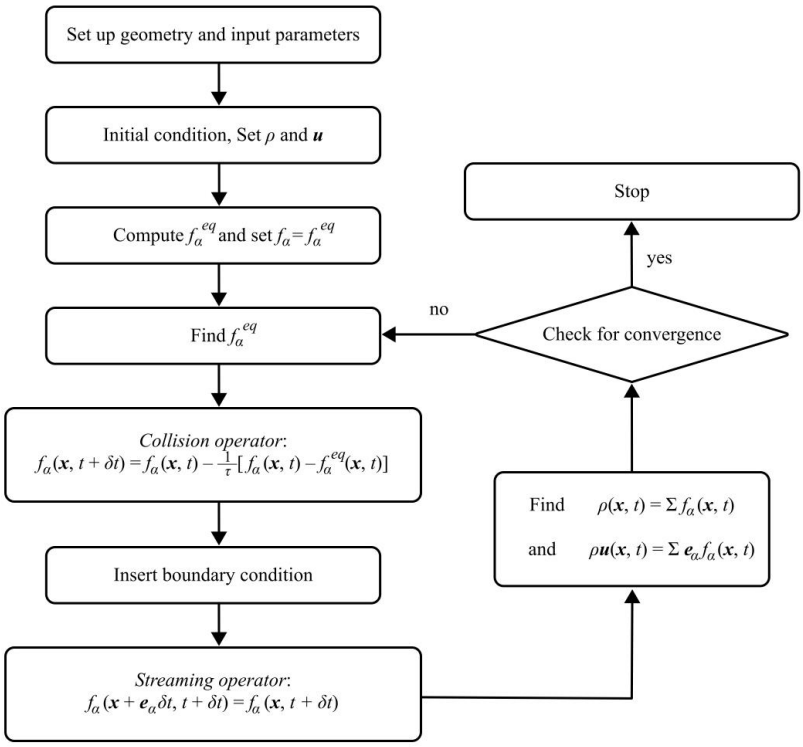

Fig.2.3. A flow diagram of the LBM

2.2 Shan-Chen and EDM Forcing Schemes

To mimic the external force, $\boldsymbol{F}_\alpha^\sigma$ in the incompressible Navier–Stokes equations, two different forcing schemes are adopted in this study. The first one is the Shan-Chen scheme, which was proposed by Shan and Chen (1993). This scheme is the concept of the shift velocity model, which is the external force acts on the velocity in the equilibrium distribution function, and the discretized LB equation for each component is given by

$$f_\alpha^\sigma(\boldsymbol{x} + \boldsymbol{e}_\alpha \Delta t, t + \Delta t) - f_\alpha^\sigma(\boldsymbol{x}, t) = -\frac{\Delta t}{\tau^\sigma}\left[f_\alpha^\sigma(\boldsymbol{x}, t) - f_\alpha^{\sigma,eq}(\rho^\sigma, \boldsymbol{u}^{\sigma,eq})\right] \quad (2.1a)$$

The shifted equilibrium velocity of the σth component, $\boldsymbol{u}^{\sigma,eq}$ is calculated by considering the momentum change rate due to the external forces, and it is described as

$$\boldsymbol{u}^{\sigma,eq} = \frac{\sum_\sigma \sum_a f_a^\sigma \boldsymbol{e}_a}{\rho^\sigma \sum_\sigma \sum_a \frac{1}{\tau^\sigma} f_a^\sigma} + \frac{\tau^\sigma}{\rho^\sigma} \sum \boldsymbol{F}^\sigma \tag{2.7}$$

In Eq. (2.7), the first term of the right-hand side represents the common velocity for all components of the multicomponent model, and the second term indicates the total force acting on each component. In the SC model, the total force includes the fluid/fluid and fluid/solid interaction forces, $\sum \boldsymbol{F}^\sigma = \boldsymbol{F}^\sigma_{cohesion} + \boldsymbol{F}^\sigma_{adhesion}$.

The exact difference method (EDM) was recently developed by Kupershtokh and Medvedev (2006). In this scheme, the external force term in Eq. (2.1) is directly discretized as a disturbance in PDFs and leads to the following modified form of the discrete LB equation:

$$f_\alpha^\sigma(\boldsymbol{x} + \boldsymbol{e}_\alpha \Delta t, t + \Delta t) - f_\alpha^\sigma(\boldsymbol{x}, t)$$

$$= -\frac{\Delta t}{\tau^\sigma}\left[f_\alpha^\sigma(\boldsymbol{x}, t) - f_\alpha^{\sigma,eq}(\rho^\sigma, \boldsymbol{u}^{\sigma,eq})\right] + \Delta f_\alpha^\sigma \tag{2.1b}$$

where,

$$\Delta f_\alpha^\sigma = f_\alpha^{\sigma,eq}(\rho^\sigma, \boldsymbol{u}^{\sigma,eq} + \Delta \boldsymbol{u}) - f_\alpha^{\sigma,eq}(\rho^\sigma, \boldsymbol{u}^{\sigma,eq}) \tag{2.8}$$

and,

$$\Delta \boldsymbol{u} = \sum \boldsymbol{F}^\sigma \, \Delta t / \rho^\sigma \tag{2.9}$$

In contrast to the SC model, the equilibrium velocity of the σth component, $\boldsymbol{u}^{\sigma,eq}$ is calculated by the common velocity for all components, $\boldsymbol{u}^{\sigma,eq} = \sum_\sigma \sum_a f_a^\sigma \boldsymbol{e}_a / \rho^\sigma \sum_\sigma \sum_a (f_a^\sigma / \tau^\sigma)$. The physical fluid velocity is redefined by averaging the momentum before and after the collision as below (Ikeda et al., 2014; Zhu et al., 2017)

$$\boldsymbol{u}^{\sigma,real} = \frac{1}{\rho^\sigma} \sum_\alpha f_\alpha^\sigma \boldsymbol{e}_\alpha + \frac{\sum \boldsymbol{F}^\sigma \Delta t}{2\rho^\sigma} \tag{2.10}$$

The EDM forcing scheme can easily apply additional external force terms in PDFs. The total force of the EDM model includes the interparticle force, $\boldsymbol{F}^\sigma_{interparticle}$ in addition to the existing total force of the SC model.

2.2.1 Total interaction forces

Any number of forces can be easily summed to determine the total force acting on a given particle within the system:

$$\sum \boldsymbol{F}^{\sigma} = \boldsymbol{F}^{\sigma}_{cohesion} + \boldsymbol{F}^{\sigma}_{adhesion} + \boldsymbol{F}^{\sigma}_{interparticle} \tag{2.11}$$

As mentioned earlier, the SC model considers only the first two terms, and the EDM model applies all three force terms in Eq. (2.11). $\boldsymbol{F}^{\sigma}_{cohesion}$ represents the interaction force with other components, $\boldsymbol{F}^{\sigma}_{adhesion}$ is the force interacting on the wall surface and each component, and $\boldsymbol{F}^{\sigma}_{interparticle}$ is the interaction force on a component surrounding the same component.

$$\boldsymbol{F}^{\sigma}_{cohesion} = -\varphi^{\sigma}(\boldsymbol{x}) \sum_{\bar{\sigma}} G_{\sigma\bar{\sigma}} \sum_{\alpha} \omega_{\alpha} \varphi^{\bar{\sigma}}(\boldsymbol{x} + \boldsymbol{e}_{\alpha}\Delta t)\boldsymbol{e}_{\alpha} \tag{2.12}$$

$$\boldsymbol{F}^{\sigma}_{adhesion} = -\varphi^{\sigma}(\boldsymbol{x}) \sum_{\alpha} G^{\sigma}_{adh} \omega_{\alpha} s(\boldsymbol{x} + \boldsymbol{e}_{\alpha}\Delta t)\boldsymbol{e}_{\alpha} \tag{2.13}$$

$$\boldsymbol{F}^{\sigma}_{interparticle} = -\psi^{\sigma}(\boldsymbol{x}) \sum_{\sigma} G_{\sigma\sigma} \sum_{\alpha} \omega_{\alpha} \psi^{\sigma}(\boldsymbol{x} + \boldsymbol{e}_{\alpha}\Delta t)\boldsymbol{e}_{\alpha} \tag{2.14}$$

In Eqs. (2.12) and (2.13), φ^{σ} and $\varphi^{\bar{\sigma}}$ are the potential function of particle interactions, and it can be set as the density function, $\varphi^{\sigma} = \rho^{\sigma}$ in multiphase LB models (Shan and Chen, 1993, 1994; Kupershtokh and Medvedev, 2006). $G_{\sigma\bar{\sigma}}$ is the coefficient of Green's function, which expresses the interaction between the σth component located at $\boldsymbol{x}$ and the $\bar{\sigma}$th component located at $\boldsymbol{x}'$, and it controls the strength of nearest particle interactions as follows:

$$G_{\sigma\bar{\sigma}}(\boldsymbol{x}, \boldsymbol{x}') = \begin{cases} 0, & |\boldsymbol{x} - \boldsymbol{x}'| > |\boldsymbol{e}_{\alpha}| \\ G_{\sigma\bar{\sigma}}, & |\boldsymbol{x} - \boldsymbol{x}'| = |\boldsymbol{e}_{\alpha}| \\ G_{\sigma\bar{\sigma}}/2, & |\boldsymbol{x} - \boldsymbol{x}'| = |\boldsymbol{e}_{\alpha}|\sqrt{2} \end{cases} \tag{2.15}$$

For the two components system considered in this study, the first one (σ = 1) represents the water component and the second component (σ = 2) means air, respectively. The coefficient values G_{12} and G_{21} are set to the same value to apply equal force between the components. -1 for the SC model and 0.002 for the EDM model are used, respectively. In Eq. (2.13), G^{σ}_{adh} is the parameter that tunes the adhesion of the σth component to a solid wall; that is, it controls the wettability of

the wall surface. $s(\boldsymbol{x}+\boldsymbol{e}_\alpha \Delta t)$ in Eq. (2.13) is the wall indicator function representing fluid nodes (s = 0) or solid nodes (s = 1) of the lattice. The value of G_{adh}^{σ} will be discussed and validated in the next part.

$\psi^{\sigma}(\boldsymbol{x})$ in Eq. (2.14) differs from φ^{σ} in Eq. (2.12) and is the pseudopotential function representing the "effective mass," $G_{\sigma\sigma}$ is the strength coefficient of the interaction (Li et al., 2017; Zhang et al., 2020). The interaction force of the air component is ignored due to the characteristics of the ideal gas. That is, the phase change and separation of the air component are not considered, and the coefficient is set to $G_{22} = 0$ (Zhang et al., 2017; Zhu et al., 2017; Zhang et al., 2020). For the water component, $\psi^{\sigma}(\boldsymbol{x})$ can be calculated after the non-ideal gas equation of state (EOS) as expressed by

$$\psi^{\sigma}(\rho^{\sigma}) = \sqrt{\frac{2(P_{eos}^{\sigma} - \rho^{\sigma} c_s^2)}{G_{\sigma\sigma} c_s^2}} \tag{2.16}$$

It follows that G_{11} is canceled when Eq. (2.16) is replaced by Eq. (2.14). Therefore, we set $G_{11} = -1$ to ensure the inner square root of Eq. (2.16) is a positive value. For the EOS for the non-ideal gas, the Peng-Robinson (P-R) EOS is adopted in this study to increase the density ratio between different components and improve the thermal consistency.

$$P_{eos} = \frac{\rho RT}{1 - b\rho} - \frac{a\rho^2 \alpha(T)}{1 + 2b\rho - b^2\rho^2} \tag{2.17}$$

$$\text{with} \quad a = \frac{0.457235 R^2 T_c^2}{P_c}, \; b = \frac{0.077796 R T_c}{P_c}, \tag{2.18}$$

Table 2.1. The coefficient values of the cohesion and interparticle forces for the SC and EDM models

Type	G_{11}	G_{12}, G_{21}	G_{22}
SC	-	-1	-
EDM	-1	0.002	0

where, 1: water component, 2: air component

$$\alpha(T) = \left[1 + (0.37464 + 1.54226\omega_{ac} - 0.26992{\omega_{ac}}^2) \times \left(1 - \sqrt{T/T_c}\right)\right]^2 \quad (2.19)$$

where R is the gas constant, P_c and T_c are critical values, and ω_{ac} is the acentric factor. In this model, we choose $a = 2/49$, $b = 2/21$, $R = 1$, and $\omega_{ac} = 0.344$ for the water component.

A brief comparison of the two forcing schemes described so far shows that the SC and EDM models differ in applying the external force term. In the case of the SC model, an external force is applied in the form of a shifted equilibrium velocity. In the EDM model, the external force is directly applied through the discretized form in PDFs. Therefore, it takes a different form when calculating the equilibrium velocity of each PDF.

The SC model applies cohesion and adhesion to account for fluid surface tension and contact angle at the solid wall. The density and viscosity ratios are assumed as 1 in the SC model. As mentioned before, the liquid water flows through the GDL as a capillary flow, and the density and viscosity ratios of the injected and displaced fluids (i.e., liquid water and air) are negligible compared to the capillary force (Kim et al.,

Table 2.2. The comparison of the SC and EDM models

Type	SC	EDM
Equilibrium velocity, $\boldsymbol{u}^{\sigma,eq}$	$\frac{\sum_\sigma \sum_a f_a^\sigma \boldsymbol{e}_a}{\rho^\sigma \sum_\sigma \sum_a \frac{1}{\tau^\sigma} f_a^\sigma} + \frac{\tau^\sigma \Delta t}{\rho^\sigma} \boldsymbol{F}^\sigma$	$\frac{\sum_\sigma \sum_a f_a^\sigma \boldsymbol{e}_a}{\rho^\sigma \sum_\sigma \sum_a \frac{1}{\tau^\sigma} f_a^\sigma}$
Physical velocity, $\boldsymbol{u}^\sigma$	$\frac{1}{\rho^\sigma} \sum_a f_a^\sigma \boldsymbol{e}_a$	$\frac{1}{\rho^\sigma} \sum_a f_a^\sigma \boldsymbol{e}_a + \frac{\boldsymbol{F}^\sigma \Delta t}{2\rho^\sigma}$
Total force, $\sum \boldsymbol{F}^\sigma$	$\boldsymbol{F}_{coh}^\sigma + \boldsymbol{F}_{adh}^\sigma$	$\boldsymbol{F}_{coh}^\sigma + \boldsymbol{F}_{adh}^\sigma + \boldsymbol{F}_{int}^\sigma$
Potential function, φ^σ	ρ^σ	
Effective mass, ψ^σ	Ideal gas	non-ideal gas / P-R EOS
Relaxation time, τ^σ	$\nu^\sigma = c_s^2(\tau^\sigma - 0.5)\Delta t$	
Density ratio	No	Yes
Viscosity ratio	No	Yes

2015; Shum et al., 2017). Thus, the SC model is adaptable to investigate the dynamic behavior of liquid water in the GDL using this assumption, which will be discussed in Chapter 3.

The EDM model also includes cohesion and adhesion forces, like the former model. Additionally, the EDM model accounts for the phase separation of non-ideal gas by applying interparticle force. As a result, the density ratio between each component can be simulated according to applied temperatures. This model is combined with the thermal LBM, described in the next part, and applied to estimate the effect of the water component on the heat transfer of the GDL using the phase separation phenomenon, which will be discussed in Chapter 4.

2.3 Thermal LBM

For the heat transfer in the GDL, the two-phase (carbon fiber and pore) conjugate heat transfer is considered because the GDL is a microscale porous fiber medium consisting of a solid fiber and a pore region. In the literature, convective and radiative heat transfers are negligible compared to the heat conduction in the GDLs microstructure for temperatures below $100\,℃$, above the PEMFC operating temperature (Ramousse et al., 2008; Ross-Jones et al., 2019; Lu et al., 2021). Therefore, only pure conductive heat transfer is considered in this study. We assume no chemical reaction and an additional heat source term, and the thermal contact resistance between adjacent fibers was also neglected (Burheim et al., 2010; Lu et al., 2021).

In this study, we use a passive-scalar method to incorporate thermal effects into the LBM. The passive-scalar method is the most popular and straightforward approach among various methods of incorporating thermal effects. (Shan, 1997; Ikeda et al., 2014). In this method, the physical temperature is passively advected by the hydrodynamics of the system. A second PDF corresponding to the temperature, $g_{i,\alpha}^{\sigma}(\boldsymbol{x}, t)$ is applied. The DDF, such as the fluid flow model in the present model, is considered for the two components (water and air). And then, the governing equation

for the pure conduction of each component is given by the formula:

$$g_{i,\alpha}^{\sigma}(\boldsymbol{x}+\boldsymbol{e}_{\alpha}\Delta t, t+\Delta t) - g_{i,\alpha}^{\sigma}(\boldsymbol{x},t) = -\frac{\Delta t}{\tau_i^{\sigma}}\left[g_{i,\alpha}^{\sigma}(\boldsymbol{x},t) - g_{i,\alpha}^{\sigma,eq}(\boldsymbol{x},t)\right] + \Delta t\omega_{\alpha}S_{\sigma} \quad (2.20)$$

where $\boldsymbol{x}$, $\Delta\boldsymbol{x}$, t, and Δt are the spatial coordinate, lattice spacing, time, and simulation time step, respectively. In thermal LBM, τ_i^{σ} is the dimensionless relaxation time related to the thermal conductivity of each component σ, and the subscript, i denoted the solid and fluid phases. $g_{i,\alpha}^{\sigma,eq}$ are the equilibrium distribution functions of fictitious energy particles of phase i of component σ. The lattice spacing ($\Delta\boldsymbol{x}$) is related to the simulation time step as $\Delta\boldsymbol{x} = \boldsymbol{e}_{\boldsymbol{\alpha}}\Delta t$, where $\boldsymbol{e}_{\boldsymbol{\alpha}}$ is the discrete velocity set of energy particles.

Additionally, S_{σ} is the phase transition term of the water component and is expressed as (Gong and Cheng, 2013; Zhang and Cheng, 2017; Zhang et al., 2020)

$$S_{\sigma} = T^{\sigma}\left[1 - \frac{1}{\rho^{\sigma}c_v^{\sigma}}\left(\frac{\partial P_{eos}^{\sigma}}{\partial T}\right)_{\rho}\right]\nabla\cdot\boldsymbol{u}^{\sigma} \quad (2.21)$$

Since liquid water is driven by capillary force (capillary number, $Ca \sim 10^{-5}$–10^{-8}) and heat convection through gas flow is negligible in the PEMFC [34, 40], it is assumed that the fluid velocity ($\boldsymbol{u}^{\sigma,eq}$ of the EDM model) inside the GDL pores is close to zero by applying a scale factor. The phase change source term, Eq. (2.21),

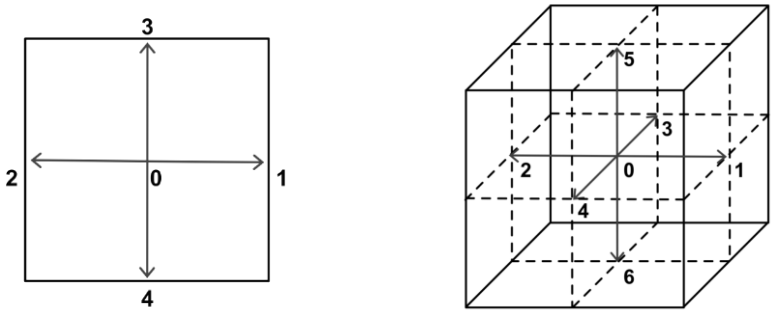

(a) D2Q5 (b) D3Q7

Fig.2.4. Schematic of representative 2D and 3D LBM schemes for thermal model

would be irrelevant, and the equilibrium distribution equations of energy particles can be simplified.

The D2Q9 and D3Q19 model are generally used in heat conduction simulation; however, it has been shown that the D2Q5 and D3Q7 models can be suitable for simulating pure thermal conduction without advection conditions (L. Li et al., 2017; Liu et al., 2020; Wang et al., 2021). For each lattice model, the equilibrium distributions are given as follows:

$$g_\alpha^{\sigma,eq} = \omega_\alpha T^\sigma \left[1 + \frac{\boldsymbol{e}_\alpha \cdot \boldsymbol{u}^\sigma}{c_s^2} + \frac{1}{2}\left(\frac{(\boldsymbol{e}_\alpha \cdot \boldsymbol{u}^\sigma)^2}{c_s^4} - \frac{\boldsymbol{u}^\sigma \cdot \boldsymbol{u}^\sigma}{c_s^2}\right)\right] = \omega_\alpha T^\sigma \tag{2.22}$$

where T^σ is the physical temperature of the σth component, c_s is the lattice sound speed, and ω is the weighting factor. The fluid velocity in Eq is ignored like in the phase change source term due to the characteristic of the pure conduction and low capillary flow regime. Thus, the equilibrium distribution equations are independent of the material phase and depend only on the lattice structure and the value of the local macroscopic temperature. The lattice sound speed is $1/\sqrt{4}$ for the D2Q5 and D3Q7 lattices. The ω weighting factors for each lattice model are:

$$\omega_\alpha = \begin{cases} 1/3, & \alpha = 0; \\ 1/6, & \alpha = 1-4; \end{cases} \tag{2.23a}$$

and

$$\omega_\alpha = \begin{cases} 1/4, & \alpha = 0; \\ 1/8, & \alpha = 1-6; \end{cases} \tag{2.23a}$$

The discrete velocity set, $\boldsymbol{e}_\alpha$, is given respectively as

$$\boldsymbol{e}_\alpha = \begin{cases} (0,\ 0), & \alpha = 0; \\ (\pm 1,\ 0),\ (0,\ \pm 1), & \alpha = 1-4; \end{cases} \tag{2.24a}$$

and

$$\boldsymbol{e}_\alpha = \begin{cases} (0,\ 0,\ 0), & \alpha = 0; \\ (\pm 1,\ 0,\ 0),\ (0,\ \pm 1,\ 0),\ (0,\ 0,\ \pm 1,), & \alpha = 1-6; \end{cases} \tag{2.24b}$$

Each phase's relaxation time depends on the macroscopic thermal conductivity of

the respective phase and the lattice parameters. According to the Chapman-Enskog Expansion, the dimensionless relaxation times are (Li et al., 2014; Wang et al., 2021)

$$\tau_i^\sigma = \left(\frac{1}{c_s^2 \Delta t} k_i^\sigma + \frac{1}{2}\right) \quad \text{with} \quad 0 < \frac{1}{\tau^\sigma} < 2 \tag{2.25}$$

The wall function in Eq. (2.13) uses individual relaxation times for the solid fibers and pores. When comparing the local and critical densities of P-R EOS, additional conductivity is adopted to account for saturated liquid water versus vapor water components.

The concept of average temperature is adopted to combine the temperature of each component, and the average temperature is applied to the P-R EOS of the EDM model. The temperature and heat flux in each lattice node are calculated from the formulas (Ikeda et al., 2014; Shen et al., 2019; Zhang et al., 2017, 2020):

$$T_{avg} = \frac{1}{\sum \rho^\sigma c_v} \sum_\sigma \rho^\sigma c_v T^\sigma \tag{2.26}$$

$$\text{with} \qquad T^\sigma = \sum_\alpha g_\alpha^\sigma \tag{2.27}$$

$$\boldsymbol{q} = \left(\sum_\alpha \boldsymbol{e}_\alpha g_\alpha^\sigma\right) \frac{\tau^\sigma - 0.5}{\tau^\sigma} \tag{2.28}$$

After the system reaches its final equilibrium state, the ETC is then calculated using the Fourier heat, Eq. (17) as follows [21–24],

$$k_{eff} = \frac{L \cdot \int \boldsymbol{q} dA}{\Delta T \cdot \int dA} \tag{2.29}$$

where $\boldsymbol{q}$ is the steady-state heat flux, ΔT is the temperature difference along the heat flux direction along with the L distance, and A is the cross-sectional area.

2.4 Boundary Conditions

Boundary conditions are important to simulate any meaningful results. In LBM, the boundary conditions are imposed with the distribution functions, f_α^σ or g_α^σ instead of the conventional velocity and pressure boundary conditions of the general commercial tools. This part introduces the bounce-back and periodic boundaries for the MCMP model and isothermal/adiabatic wall boundaries for the thermal model.

Since the particle distribution functions coming out of the wall are unknown, as described in Fig. 2.5, the bounce-back condition is implemented to deal with the wall boundary (Ladd, 1994a, 1994b; Liu and Wu, 2020). The bounce-back method means that when the fluid collides with the wall, a PDF of the same size is returned in the opposite direction of the collision. It is applied to the carbon fiber surface.

$$f_{-\alpha}(\boldsymbol{x}, t + \Delta t) = f_\alpha^+(\boldsymbol{x}, t) \tag{2.30}$$

where, $f_{-\alpha}$ and f_α^+ represent the PDFs in the opposite αth direction and after the collision, respectively. This makes the LBM easy to apply and solve problems with arbitrary shapes of complex structures.

The periodic boundary condition is the simplest, and the system becomes closed by

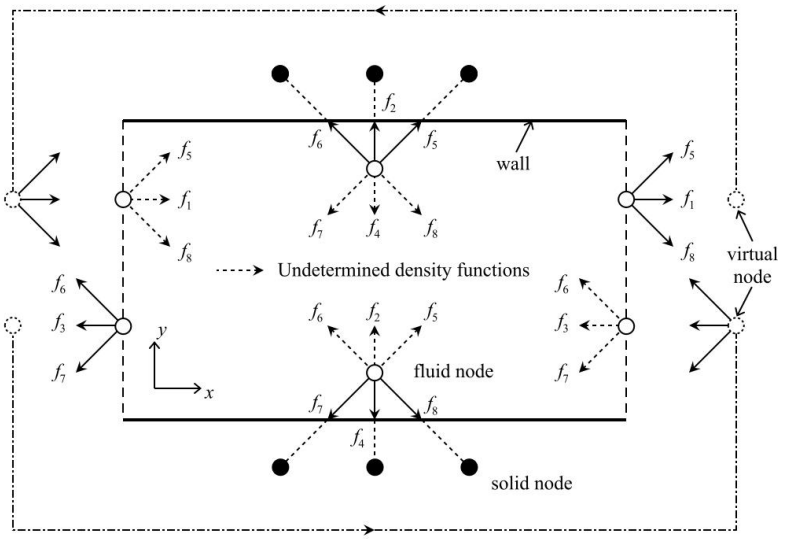

Fig.2.5. Schematic of the bounce-back rules and periodic boundary conditions for MCMP models

the boundaries being treated as if they are attached to opposite boundaries (Sukop, 2006). It is also straightforward to impose in the LBM. The PDFs are streamed with the opposite boundary in the same direction as the PDFs propagating out of the domain. This treatment method is applied to the rest of the domain boundary conditions except for the entrance/exit boundary of the multicomponent model.

In this study, the boundary condition of the thermal LBM model is set to generate a temperature gradient in one direction, as shown in Fig. 2.6, so that heat flux by the temperature gradient is generated. The end of the boundaries in the heat flux direction is fixed at high and low temperatures as isothermal boundary conditions, respectively, and the isothermal boundary condition is set as follows.

$$\sum_a g^{\sigma}_{undetermined} = T_0 - \sum_a g^{\sigma}_{determined} \tag{2.31}$$

where, T_0 indicates the initial isothermal temperature (T_{hot} or T_{cold}).

The adiabatic wall is applied to the boundary in the other direction so that only heat transfer occurs in the heat flux direction at the domain boundary, assuming that there are no additional heat sources. As shown in Fig. 2.6, when the heat flux in the x-direction occurs in the three-dimensional analysis domain, the adiabatic boundary condition is as $g^{\sigma}_{\alpha}(i,j,k) = g^{\sigma}_{\alpha}(i-1,j,k)$. The heat transfer inside the computational domain proceeds according to all lattice speed directions for each lattice model.

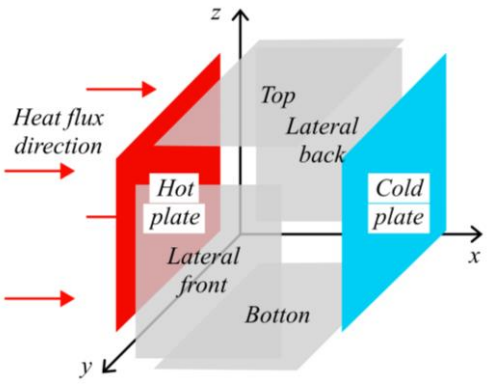

Fig.2.6. Schematic of the isothermal and adiabatic wall conditions for thermal model

2.5 Unit Conversion in LBM

The physical values are needed to be converted by using a unit conversion coefficient because they are commonly computed dimensionless in the LBM. Three fundamental units, i.e., length, time, and density, are needed to be determined priory; then, the conversion coefficients of all the others can be sequentially decided. Typically, the lattice space, time step, and fluid density are set to be 1 in the LBM computation, and it is also applied in the SC model of this study. The SC model's unit conversion is listed in Table 2.3.

Table 2.4 represents the unit conversion of the EDM and thermal model. The lattice space and time step are also set to be 1 in the EDM, but the density is set to the reduced value is equal to the physical and lattice values. The reduced value means the value divided by the critical value, i.e., $\rho_r = \rho_{\mathrm{LB}}/\rho_{\mathrm{LB},c} = \rho_{phy}/\rho_{phy,c}$. Similarly, the reduced value is applied to the temperature of the thermal model, $T_r = T_{\mathrm{LB}}/T_{\mathrm{LB},c} = T_{phy}/T_{phy,c}$ (Huang et al., 2019).

Table 2.3. Unit conversion coefficients of the SC model

Parameters	Physical value	Lattice value	Conversion coefficient in SI
Length	0.00015 [m]	150	$l_{\mathrm{LB}} = 1.0 \times 10^{-6}$ [m]
Time	2.0×10^{-7} [s]	1.0	$t_{\mathrm{LB}} = 2.0 \times 10^{-7}$ [s]
Kinetic viscosity	1.0×10^{-6} [m^2/s]	0.2	$v_{\mathrm{LB}} = 0.5 \times 10^{-5}$ [m^2/s]
Velocity	3.25×10^{-2} [m/s]	0.65×10^{-2}	$u_{\mathrm{LB}} = l_{\mathrm{LB}}/t_{\mathrm{LB}} = 5.0$ [m/s]
Density	1,000 [kg/m^3]	1.0	$\rho_{\mathrm{LB}} = 1{,}000$ [kg/m^3]
Lattice Mass			$m_{\mathrm{LB}} = \rho_{\mathrm{LB}} \cdot l_{\mathrm{LB}}^3$ $= 1.0 \times 10^{-15}$ [kg]
Pressure	250 [Pa]	0.01	$P_{\mathrm{LB}} = m_{\mathrm{LB}}/(t_{\mathrm{LB}}^2 \cdot l_{\mathrm{LB}})$ $= 25{,}000$ [Pa]

Table 2.4. Unit conversion coefficients of the EDM and thermal models

Parameters	Physical value	Lattice value	Conversion coefficient in SI
Length	0.00015 [m]	150	$l_{LB} = 1.0 \times 10^{-6}$ [m]
Time	5.0×10^{-9} [s]	1.0	$t_{LB} = 1.25 \times 10^{-8}$ [s]
Kinetic viscosity	1.482×10^{-5} [m^2/s]	0.1853	$v_{LB} = 8.0 \times 10^{-5}$ [m^2/s]
Thermal diffusivity	2.11×10^{-5} [m^2/s]	0.2638	$\alpha_{LB} = v_{LB}$
Velocity	3.0×10^{-6} [m/s]	3.75×10^{-8}	$u_{LB} = l_{LB}/t_{LB}$ = 80.0 [m/s]
Density	1.217 [kg/m^3]	1.004×10^{-2}	$\rho_{LB} = \rho_{phy} / \rho_{phy.c} \cdot \rho_{LB,c}$ = 1.0 [kg/m^3]
Lattice Mass			$m_{LB} = \rho_{LB} \cdot l_{LB}^3$ = 1.0×10^{-18} [kg]
Pressure	1,920.6 [Pa]	0.3	$P_{LB} = m_{LB}/(t_{LB}^2 \cdot l_{LB})$ = 6,402 [Pa]
Lattice Temperature	330 [K]	0.0372	$T_{LB} = T_{phy}/T_{phy,c} \cdot T_{LB,c}$ = 1.0 [K]
Specific heat, c_p	1,007 [J/kg·K]	0.1576	$c_{p,LB} = l_{LB}^2/(t_{LB}^2 \cdot T_{LB})$ = 6,400 [J/ kg·K]
Thermal conductivity	0.0253 [W/m·K]	0.0494	$k_{LB} = l_{LB} \cdot m_{LB}/(t_{LB}^3 \cdot T_{LB})$ = 0.512 [W/ m·K]

CHAPTER 3. NUMERICAL STUDY OF THE DYNAMIC BEHAVIOR OF LIQUID WATER IN THE GDL

In this chapter, the 3D microscale dynamic behavior of liquid water transport in a microstructure GDL is simulated using the MCMP SC model in the previous chapter. We use a stochastic reconstruction method to generate the 3D GDL structures and summarize the general characteristics of fiber orientation. This chapter estimates both in-plane and through-plane permeabilities and determines the effect of the fiber orientation of carbon paper on water management in the GDL. Using the simulation results, we can obtain the progression of water distribution in GDL pores and the cross-sectional average of the water saturation profiles according to the thickness of the GDL. This chapter addresses the effects of the anisotropic characteristics of the GDL on water management in PEMFC, and the GDL arrangement for better water transport is discussed in detail.

3.1 Introduction

The gas diffusion layer (GDL) is one of the critical components in PEMFC. It typically comprises highly porous materials like carbon fiber paper/cloth. It has several functional roles in the supply and distribution of gas reactants to the catalyst layer, removal of liquid water, and low-resistance conduction of electrons (Omrani and Shabani, 2017). Liquid water, generated as a byproduct during cell operation, significantly influences performance. The increasing quantity of liquid water generation results in flooding of GDL, which has a fatal impact on the performance of PEMFC. Thus, preferential water management is necessary to achieve a better arrangement of PEMFC.

Several experimental studies have been conducted to investigate the effect of the GDL structural parameters and material properties on the liquid water dynamic behavior (Lu et al., 2010; Kandlikar et al., 2011; Banerjee et al., 2016; Eller et al.,

2016; Zenyuk et al., 2016; Shum et al., 2017). Even though the empirical research considers the realistic GDL, it requires extensive financial and time costs. Thus, the lattice Boltzmann method (LBM), one of a two-phase numerical simulation, will be helpful as an alternative tool to visualize the water invasion patterns in GDL and investigate the changes due to the variation in the structural parameters.

The LBM has been effectively applied in the flow and transport processes models in microporous medium and is widely used in simulations related to PEMFC owing to its advantages (Mukherjee et al., 2009; Gao et al., 2012). As introduced previously, Chen et al. (2010, 2012a, 2012b) analyzed liquid water removal from hydrophobic GDL using a two-phase LBM model. They also applied a GC's wettability and demonstrated that less liquid water accumulates in the GDL under hydrophilic GC compared to hydrophobic GC. Moriyama and Inamuro (2011) investigated the effect of the hydrophobicity of the GDL on flooding by utilizing an arbitrarily generated porous media as the GDL for the simulation. In their results, the GDL was assumed by composed of hydrophobic carbon fibers with a hydrophilic GC. In addition, Hao and Cheng (2010) and Gao et al. (2013) addressed that an increase in the hydrophobicity of the GDL generally reduces liquid water saturation levels in the GDL. However, the previous studies were conducted as if the carbon fibers were parallel to the through-plane by compressing during the clamping process.

In this chapter, we use a carbon paper GDL with a complex porous structure obtained by a 3D structure reconstruction process instead of a homogenous GDL. 3D imaging combination and virtual stochastic generation are usually adopted to reconstruct 3D porous media. The former uses an X-ray or scanning laser microscope to scan a 3D image of a porous medium and then incorporates the 3D images to obtain the final construction. In the latter case, a porous medium microstructure is reconstructed based on the statistical information of the porous medium. This study uses the stochastic generation method because it requires lower operational costs and can implement more straightforward geometry generation than the imaging combination method (Schulz et al., 2007).

3.2 Stochastic Reconstruction Method

This part introduces the stochastic reconstruction method used to generate the carbon fiber GDL. The carbon fibers are randomly oriented and distributed in the GDL structure region. Some assumptions are employed in this method (Gao et al., 2019): (1) the carbon fibers are cylindrical with a constant radius and infinitely long with negligible curvature, and (2) the carbon fibers can overlap each other. The order of generation of the gas diffusion layer using the stochastic model is as follows:

1) Define the number of fibers, layer thickness, and fiber diameter
2) Set azimuthal angle, θ [$-\pi/2$, $\pi/2$] and polar angle, φ [0, π]
3) Then, the orientation vector, $\vec{u}$ is defined as below:

$$\vec{u}(u_1, u_1, u_1) = [sin\,\varphi\, cos\,\theta\,, sin\,\varphi\, sin\,\theta\,, cos\,\varphi] \tag{3.1}$$

4) Calculate the distance, l, between the central point and arbitrary point by the modulus of the cross product of the orientation vector and position vector, $\vec{p}$

$$l = \sqrt{\begin{array}{c}[u_2(z-z_0)-u_3(y-y_0)]^2 \\ +[u_3(x-x_0)-u_1(z-z_0)]^2 \\ +[u_1(y-y_0)-u_2(x-x_0)]^2\end{array}} \tag{3.2}$$

The position vector, $\vec{p}$ is defined by an arbitrary point (x, y, z) and a center point of fibers (x_0, y_0, z_0) that passes through the axis. Then, the skeleton of the entire 3D structure of GDL is generated, and when the distance from the axis to an arbitrary point is less than the fiber radius, the point is contained as carbon fiber.

As mentioned, most previous studies on the influence of the characteristics of GDLs

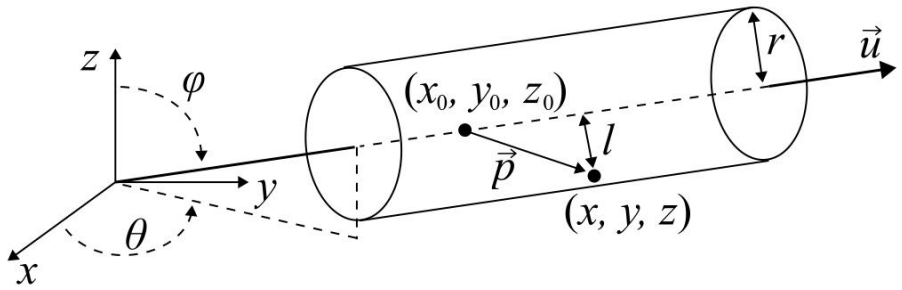

Fig.3.1. Three-dimensional cylindrical model for the skeleton of carbon fibers

in PEMFCs assume that all carbon fibers exist in horizontal parallel layers (i.e., φ = $\pi/2$ is constant) (Thiedmann et al., 2008; Yablecki et al., 2012a, 2012b; Froning et al., 2013; Zenyuk et al., 2016). In those studies, the carbon fibers' diameter is given, and carbon fibers are randomly assigned until a defined porosity is satisfied layer by layer. It is assumed that fibers are infinite cylinders without any curvature capable of intersecting with each other. It contrasts with the actual characteristic of GDLs because real carbon paper GDLs consist of carbon fibers randomly oriented in a plane, leading to different in-plane and through-plane properties (Hao and Cheng, 2009).

Although some assumptions similar to previous works are used in this dissertation, we even consider an interruption of the carbon fibers in the through-plane by adjusting the directional distribution to demonstrate the effects of in-plane and through-plane permeability (Schladitz et al., 2006). It should be noted that total layers and fibers determine the porosity of the reconstructed GDL. Therefore, the final porosity of the reconstructed GDL does not precisely match the specified value but is an acceptable approximation.

The regenerated GDLs are represented in Fig. 3.2. Generally, the GDL is coated by resin and Polytetrafluoroethylene (PTFE). Still, in this study, it is considered only the influence of the GDL morphological conditions according to the change of the orientation of the carbon fibers. As shown in Fig. 3.2, the center point and azimuthal angle of fibers are identical, but only the polar angle is changed according to applied ranges. We adopt three different fiber polar angle ranges ($\varphi = \pi/2 \pm 5°$, $\pm 15°, \text{and } \pm 25°$) based on the 3D GDL with no fibers intervening in the through-plane direction ($\varphi = \pi/2$).

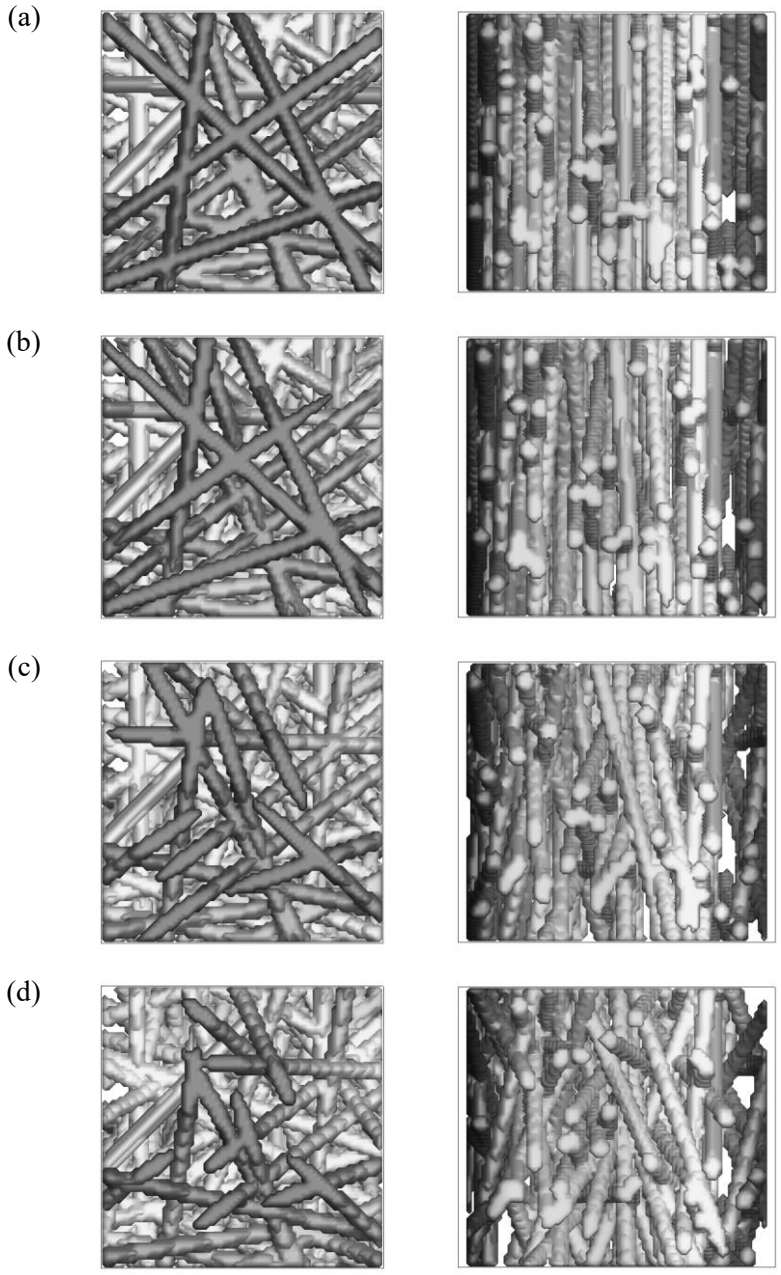

Fig.3.2. Regenerated GDL with various polar angles, (a) $\varphi = \pi/2$, (b) $\varphi = \pi/2 \pm 5°$, (c) $\varphi = \pi/2 \pm 15°$, (d) $\varphi = \pi/2 \pm 25°$ (left: top view, right: side view)

3.3 Model Description

In this chapter, the effect of the fiber orientation on the liquid water transport in the GDL is simulated using the SC model in Chapter 2. The 3D GDL is used to simulate liquid water transport through the GDL. We generate a 3D GDL reconstructed with a fiber diameter of 8 μm with an average porosity of 0.753. The number of layers is 20; hence, the thickness of the GDL is 160 μm. The size of the calculation domain is $270 \times 150 \times 150$ lattice units, where the lattice unit length, lu, is set to be 1 μm. The time step (ts) for simulation is set to 2×10^{-7} s. The wettability of GDL is assumed to be uniform to consider only the effect of fiber orientation on water transport. It is set to 140° as if the PTFE is coated uniformly. As mentioned, this study does not consider other parameters affecting the GDL structural condition (e.g., microporous layer, compression ratio, rib structure).

Referencing the dimensionless number that characterizes liquid water transport in PEMFC decides the simulation conditions. In PEMFC, liquid water transport is relatively slow, so capillary and viscous forces are the dominant flow, as described in Fig. 3.3 (Lenormand, 1990). The capillary number, *Ca*, represents the ratio of viscous to capillary force and is around the order of $10^{-5} - 10^{-8}$ under typical fuel cell

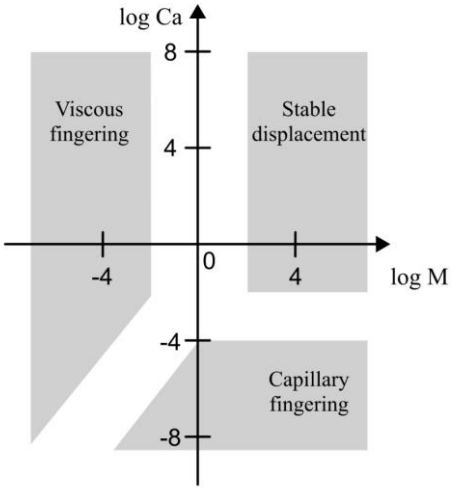

Fig.3.3. Immiscible two-phase flow pattern phase diagram: stable displacement, viscous fingering, and capillary fingering

operating conditions. Therefore, the ratios of water and gas densities and viscosities do not include because the effect of other forces, except capillary pressure, is not significant in slow two-phase flow in a porous medium like GDL (Kim et al., 2015; Shum et al., 2017). In the simulation, liquid water is injected at constant pressure through a reservoir region initially filled with liquid water.

A schematic representation of the simulation setup consisted of three regions: a water reservoir, the GDL, and empty space (Fig. 3.4). The water reservoir is set at ten lu between the first layer of the GDL and the inlet. Two immiscible components are assumed as 1: water and 2: air. Thus, the water reservoir area is filled with component 1 by setting $\rho_1 = 1$ and $\rho_2 = 10^{-5}$. For the rest area, air and water densities are set to $\rho_2 = 1$ and $\rho_1 = 10^{-5}$, it indicates no fluid in the rest of the area.

At the inlet boundary, liquid water fills the water reservoir region with a given velocity of $u_{\text{in}} = 6.5 \times 10^{-3} \text{lu ts}^{-1}$ ($u_{\text{phy}} = u_{\text{in}} \times l_{LB}/t_{LB} = 3.25 \times 10^{-2}$ m/s). A Dirichlet momentum boundary condition is adopted to achieve the given velocity. It acts as an external force on each lattice node as a form of the equilibrium velocity, $\boldsymbol{u}^{\sigma,eq}$. We apply an open boundary condition at the outlet boundary, which is also applied by the Dirichlet boundary condition to achieve the outlet pressure. A periodic boundary condition at the remaining four boundaries around the domain and parallel to the flow direction (*x*-direction). The bounce-back boundary condition is considered on all solid surfaces.

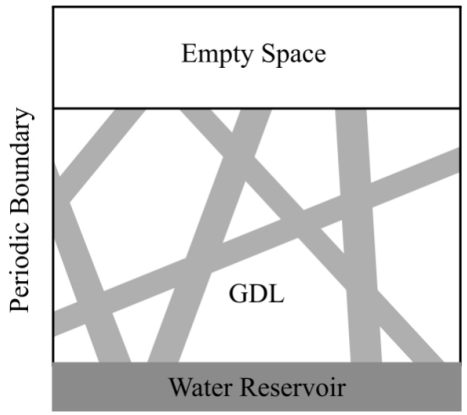

Fig.3.4. Schematic of the simulation domain and boundary conditions

3.4 Model Validation

This part presents the validity of forcing terms involved in the SC model and the reliability of the reconstructed GDL structure by evaluating the permeability of the porous media and comparing the permeability to that obtained using the Kozeny–Carman (KC) equation. Furthermore, the primary physical parameters for the multicomponent, such as the fluid/fluid and fluid/solid interaction parameters, require a priori evaluation through model calibration using numerical experiments. Fluid/fluid interaction causes surface tension force and fluid/solid interaction results in wall adhesion force. We conduct two numerical experiments to evaluate these physical parameters for each model: (1) The fluid/fluid interaction parameter is evaluated through a droplet test in the absence of a solid phase, and (2) the fluid/solid interaction parameter is evaluated via a static droplet test in the presence of a solid wall.

3.4.1 Single phase permeability in In- and Through-plane directions

The permeability of a medium, κ, is an important physical property that affects mass transportation performance in heterogeneous porous media. At a low Reynolds number, the permeability of a porous medium is defined by Darcy's law (Neale and Nader, 1973) as

$$\bar{u} = -\frac{\kappa}{\mu}\nabla P \tag{3.3}$$

where $\bar{u}$ is the volume-averaged velocity throughout the porous medium, μ is fluid flow viscosity, and ∇P represents the pressure gradient vector. The pressure gradient refers to the pressure difference between the inlet and outlet of porous media, and has an inverse relationship with permeability.

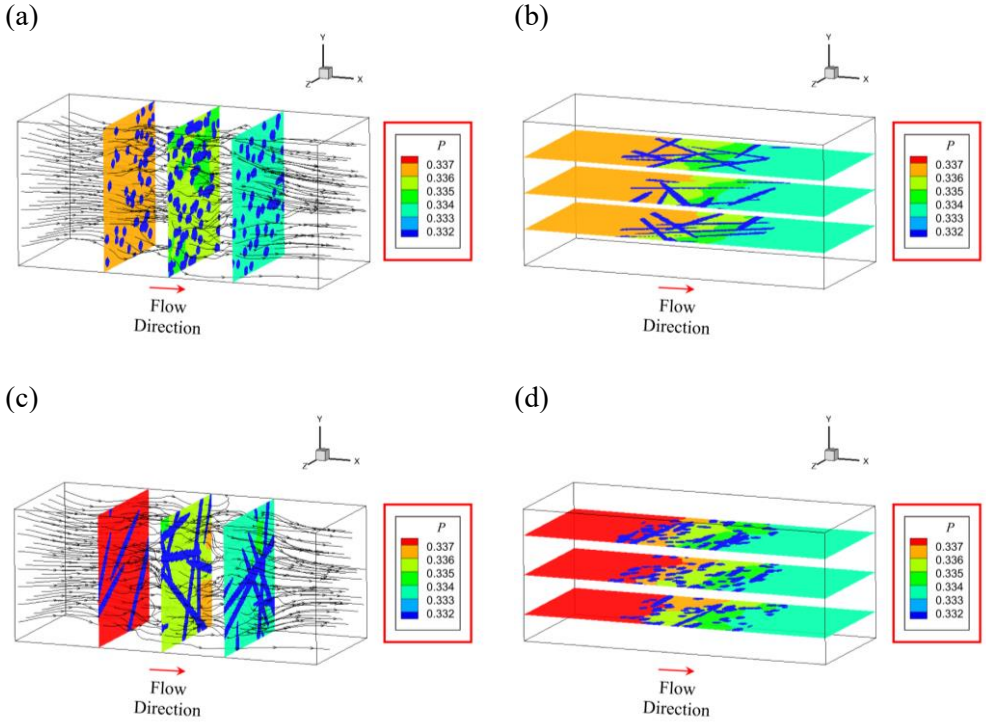

Fig.3.5. LB simulation results for single-phase permeability through 3D carbon paper GDL: (a) Velocity streamline for in-plane flow; (b) Pressure contours for in-plane flow; (c) Velocity streamline for through-plane flow; (d) Pressure contours for through-plane flow

In porous media, permeability is generally described by the porosity of porous media. The KC equation has been extensively applied in previous studies to estimate the flow permeability of randomly distributed particulate porous media. In the KC equation, the flow permeability κ of porous media with porosity ε and mean particle diameter d is estimated below (Kaviany, 2012)

$$\kappa = \frac{d^2}{16C_{kc}} \frac{\varepsilon^3}{(1-\varepsilon)^2} \tag{3.4}$$

where C_{kc} is the KC constant, which is used as a fitting parameter, and its value depends on the media type. In literature, the value of the KC constant for GDL materials varies considerably, ranging from 1.45 to 26.50. However, the value ranges

between 4.06 and 4.54 for typical commercial materials based on carbon fibers (Gostick et al., 2006; Ostadi et al., 2010). In the present study, the through-plane and in-plane KC constants are set as 4.07 and 2.7, respectively, to match the simulation results and KC equation.

We calculate single-phase permeability using a cubic domain with dimensions of $361 \times 151 \times 151$ lu^3. The empty space, 100 lu, is set both in front of and behind the GDL to make the velocity profile fully developed. The size and thickness of the GDL used in this part are the same as that implemented in other parts. It is assumed that a constant velocity corresponding to $Re = 0.5$ enters the area through the bottom plane. The top plane of the domain is assumed to be a constant pressure, and the rest of the side planes are treated as walls with Bounce-back conditions applied.

The LB simulations for single-phase permeability through a 3D carbon paper GDL show a pressure gradient and streamlines in through-plane and in-plane flow (Figs. 3.5(a) and (c)). The pressure drop in the through-plane direction is more significant than that in the in-plane direction (Figs. 3.5(b) and (d)). The streamlines are the most disrupted in the middle of both flow directions. This implies that liquid water will detour toward the in-plane direction and the side of the GDL structure because of considerable flow resistance. The flow permeability values obtained from the LB simulations agree with the KC equation (Tables 3.1 and 3.2). Permeability in the in-

Table 3.1. Comparison of the GDL permeability of the through-plane direction of LB simulation results with the KC equation

Case	Flow permeability, κ in the GDL (d = 8 μm)			
	Porosity ε	KC [10^{-12} m^2]	LBM [10^{-12} m^2]	Error (%)
$\varphi = \pi/2 \pm 0°$	0.7477	6.454	7.5215	16.54
$\varphi = \pi/2 \pm 5°$	0.7516	6.763	7.6316	12.85
$\varphi = \pi/2 \pm 15°$	0.759	7.399	7.8787	6.49
$\varphi = \pi/2 \pm 25°$	0.7618	7.658	8.2344	7.53

Table 3.2. Comparison of the GDL permeability of the in-plane direction of LB simulation results with the KC equation

Case	Flow permeability, κ in the GDL (d = 8 μm)			
	Porosity ε	KC [10^{-12} m^2]	LBM [10^{-12} m^2]	Error (%)
$\varphi = \pi/2 \pm 0°$	0.7471	9.659	8.5334	11.65
$\varphi = \pi/2 \pm 5°$	0.7496	9.952	9.325	6.3
$\varphi = \pi/2 \pm 15°$	0.7571	10.897	10.65	2.27
$\varphi = \pi/2 \pm 25°$	0.76	11.291	10.6636	5.55

plane direction is higher than that in the through-plane direction. This is due to the fiber orientation and anisotropy of the material. The LB results show that the obtained permeability ratio ranges between $1.135 - 1.352$. This is consistent with trends reported in other numerical results (Schulz et al., 2007; Mukherjee et al., 2009; Gao et al., 2012). Thus, our LBM model can be trusted to evaluate the permeability of porous media and simulate the dynamic fluid flow inside the GDLs.

3.4.2 Static droplet test

For the validity of the cohesion force contribution, we conduct a two-component (water and air) droplet test using the SC model described in the previous part and validate the shape of the spherical droplet utilizing the well-known Laplace law (Fig. 3.6). According to the Laplace law, the pressure difference, ΔP, between the interior and exterior of a 3D spherical droplet (Fig. 3.6(a)) is linearly proportional to liquid surface tension, γ, and inversely proportional to droplet radius, R. For a 3D droplet, this equation is expressed as

$$\Delta P = P_{in} - P_{out} = \frac{2\gamma}{R} \tag{3.5}$$

A droplet with different initial sizes is placed in the center of a cubic lattice with $101 \times 101 \times 101$ nodes, and the periodic boundary condition is set on all of its

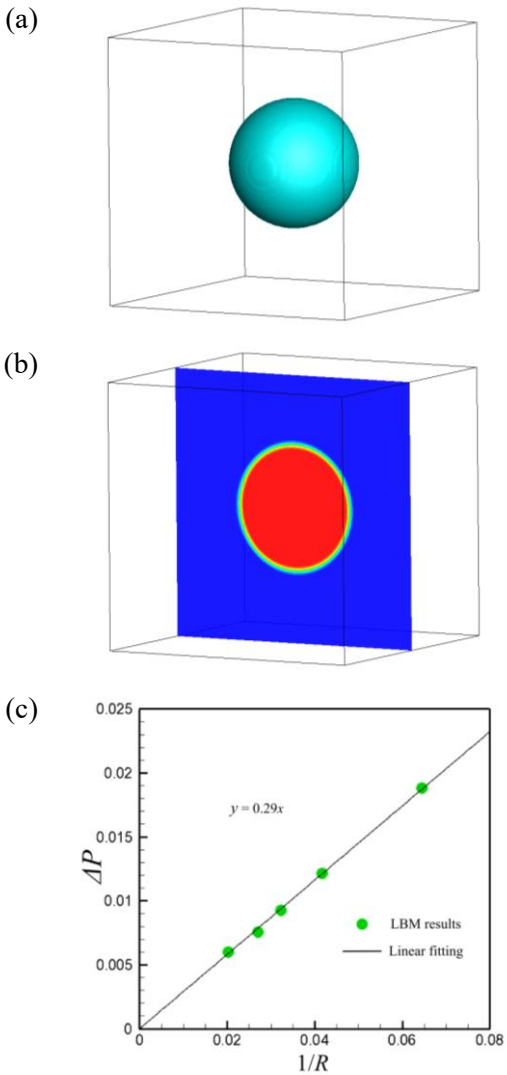

Fig.3.6. LB simulation results for the static droplet test: (a) 3D schematic of an ideal droplet; (b) density contours of liquid water; (c) pressure difference *vs*. 1/*R* for a range of droplet radii

lateral faces (Fig. 3.6(b)). We record droplet radii and the pressure differences (in the lattice unit) between the interior and exterior of the droplets when a steady state is achieved (Fig. 3.6(c)). The results demonstrate that the SC model follows the Laplace law with excellent accuracy, with a surface tension of 0.145 lattice units (Fig. 3.6(c)).

3.4.3 Static contact angle test

The interfacial tension at liquid/solid and gas/solid interfaces determines the contact angle. This measurement indicates the balance of interfacial forces on liquid/gas, liquid/solid, and gas/solid interfaces. A small volume of liquid on a solid surface tends to spread as a film on hydrophilic surfaces and forms a droplet on hydrophobic surfaces.

In the adhesive interaction model, the adhesion coefficient, G_{adh}^{σ}, represents the wettability of component σ on a solid surface as below:

$$\cos\theta_c = \frac{(\gamma_{LS}-\gamma_{GS})}{\gamma_{LG}} = G_{adh}^{\sigma} - G_{adh}^{\bar{\sigma}} = \Delta G_{adh} \tag{3.6}$$

The adhesion coefficients of σ and $\bar{\sigma}$ can control the contact angle by changing their difference $(\Delta G_{adh} = G_{adh}^{\sigma} - G_{adh}^{\bar{\sigma}})$. In this calculation, σ and $\bar{\sigma}$ are set as liquid and gas, respectively. It is assumed that G_{adh}^{σ} equals $-G_{adh}^{\bar{\sigma}}$ to perform straightforward calibration in adjusting force term; however, G_{adh}^{σ} and $G_{adh}^{\bar{\sigma}}$ are intrinsically independent parameters. Using this concept, numerous LB simulations with various values of G_{adh}^{σ} are implemented, and the resulting values of ΔG_{adh} are compared with the observed contact angles (Fig. 3.7). A semispherical droplet is placed initially on the flat bottom wall of a cubic lattice with $101 \times 101 \times 51$ nodes. The lateral interfaces of the computational domain are set periodic boundary

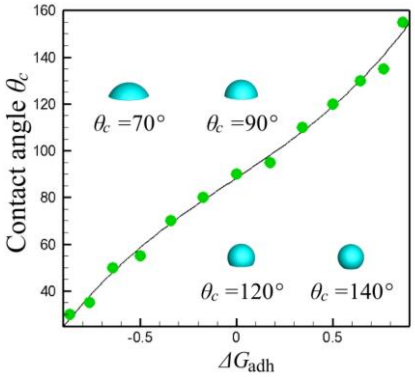

Fig.3.7. LB simulation results of contact angle of liquid droplets formed with different adhesion coefficients, ΔG_{adh}

conditions. We observe that positive ΔG_{adh} represents a hydrophobic solid surface, whereas negative ΔG_{adh} represents a hydrophilic solid surface. These results demonstrate that the SC model, including the cohesion and adhesion forcing terms, can adequately simulate liquid water transport inside GDL with varying wettability.

3.5 Result and Discussion

As mentioned previously, under typical operating conditions for PEMFCs, $Ca = u\mu_l/\gamma$ is of the order of $10^{-5} - 10^{-8}$, and two-phase flow in a GDL belongs to the regime of capillary fingering, as shown in Fig. 3.3 (Sinha and Wang, 2007; Tabe et al., 2009). A uniform velocity of 6.5×10^{-3} lu ts^{-1} is applied at the inlet boundary in this study. This velocity value corresponds to a capillary number of $Ca \approx 10^{-4}$, which is higher than the capillary number for average water production rates in operated PEMFCs. However, this value is still belong to the capillary fingering regime and ensures capillary-dominant liquid water transport (Sukop, 2006; Sakaida et al., 2017). Therefore, the ratios of the densities and viscosities of water and gas can be neglected because the effects of gravitational, inertial, and viscosity forces are insignificant compared to capillary forces. For this reason, the densities of water and gas are arbitrarily equal, and the ratio of viscosities of water and gas is set to be 1.0 for numerical stability in the SC model.

3.5.1 Effect of fiber orientation in the In-plane of the GDL

Liquid water in the GDL possibly exists as a continuous complex liquid with a surface modified to fit the generated pore structure and not as a discrete droplet (Nam et al., 2009). The liquid pressure gradient in the adjacent pores drives the liquid water in the GDL. In steady-state cell operation, the gas pressure of the GDL is almost constant. Therefore, only the capillary pressure gradient due to localized water condensation in the GDL acts as the driving force for liquid water transport. According to the Young–Laplace equation, capillary pressure P_c can be expressed

as

$$P_c = P_{air} - P_{water} = -c\frac{\gamma cos\theta_c}{R} \tag{3.7}$$

with c = 1 for 2D, and c = 2 for 3D

where γ and θ_c are the surface tension and contact angle of liquid water, respectively, and R is the largest pore radius. According to Eq. (3.7), the capillary pressure depends on the pore size at a constant contact angle. In this study, the GDL is assumed to have uniform wettability, which is set as 140° representing the GDL coated by hydrophobic materials. Thus, permeability is a key structural characteristic for determining mass transport in the GDL (Moriyama and Inamuro, 2011; Gao et al., 2012).

To investigate the influence of fiber orientation on liquid water distribution in the GDL, we compared the cases of GDLs with polar angle ranges $\varphi = \pi/2 \pm 0°$, ±5°, ±15°, and ±25° in the in-plane direction (Didari et al., 2012; Mortazavi and Tajiri, 2014). As described above, the GDL is an anisotropic material; thus, its permeability differs between the in-plane and through-plane directions. The permeability in both directions gradually increased with the range of fiber orientation (Fig. 3.8(a)). Within the range applied in this study, the permeability in the through-plane direction tended

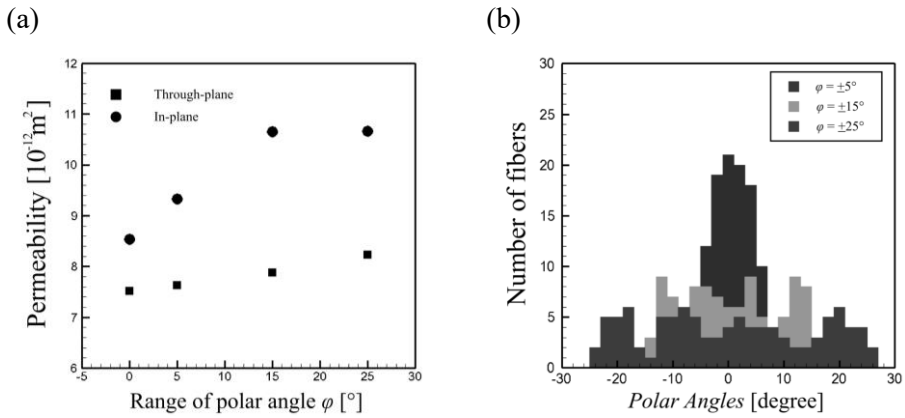

Fig.3.8. (a) Permeability trend chart of the GDL with different polar angle ranges, (b) fiber polar angle range distribution of the reconstructed GDL

to increase gradually. In contrast, the permeability in the in-plane direction increased rapidly at first and then gradually (Fig. 3.8(a)) (Yiotis et al., 2016). The ratio of in-plane permeability to through-plane permeability employed in this study ranged from 1.135 to 1.352 (Schulz et al., 2007). Fig. 3.8(b) shows the fiber polar angle range distribution of the reconstructed GDLs using a stochastic method. When it follows the narrow distribution in the in-plane with a zero value, the fiber's direction becomes more parallel to the through-plane of the GDL surface. All samples represent the valid anisotropy in the in-plane directions of the GDL, and they quite satisfactorily describe the intrinsic feature of commercial GDLs (Gostick et al., 2006; Tahir and Vahedi Tafreshi, 2009). The sample used in this study shows an even distribution at all applied polar ranges.

The observed water invasion pattern along the GDL is shown in Figs. 3.9 – 3.12. As a strong hydrophobic contact angle of 140° is applied, the "capillary fingering" phenomenon is well represented in all cases. The waterfront forms a convex shape owing to the hydrophobicity of the fibers, and water transfers through a passage in which small local capillary resistance acts in the through-plane and in-plane directions. Consequently, water breakthrough occurs at the end of a preferential path on the GDL surface, and a liquid droplet is formed and grows.

The polar angle range does not significantly influence the character of the water transport in the GDL. The preferential path and breakthrough point are almost the same because all cases have the same center point and azimuthal angle of the fibers. However, as the fiber orientation is applied in the in-plane direction, the tendency of water to detour through the in-plane direction is reduced, and water flows more readily in the through-plane direction compared to the Ref. Chen et al. (2010) and Eller et al. (2016). The fiber orientation in the in-plane direction creates a passage through which liquid water moves more efficiently in the through-plane direction of the GDL.

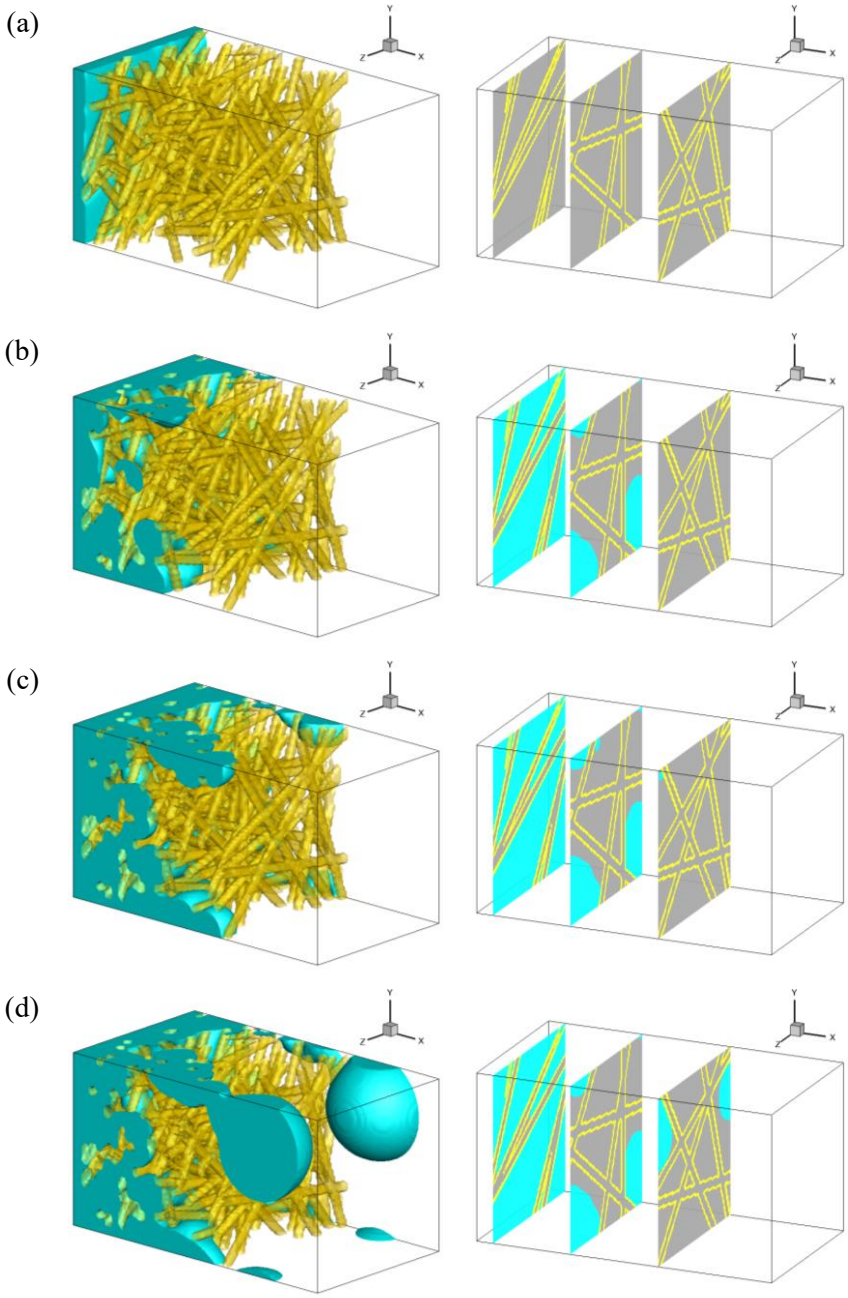

Fig.3.9. Temporal water behavior and distribution in the reconstructed GDL microstructure with a polar angle range of π/2 ±0°, (a) 0.2 ms, (b) 11.8 ms, (c) 21.8ms, (d) 31.8 ms

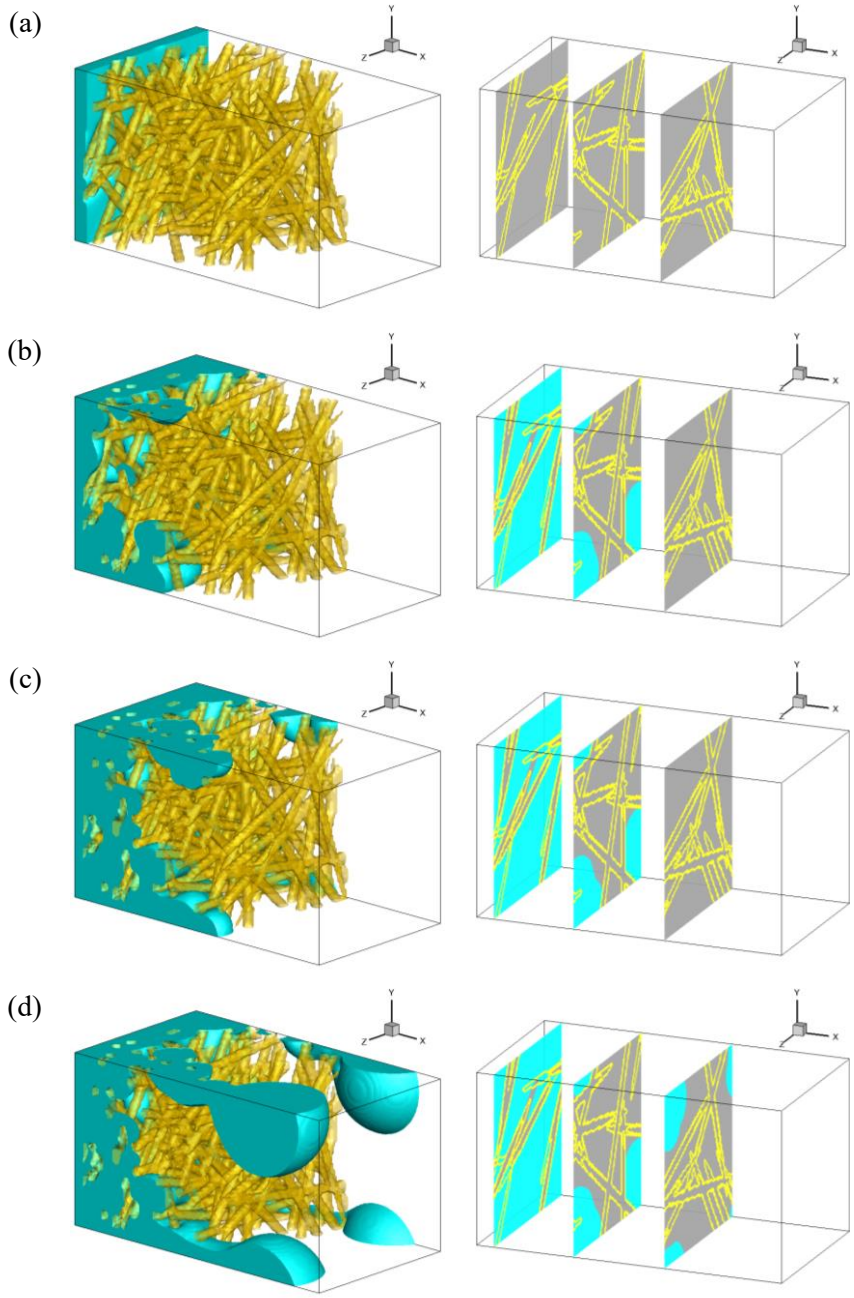

Fig.3.10. Temporal water behavior and distribution in the reconstructed GDL microstructure with a polar angle range of $\pi/2 \pm 5°$, (a) 0.2 ms, (b) 10.2 ms, (c) 20.2ms, (d) 30.2 ms

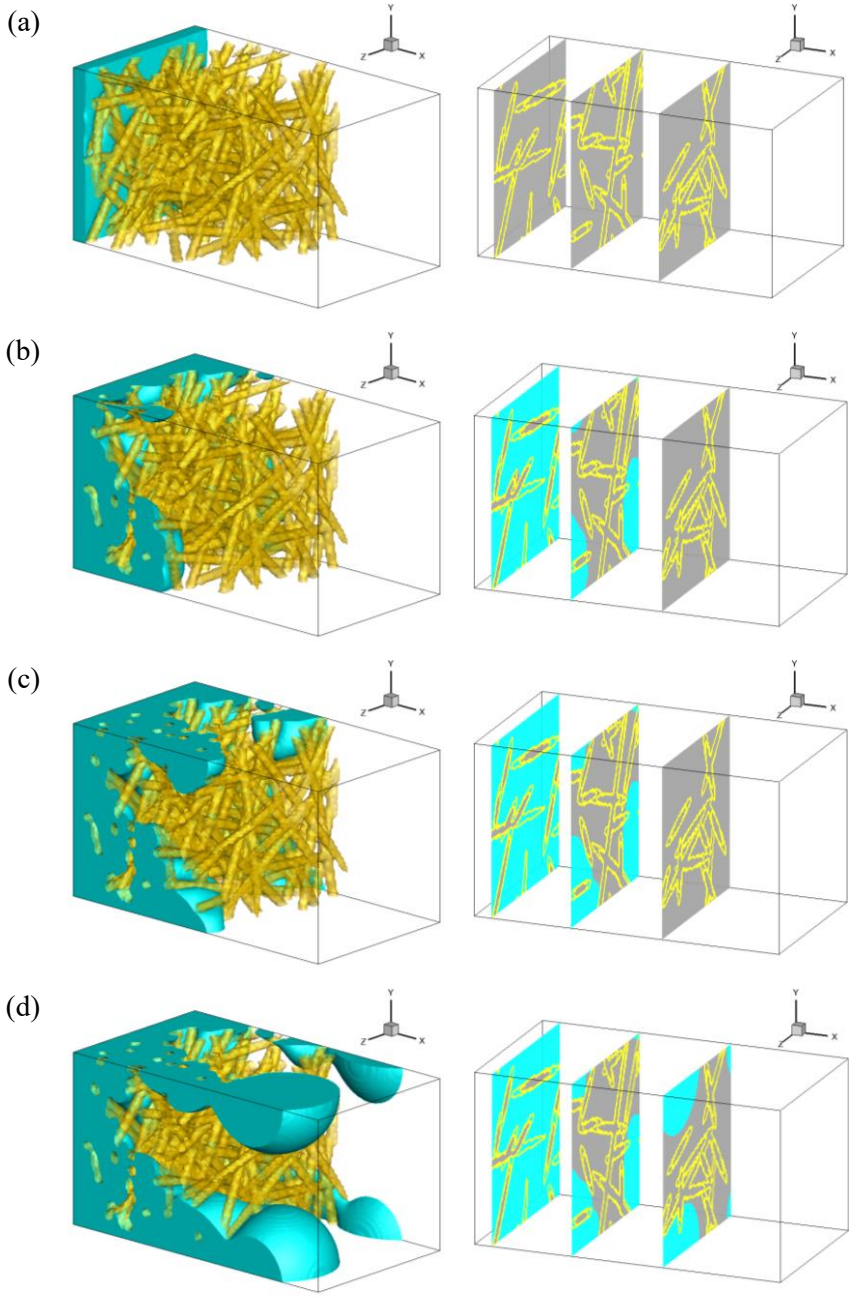

Fig.3.11. Temporal water behavior and distribution in the reconstructed GDL microstructure with a polar angle range of $\pi/2 \pm 15°$, (a) 0.2 ms, (b) 10 ms, (c) 19.8 ms, (d) 29.6 ms

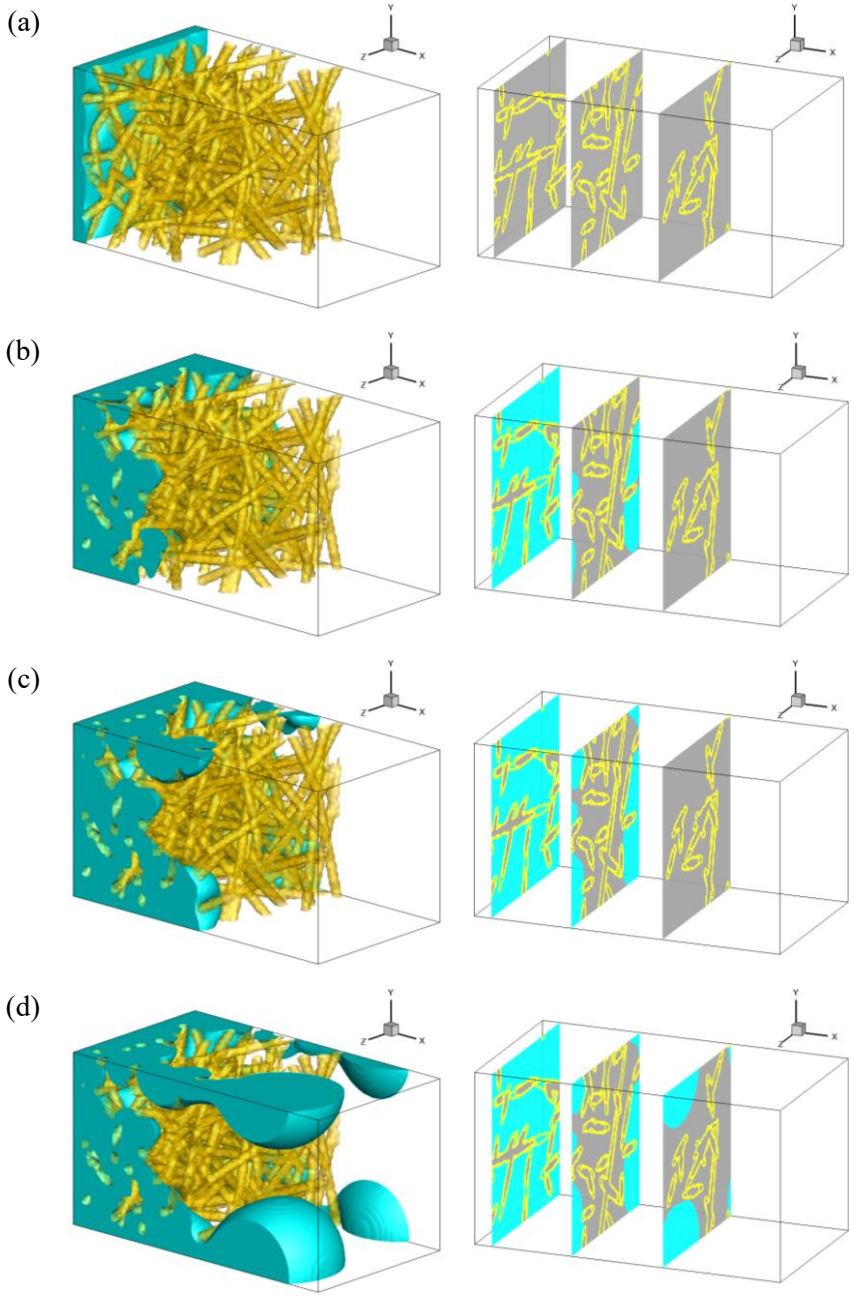

Fig.3.12. Temporal water behavior and distribution in the reconstructed GDL microstructure with a polar angle range of $\pi/2 \pm 15°$, (a) 0.2 ms, (b) 9.2 ms, (c) 18.2 ms, (d) 27.2 ms

The cross-sectional average water saturation along the through-plane direction of the GDL decreases for all polar angle ranges until it reaches the interface between the GC and GDL surface (Fig. 3.13). Here, the average cross-sectional saturation is defined as the ratio of the area occupied by water to the total pore area in the cross-section. The concavity of the water saturation profile increases with the polar angle range applied to the carbon fibers of the GDL. A concave type profile implies that liquid water escapes only through the pathway preferentially formed toward the GC without filling the GDL as governed by the polar angle range applied in the in-plane direction.

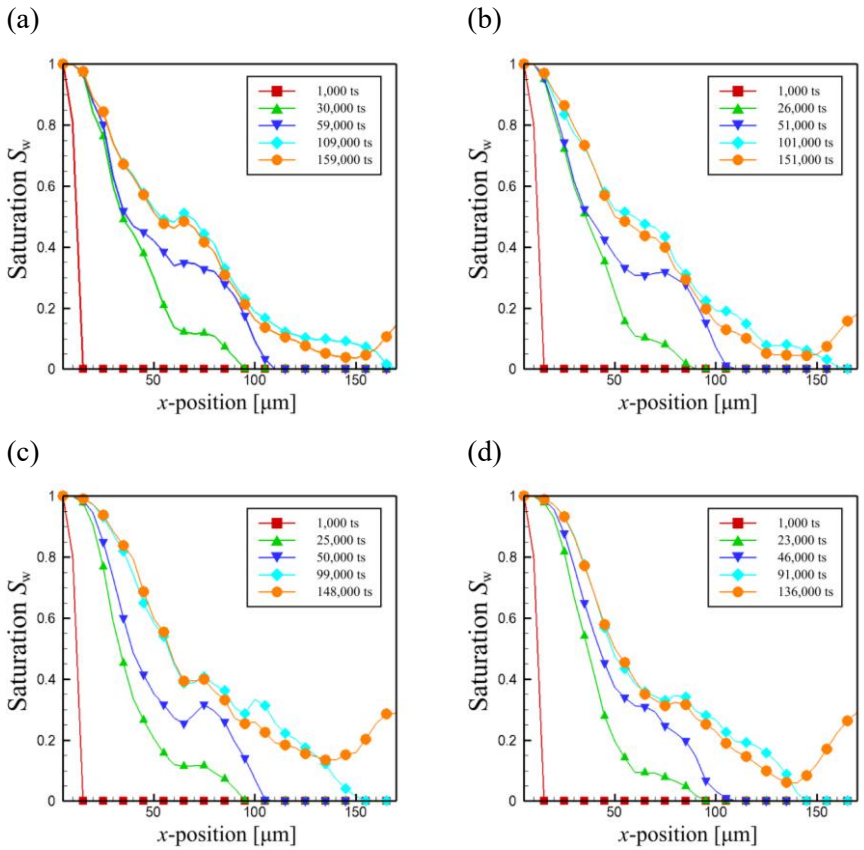

Fig.3.13. Liquid water saturation profiles along the through-plane direction of the GDLs: (a) $\varphi = \pm 0°$, (b) $\varphi = \pm 5°$, (c) $\varphi = \pm 15°$, and (d) $\varphi = \pm 25°$

In addition, it is indicated that the applied polar range changes the pore shape. An oblate shape in through-direction becomes transient to spherical and elliptical shapes according to the polar range, respectively. As shown in Fig. 3.14(a), the average water saturation slightly increases in the applied $\pm 15°$ range case, and the others maintain similar saturation levels with a standard deviation of less than 1.6%. Fig. 3.14(b) represents the time evolution of normalized total saturation in the GDL. Water saturation and time are normalized by the steady-state saturation and time, respectively, of the case where the polar range is not applied. The variation of water saturation indicates the amount of water during the simulation iteration, and it is

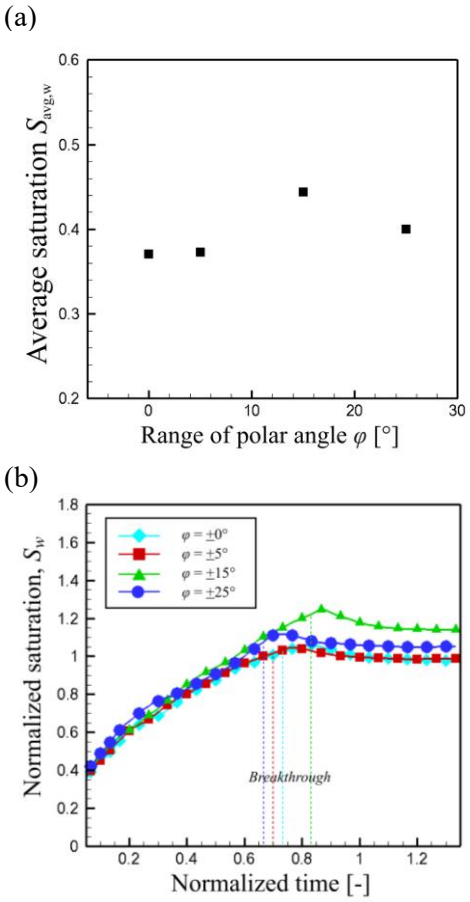

Fig.3.14. (a) Average liquid water saturation level of the GDL at various polar angle ranges, (b) dynamic saturation curves of the applied polar ranges

converted to the molar rate of water generation using the below equation (Pournemat et al., 2019).

$$\varepsilon V_{GDL} \Delta S_{avg,w} = \frac{\dot{n}_{H_2O} M_{H_2O}}{V_{node} \rho_{H_2O}} \Delta t_{step} \tag{3.8}$$

where, ε is the porosity of the GDL and V_{GDL} is the total lattice nodes of the GDL. M_{H_2O} is the molar mass of water $[\mathrm{g/mol}]$, V_{node} is the volume of each lattice node $[\mathrm{cm}^3]$, ρ_{H_2O} is the density of water $[\mathrm{g/cm}^3]$, and Δt_{step} is the time step calculated for each simulation iteration [s].

Eq. (3.8) means the equivalent number of lattice nodes per simulation iteration, and the corresponding current density, *j*, for this study can be calculated as follow :

$$\dot{n}_{H_2O}[\mathrm{mol/s}] = \frac{jA}{2F} \tag{3.9}$$

where, *j* is the current density $[\mathrm{A/cm}^2]$, *A* is the surface area of the assumed catalyst layer $[\mathrm{cm}^2]$, and *F* is the Faraday constant. In Eq. (3.9), "two" is the electron stoichiometry in the water production reaction to produce one molecule of water. In this study, the corresponding current density is approximately $167\ \mathrm{mA/cm}^2$ belongs to a very low current density ($< 250\ \mathrm{mA/cm}^2$) (White et al., 2019). The current density is due to the small domain size selected in this study, but the domain size is enough to represent the characteristic of the general GDL structure (Liu et al., 2019).

In Fig. 3.14(b), the saturation level increases slightly after the breakthrough of liquid water in all cases. It is due to a temporary inflow through preferential routes. After that, it decreases due to suction and droplet growth in the in-plane direction. Compared to the case applied fibers parallel to the through-plane, other cases reach the GC interface faster than the parallel case except for the $\pm 15°$ range case.

As defined in Eq. (3.7), capillary pressure is related to the pore size of the GDL at the identical wettability condition. Thus, as pore size decreases, the capillary pressure increases, and a more significant force is required for liquid water to pass through the GDL. The relative pressure distributions of the air component in GDL at the first

breakthrough are similar in each case for all directions (Fig. 3.15). As shown in Fig. 3.16, the pressure drops in the through-plane direction show a more considerable difference than in the in-plane direction as the polar angle range is applied. The fiber orientation in the in-plane makes the mean pore radius in the through-plane larger, in contrast to that in the in-plane smaller. In this study, even considering that periodic conditions are applied to the lateral side of the domain, an additional path is not created in the in-plane direction. This implies that liquid water is still more affected by the pressure drop in the through-plane direction compared with the other in-plane direction, even though more carbon fibers are straightforward to the through-plane

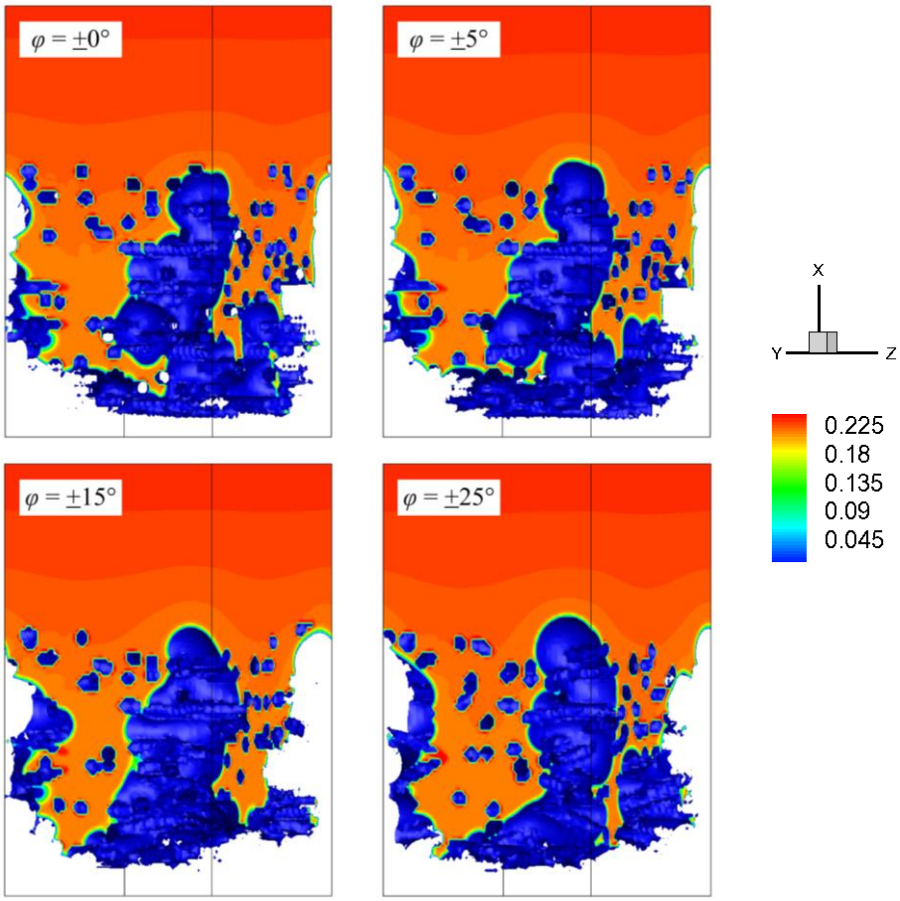

Fig.3.15. Relative gas pressure in the GDL with different polar angle ranges at the first breakthrough

direction by adjusting the polar angle range.

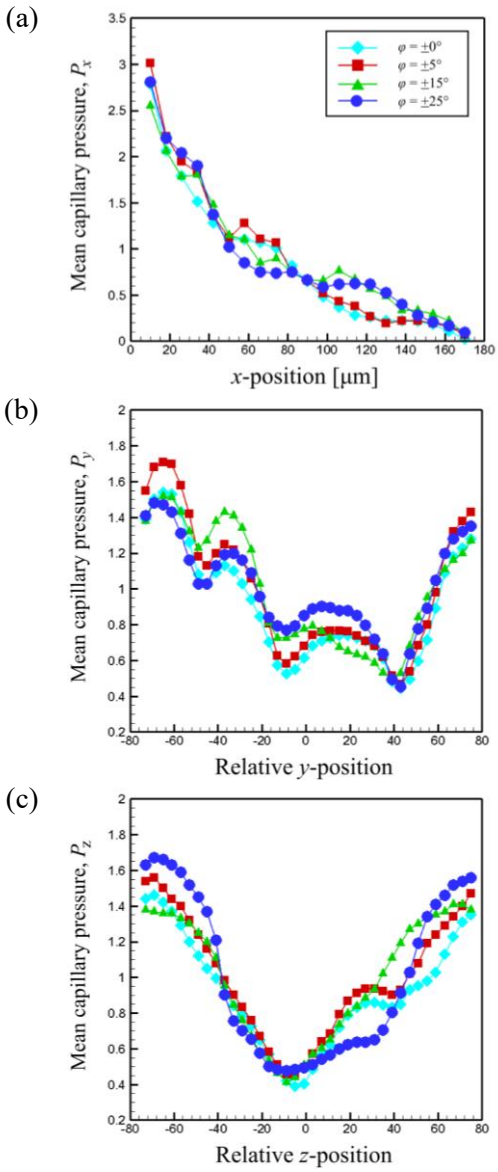

Fig.3.16. Normalized mean capillary pressure in each plane direction at the first breakthrough, (a) through-plane direction, (b) *zx*-plane direction, and (c) *xy*-plane direction

A single droplet is formed through the pores of the through-plane, where a relatively low capillary resistance is applied. The liquid water throat, representing the interface between the GC and GDL, becomes thicker as the polar angle range expands. Furthermore, the carbon fiber's orientation also influences an apparent angle representing the contact angle after the breakthrough. Figs 3.17(a) and (b) represent

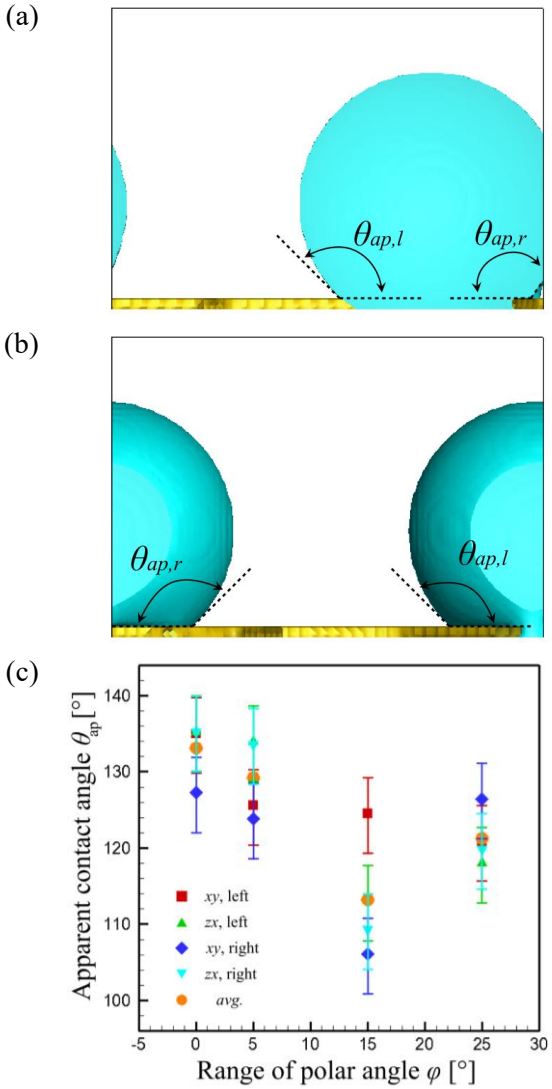

Fig.3.17. The apparent contact angle of the liquid droplet (a) *xy*-plane, (b) *zx*-plane, and (c) apparent contact angles in various polar angle ranges

the apparent angle of the case without an applied polar angle. The right and left sides of the contact angle are defined based on the center of the droplet, and the selected droplet represents the steady-state condition (Yu et al., 2018). Apparent angles are measured using the "ImageJ" program, and the measured angles are displayed with an error of ±5°.

As shown in Fig. 3.17(c), the apparent angle decreases compared to the original contact angle applied to the carbon fiber even in all cases, considering the error range of the measured value. In addition, the angle decreases as the polar angle range broads, and the smallest angle appears at $\varphi = \pi/2 \pm 15°$ case. According to Ref. Hao and Cheng (2009b) and Hou et al. (2020), the apparent angle affects the path and time of removing liquid water from the GC. Due to the high wettability (i.e., low contact angle), liquid water sticks and delays in the GC. Although droplet removal depends on the channel structure and the flow direction (e.g., parallel or serpentine channels), a narrow polar range is more appropriate to depart from the GDL surface while creating smaller droplets and high apparent angles in this study.

3.6 Summary

A 3D multicomponent Shan-Chen LB model was used to examine the effect of the 3D micropore structure on water transport. The 3D micropore structure of GDL composed of carbon fibers was generated using a stochastic reconstruction method. The GDL structure was assembled through the random placement of straight cylinders with four different polar angle ranges of $\pi/2$ ±5°, ±15°, and ±25°, including constant $\varphi = \pi/2$. All GDL cases showed the anisotropic characteristic of the GDL in material transport and good agreement with the results of Ref. (Schulz et al., 2007).

The structural conditions of the GDL do not significantly influence the transport of liquid water within the GDL. Liquid water transport is determined mainly by capillary effects, which are influenced by the hydrophobic nature of the GDL. Furthermore, the capillary pressure drops in the through-plane direction still play a crucial role in determining the preferential path, even in a wide polar angle range. Compared to the

parallel layers of the reconstructed GDL, the carbon fiber orientation in the in-plane within the GDL maintains liquid water saturation at similar levels.

In addition, the present change in the morphological conditions of the GDL provides more specific characteristics of the apparent angle of liquid droplets after the water breakthrough. The apparent angle significantly depends on the interface between the GC and GDL determined by the applied fiber's orientations. The liquid droplet grows and covers wider as the polar range broads, representing low apparent angles. Especially the case of the ±15° range shows the lowest apparent angles in both in-plane directions, which means that the removal of liquid droplets becomes more challenging after the breakthrough.

CHAPTER 4. NUMERICAL ANALYSIS OF EFFECTIVE THERMAL CONDUCTIVITY OF THE GDL

In this chapter, the effect of saturated liquid water on the effective thermal conductivity (ETC) of gas diffusion layers (GDLs) is estimated using a developed three-dimensional multicomponent multiphase (MCMP) LBM coupled with a thermal model. The Peng-Robinson equation of state (P-R EOS) with the exact difference method (EDM) forcing scheme is adopted to consider the density ratio between each component (liquid water/air). The original objective of the developed model is to consider the high-density ratio and latent heat source due to phase change, including condensation and evaporation. However, as part of the research and development process, this study uses the developed model to investigate heat transfer without considering the phase change.

We mainly focus on the ETC of GDLs in the through-direction, adjust the wettability and orientation of the GDLs fibers and visualize the temporal changes in water distribution during heat transfer in the GDLs. The rest of this chapter is arranged as follows. The first part introduces the importance of ETC measurement and thermal management in the GDLs. The next part verifies the MCMP EDM and thermal models proposed in Chapter 2. Furthermore, the ETC of parallel and series straight cylindrical tubes in a rectangular box is validated compared to theoretical methods. Then the ETC of reconstructed GDLs used in Chapter 3 is verified under dry conditions. In the third part, we detail and discuss simulation results of saturated water and temperature distributions at various GDLs. Finally, we summarize the present study in the last part.

4.1 Introduction

The temperature inside the PEMFC keeps increasing during the operation due to electrochemical reactions. The generated heat makes the GDL dry and the

temperature gradient across the fuel cell stack, even in a single cell. The gas diffusion layer (GDL), a medium through which the generated heat transfers to the gas channel (GC), plays an essential role in thermal management in PEMFC.

As already known, the GDL is composed of carbon fiber paper/clothes. Due to this complex structural property, the heat transfer mechanism in the GDL is complicated, and there are two conjugated components (fibers and pores) in the GDL. As mentioned earlier, thermal conductivity is essential to determine the thermal anisotropic properties of GDL. Therefore, effective thermal conductivity (ETC) is measured to define the heat transfer properties of GDLs (Karimi et al., 2010; Zamel et al., 2011b; Chen et al., 2020).

Many experimental studies have been conducted to explain the thermal properties of the carbon fiber/paper microstructure. Ramousse et al. (2008) specifically measured the ETC of Teflon-treated carbon paper. According to their results, it was introduced that many researchers overestimated the theoretical ETC in the literature. Xu et al. (2014) showed experimental results of the thermal conductivity of partially saturated GDLs. They discussed the analytical expression for the theoretical maximum value of the through-plane thermal conductivity and revealed a relationship between the predicted values and experimentally measured data. Bock et al. (2018) applied commercial GDLs treated with MPL to investigate the through-plane thermal conductivity. They further presented the thermal conductivity as a function of the thickness of GDL samples. Chen et al. (2020) experimented using the Hotdisk thermal conductivity meter, and the effects of water content and temperature on its thermal conductivity were investigated in detail. However, control and measurement of microporous medium directly using the experimental tools are complicated. It takes a massive amount of time and requires careful effort to capture the changes in tiny microstructures.

In this chapter, the thermal LBM introduced in Chapter 2 is used to investigate the ETC of the microstructure GDLs. The reconstructed structure used in Chapter 3 is adopted to reveal the anisotropic material properties in the heat transfer of GDL. Furthermore, the water content, which is not considered in most of the previous works,

is included in this study to reveal the effect of the water content on the ETC of GDL during the heat transfer process. This study combines an advanced MCMP LBM with the thermal LBM to comprehensively understand water and thermal management.

4.2 Model Description

To investigate the effects of anisotropic orientation and water contents on the ETC of GDLs, the thermal LBM model is used with the MCMP EDM model of Chapter 2. In the same way, the reconstructed GDLs are composed of straight cylinders with a constant diameter of 8 μm in three-dimensional, and the total thickness of the GDL is 160 μm. The computational domain size is $170 \times 150 \times 150$ lattice units. In the EDM and thermal models, the lattice unit length, lu, is set to be "1" μm, representing the same size as the SC model. In this model, the time step (ts) of one simulation iteration is set to 1.25×10^{-8} s.

As shown in Fig. 4.1(a), the thermal conductivity is different in carbon fibers and pore regions. In this study, the pore is selected as the air with thermal conductivity of $k_f = 0.0253\ \mathrm{W/m \cdot K}$ and the thermal conductivity, $k_s = 140.0\ \mathrm{W/m \cdot K}$, is applied to the carbon fibers. Each thermal conductivity is applied using the wall

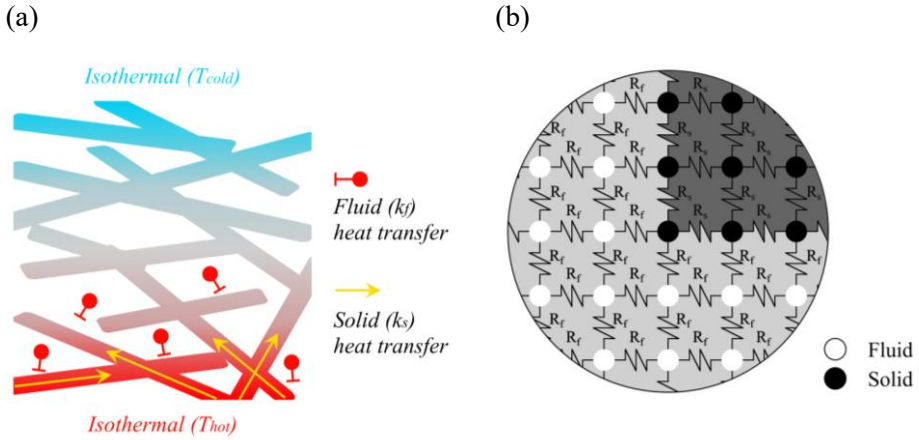

Fig.4.1. (a) Diagram of the heat transfer mechanism in GDLs, (b) the thermal resistance of lattice nodes in LBM

function, which notifies the identity of lattice nodes (Fig. 4.1(b)). It is noted that the thermal contact resistance between the attached fibers is not considered in this study (Burheim et al., 2010; Lu et al., 2021).

In this study, a one-dimensional temperature gradient is initialized to make a heat flux in the GDL. Isothermal boundary conditions are imposed on the bottom ($x = 0, T_{hot} = 335$ K) and upper ($x = X, T_{cold} = 330$ K) walls, the heat flux occurs through a temperature gradient in the *x*-direction. The whole domain except for the inlet boundary bottom wall for each simulation is initialized at T_{cold}. No additional external heat flux is applied, adiabatic conditions are implemented in the other two directions, and the unknown distribution functions of the insulated wall are calculated as introduced in Chapter 2.

The simulation is proceeded until reaching the steady-state; the steady-state is defined as the average temperature residual in the whole computational domain with a convergence of less than 10^{-5}.

$$\sum_i \left(T_i^{n+1} - T_i^n\right) / \sum_i T_i^{n+1} < 10^{-5} \tag{4.1}$$

4.3 Model Validation

Similar to the SC model, the forcing terms applied to the EDM model are verified in this part. First, the Peng-Robinson equation of state (P-R EOS) applied in the interparticle force of the EDM is compared to the Maxwell theoretical construction of pressure and density ($P - \rho$). In the following parts, the cohesion and adhesion force terms are validated by applying a static liquid droplet and measuring the contact angle on the solid wall. A static liquid droplet surrounded by an air component is performed using the MCMP EDM model coupled with the double distribution function (DDF) thermal model. In addition, static contact angles are measured while the wall wettability remains constant for selecting the appropriate adhesion force coefficient. In the last part, the comparison with the theoretical thermal conductivity model proceeds to validate a thermal model for simulating the conductive heat

transfer in the GDLs.

4.3.1 Single component phase segregation

For the validity of the interparticle force in the EDM model, the P-R EOS applied to the interparticle force is verified first among the three external forces applied to the EDM model. The density values calculated by the LBM and the theoretical Maxwell construction are compared. The Maxwell construction means equilibrium pressure under isothermal conditions below the critical temperature and is calculated by the following formula.

$$P_r^e = \frac{1}{\rho_{r,l}-\rho_{r,g}} \int_{\rho_{r,g}}^{\rho_{r,l}} P_r d\rho_r \tag{4.2}$$

where the subscript r means the reduced value, and each is defined as $\rho_r = \rho/\rho_c$, $T_r = T/T_c$, and $P_r = P/P_c$. The subscript c represents the critical point value of the equation of state, corresponding to $322\ \mathrm{kg/m^3}$, $647\ \mathrm{K}$, and $22\ \mathrm{MPa}$ for water, respectively.

At a given temperature, the equilibrium pressure is determined by the equal-area rule (i.e., area ***abc*** = area ***cde***), and an intermediate density, $\rho_{r,m}$ is also obtained (Liu, 2020). The $P_r - \rho_r$ diagram has three regions: 1) unstable region, 2) metastable region and 3) stable region (Fig. 4.2). The stable region represents the state

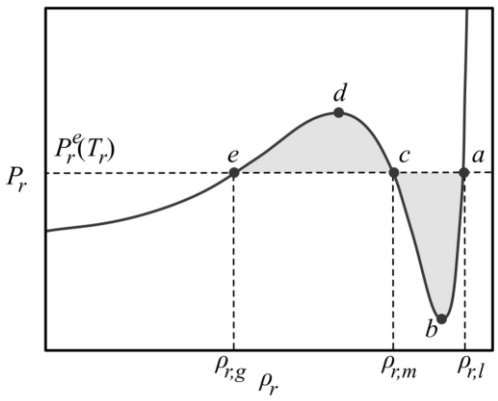

Fig.4.2. Reduced $P_r - \rho_r$ isotherm at $T_r < 1$

of saturated vapor or a liquid, where $\rho_r < \rho_{r,g}$ and $\rho_r > \rho_{r,l}$, respectively. The metastable region includes the region below the ***de*** line and the ***ab*** line. Finally, unstable means that it has a mechanically negative $\partial_\rho P$, and in this region, the fluid separates into a liquid and vapor phase (Lee and Lin, 2005; Liu, 2020).

The dimensionless coefficient, k ($k = P_c/\rho_c(\Delta t/\Delta x)^2$) was applied to Eq. (4.3) for numerical stability when using a non-ideal equation of state in the other literature (Kupershtokh et al., 2009; Stiles and Xue, 2016; Zhu et al., 2017). Instead, our model uses a weight factor, $k(T_r)$, which is a function of temperature to ensure that the effective mass is included in the unstable region and that the interface thickness of

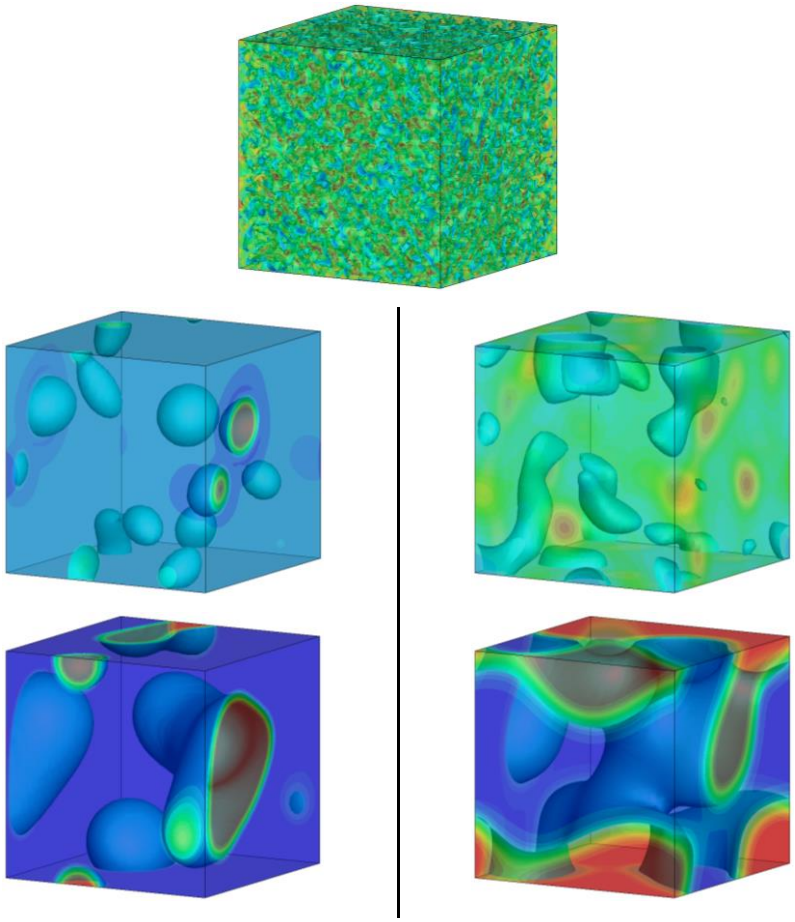

Fig.4.3. LBM results of single component phase segregation at different reduced temperatures (left: $T_r = 0.51$, right: $T_r = 0.91$)

the effective mass is considered a non-isothermal function. The order of the weight factor is curve-fitted at each temperature, and the redefined pseudopotential function is expressed as:

$$\psi^{\sigma}(\rho^{\sigma}) = \sqrt{\frac{2k(T_r)(P^{\sigma}-\rho^{\sigma}c_s^2)}{G_{\sigma\sigma}c_s^2}} = \sqrt{\frac{2{T_r}^{0.503}(P^{\sigma}-\rho^{\sigma}c_s^2)}{G_{\sigma\sigma}c_s^2}} \tag{4.3}$$

For single-component phase segregation, the water component is initially distributed randomly with a 10% fluctuation of the critical density (i.e., $\rho_c \pm 0.1\rho_c$) in a cubic domain of $100 \times 100 \times 100$, as shown in Fig. 4.3. All boundaries are set to periodic conditions, and a single relaxation time is used to consider one component with the same viscosity but different densities. Fig. 4.4 shows the equilibrium density values under different temperature conditions, and the *M*-line in Fig. 4.4 represents the intermediate value at each temperature. Phase separation occurs in the unstable region and can be divided into a liquid-like region (right side) and a vapor-like region (left side) based on the *M*-line (Liu, 2020).

The LB result is slightly different from the analysis value as it represents a mixed phase of liquid and vapor rather than a saturation value of each phase in the unstable region. However, our model shows stable phase separation due to mass transition by applied pseudopotential forces over a wide temperature range. As mentioned before, the thermal phase conductivity of the water component is determined based on the

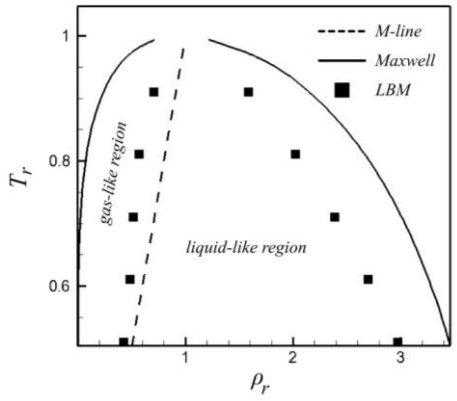

Fig.4.4. Comparison of the LB results and the Maxwell construction

equilibrium density when calculating the thermal LBM in the following part.

4.3.2 Static droplet and wall contact angle

This part tests a static liquid droplet surrounded by air in the middle of a computational domain ($150 \times 150 \times 150$) to validate the MCMP pseudopotential model using the EDM forcing scheme with the P-R EOS. A stationary droplet with a variable radius (R = 30 to 50) is performed, and periodic boundary conditions are applied in all directions without the force of gravity. The densities inside and outside the droplet for the water component are set to 7.8656 and 1.2224 at $T_r = 0.51$, obtained in the previous part. 0.001 and 0.01 are set to the densities inside and outside the droplet for the air component. The physical properties used in this work are

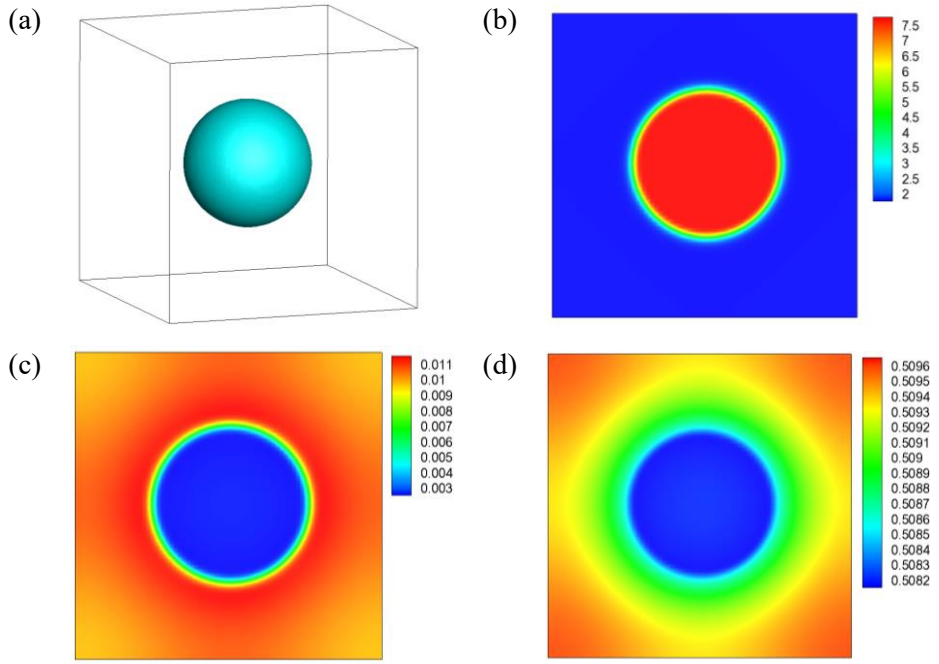

Fig.4.5. LB simulation results for the static water droplet test at $T_r = 0.51$; (a) 3D iso-surface of the mean water droplet density, (b) the contour of the density distribution of the water component, (c) the contour of the density distribution of the air component, and (d) the reduced temperature distribution

converted using the unit conversion coefficient in LBM, as described in Chapter 2. According to Eq. (4.4), the density field is initiated to smooth the density transition around the interface.

$$\rho(x,y,z) = \frac{\rho_{in}+\rho_{out}}{2} + \frac{\rho_{in}-\rho_{out}}{2} \times tanh\left(\frac{2\sqrt{(x-x_0)^2+(y-y_0)^2+(z-z_0)^2}-R}{W}\right) \quad (4.4)$$

where (x_0, y_0, z_0) is the coordinate of the droplet center, R is the radius, and W $(W = 3)$ is the width of the density interface.

Fig. 4.5 shows a liquid droplet's steady-state density and temperature distribution. When $T_r = 0.51$, and the equilibrium droplet radius is equal to 45; the result shows the most significant density ratio, 764.21 ($\rho_{water\_max}/\rho_{air\_max} = 7.7797/0.01018$). Although it is not sufficient to represent the physical density ratio between actual liquid water and air, it is much higher than in the previous SC model, which assumed that the density ratio between two different components is equal (Chen and Doolen, 1998; Sukop, 2006). The viscosity ratio, M, between two different components is defined as the ratio of the injected fluid viscosity to the displaced fluid viscosity (Sukop, 2006; Huang et al., 2009).

$$M = \frac{\mu_{injected}}{\mu_{displaced}} = \frac{\nu_{injected}\,\rho_{injected}}{\nu_{displaced}\,\rho_{displaced}} \quad (4.5)$$

In this study, the relaxation time of each component is set equal (i.e., $\nu_{injected} = \nu_{displaced}$). According to Eq. (4.5), the viscosity ratio is replaced by the density ratio. Therefore, our model could well consider and represent the effect of the viscosity ratio through the difference in density in a multicomponent multiphase situation.

The Laplace law is also used to measure the surface tension of a droplet. Fig. 4.6(a) shows the pressure difference of a static liquid droplet; the slope of each line is the surface tension according to the Laplace law and satisfies the linear relation well at any temperature. The actual surface tension of liquid water in the air at 25 ℃ ($T_r = 0.46$) is 0.072 $\mathrm{N/m^2}$; however, it is slightly overestimated and amounted to 13.357 (0.08551 $\mathrm{N/m^2}$) at $T_r = 0.51$. Although, the linear relationship between the surface tension and the temperature is well illustrated in Fig. 4.6(b). Furthermore,

Table 4.1. Interface thickness at different reduced temperatures

T_r	0.51	0.61	0.71	0.81
Interface thickness, W	3.36	3.82	4.65	7.07

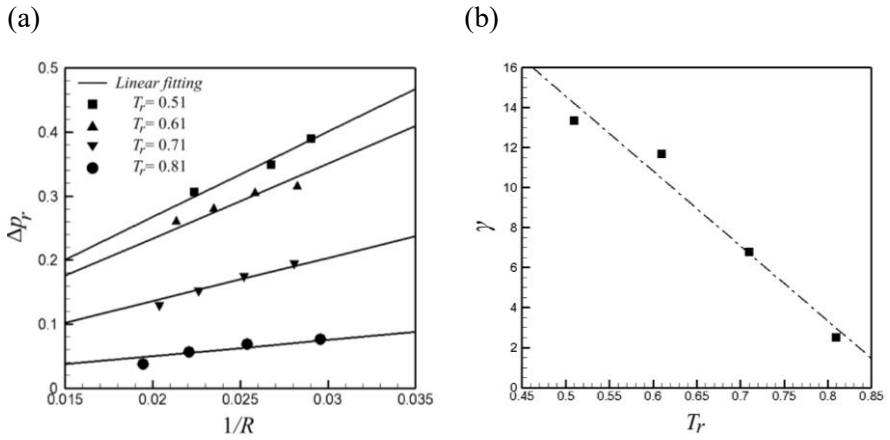

Fig.4.6. Laplace's law results in a static liquid droplet in free gravity. (a) relationship between the pressure difference inside and outside the droplet and the radii for different reduced temperatures and (b) relationship between surface tension and reduced temperature

the interface thickness of the liquid water in Table 4.1 becomes thicker as the temperature increases, representing the water component's thickened vapor film according to the high temperature.

Similar to the measurement proceeded in the SC model, the measurement of the contact angle of the EDM model is also carried out at the constant wall wettability. In a domain size of $150 \times 150 \times 75$, the half water droplet is placed on the bottom wall with the same initial densities as the previous chapter. The coefficient, G_{adh}^{σ}, in adhesion force term, is adjusted to control the wettability, and the virtual wall density is set equal to water vapor or air for each component. Fig. 4.7(a) shows the contact angle corresponding to the water component's G_{adh}^{1}, and a negative value of G_{adh}^{1}

has been applied to the air component (i.e., $G_{adh}^{2} = -G_{adh}^{1}$). As explained earlier, the surface tension decreases with increasing temperature. Accordingly, it can be seen that the wettability also tends to decrease with increasing temperature (Fig. 4.7(b)). The obtained results indicate that our model used in this study can sufficiently simulate the characteristics and temperature effect of an MCMP flow.

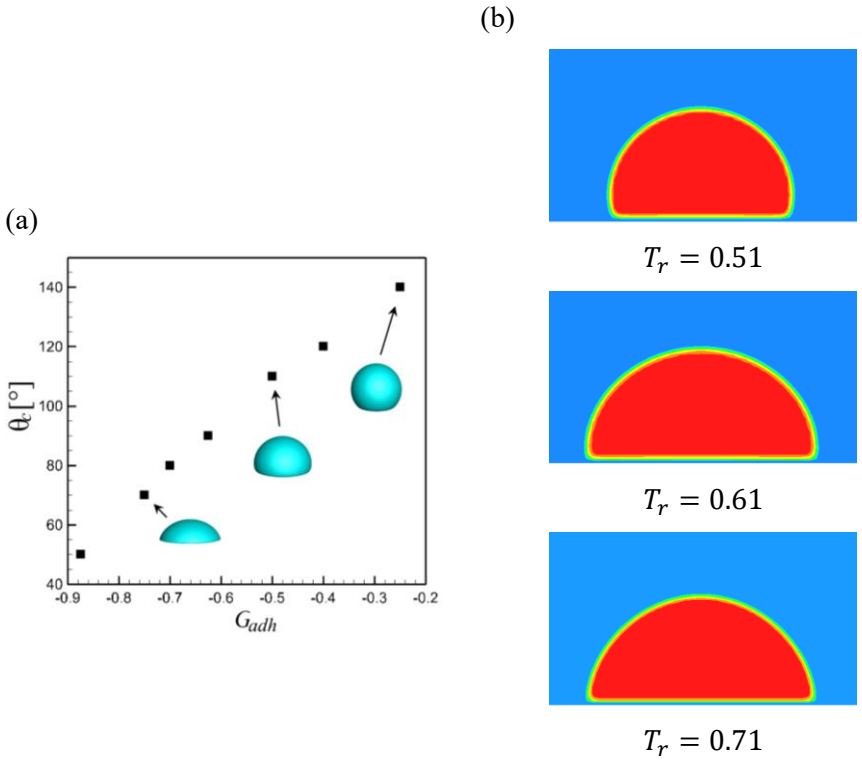

Fig.4.7. (a) Static liquid droplet on a wall with various adhesion coefficients, G_{adh}^{1}, (b) temperature effect on the wall wettability at $G_{adh}^{1} = -0.5$

4.3.3 Effective thermal conductivity (ETC)

Before assessing the effect of water contents and anisotropic orientation of GDLs, the single component thermal LBM results are evaluated using the ETC series/parallel analytical model and the Maxwell-Eucken (ME) model for solid-fluid conjugate heat conduction. The straight cylinders are distributed randomly, and three samples with the same number of cylinders but different locations are used in this part (Fig. 4.8).

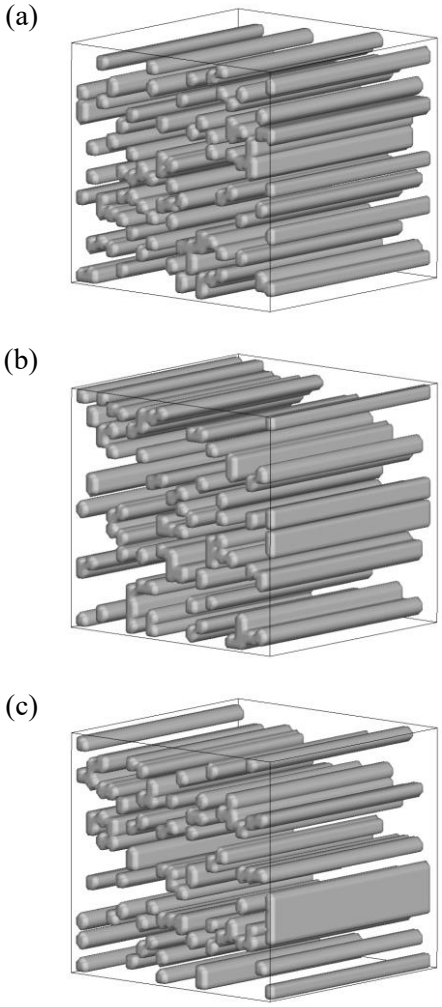

Fig.4.8. The structures of straight cylinder representing the non-oriented carbon fibers, (a) sample #1, (b) sample #2, and (c) sample #3

Series and parallel models are proposed to simplify the complex microstructure of the composite material (Deissler and Boegli, 1958). In this model, the solid-fluid interfaces are perpendicular or horizontal to the heat flux direction. The predicted ETCs represent the highest and lowest values for the solid-fluid composite material (Pfrang et al., 2011). Theoretical series and parallel models are expressed in Eqs. (4.6) and (4.7), respectively (Deissler and Boegli, 1958):

$$k_{eff} = \frac{k_f \cdot k_s}{\phi_s \cdot k_f + (1-\phi_s) \cdot k_s} \tag{4.6}$$

$$k_{eff} = (1 - \phi_s) \cdot k_f + \phi_s \cdot k_s \tag{4.7}$$

where k_f and k_s represent the thermal conductivity of the fluid and solid phases and ϕ_s is the volume fraction of the solid phase.

In contrast to the above models, the effective medium theory (EMT) model assumes a random interspersing of two different components (Kiradjiev et al., 2019).

$$k_{eff} = \frac{1}{4}\Big(3\phi_s\big(k_f - k_s\big) + \big(2k_s - k_f\big) + \sqrt{\big[3\phi_s\big(k_f - k_s\big) + \big(2k_s - k_f\big)\big]^2 + 8k_f k_s}\,\Big) \tag{4.8}$$

The ME model is one of the most widely used approaches to efficiently approximating means for predicting ETC composites (Maxwell, 1881). It is derived from the effective electric resistivity of a sphere containing *N* spherical particles based on the theory of electric potential satisfying the Laplace equation and can be expressed as:

$$k_{eff} = k_s \cdot \frac{2k_f + k_s + 2\phi_s \cdot (k_s - k_f)}{2k_f + k_s - \phi_s \cdot (k_s - k_f)} \tag{4.9}$$

where k_f and k_s represent the thermal conductivity of the matrix and periodically dispersed spherical fillers and ϕ_s is the filler volume fraction. This model can be applied when one of the materials is diluted in the other, converting k_f to k_s using $\phi_s \leftrightarrow 1 - \phi_s$. The ME model is particularly effective in predicting the ETC of

composite materials reinforced with a small volume fraction of well-dispersed particles (Ke and Duan, 2019).

For the sake of generalization, three different samples are reconstructed as described in Fig. 4.8, and all the fibers do not have any aligning angles as described previously. The carbon fibers are arranged in 20 layers, with five fibers in each layer. The carbon fiber's diameter is 8 μm, and the total GDL thickness is 160 μm. The computational domain for the through-plane direction is $150 \times 150 \times 170$, and $150 \times 160 \times 160$

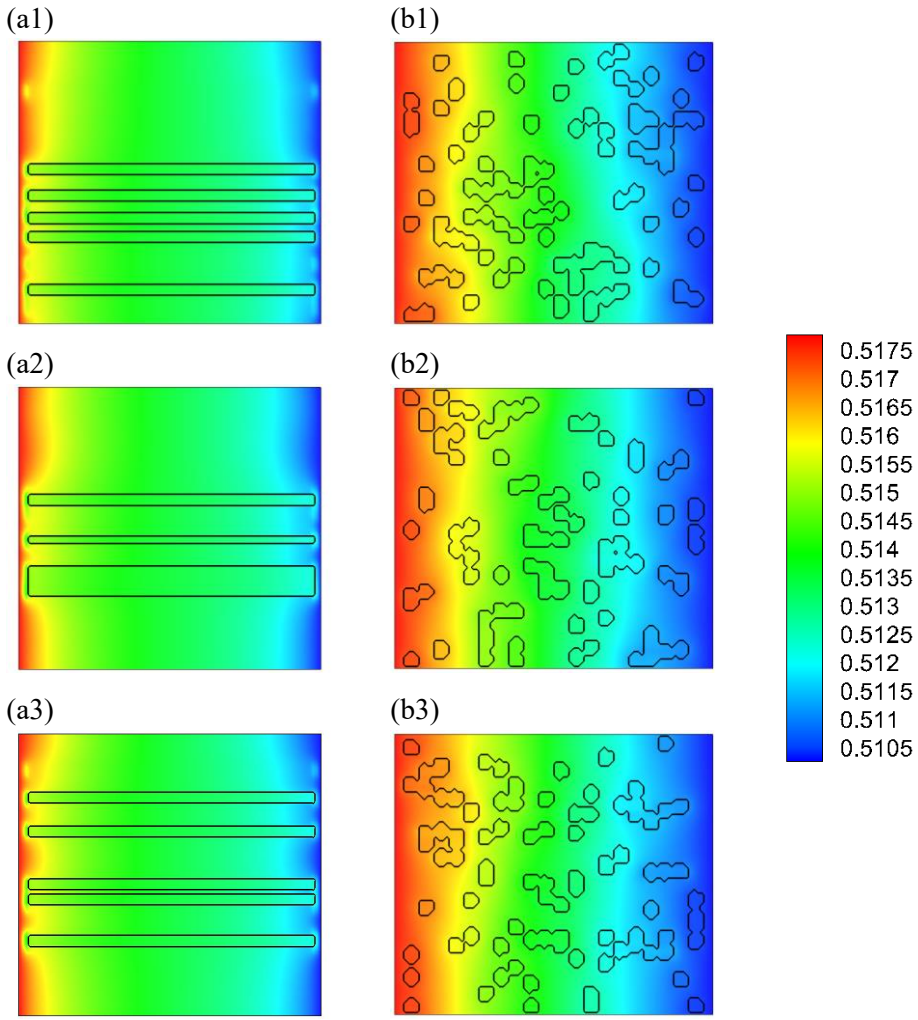

Fig.4.9. Central cross-sectional temperature distribution of non-rotated fibers in dry conditions (a) in-plane direction, (b) through-plane direction

is set for the in-plane direction. As described in the Model Description, isothermal boundary conditions are imposed on the bottom and upper sides in the heat flux direction. Each side is set to $x = 0, T_{hot} = 335\ \mathrm{K}$ and $x = X, T_{cold} = 330\ \mathrm{K}$, respectively.

Fig 4.9 shows the steady-state temperature distribution of cross-sectional in- and through-plane. As shown in Fig. 4.9, each sample has the same number of fibers, but the location of the fibers is different. The heat is transferred through the carbon fiber, and the in-plane temperature difference is more significant than the through-plane. The tendency of heat transfer through carbon fibers is visible in the through-plane. The region where the fibers overlap shows a high temperature, indicating that the compression of the GDL could affect the thermal conduction of the GDL.

The calculated ETC values using thermal LBM are compared with the analytical solution presented in Fig. 4.10. The GDLs porosity indicates $1 - \phi_s$, and ranges from 0.768 to 0.7865. The thermal conductivity of the solid material normalizes the predicted ETC. The thermal conductivity of the in-plane direction is much higher than that of the through-plane direction. It shows the thermal anisotropy properties of the GDL well. Furthermore, the result presents that optimizing the ETC of the through-

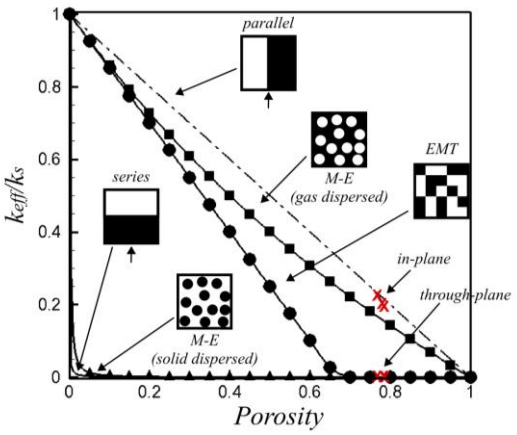

Fig.4.10. Comparison of the theoretical model and the effective thermal conductivity of each sample (white: pore, black: solid, in the schematic figure of the theoretical models)

plane direction is essential for better thermal management in the GDL of PEMFC. While it is also essential to understand the in-plane thermal conductivity as the heat transfer is predominantly through-plane, we focus on the ETC of the through-plane direction in the next part. Subsequent LBM results are compared with the EMT, M-E (solid dispersion), and series models.

4.4 Results and Discussion

In the following part, the thermal LBM is performed to investigate the effect of the orientation angle of the distributed fiber and saturated water content on the thermal conductivity properties of the GDLs, especially on the ETC of the through-plane direction. The three samples in each case are regenerated using the stochastic reconstruction model in the same way as in Chapter 3.

4.4.1 Effect of the orientation angle toward the heat flux

An orientation angle is applied in this part, which can be expressed as an azimuthal angle, θ, and a polar angle, φ as introduced in the previous chapter. These angles are perpendicular and parallel to the heat transfer direction, respectively. The random distribution of the azimuthal angle is established, and the polar angle is changed to investigate the ETC of the through-plane direction in each sample. The anisotropy characteristic of the reconstructed GDL is proved in Chapter 3, and the same samples are applied to this part. We assume that the computational domain is under a dry condition, and the PTFE content and compression effects are not considered in this part. The material properties and boundary conditions are used in the same way as in the Model Validation.

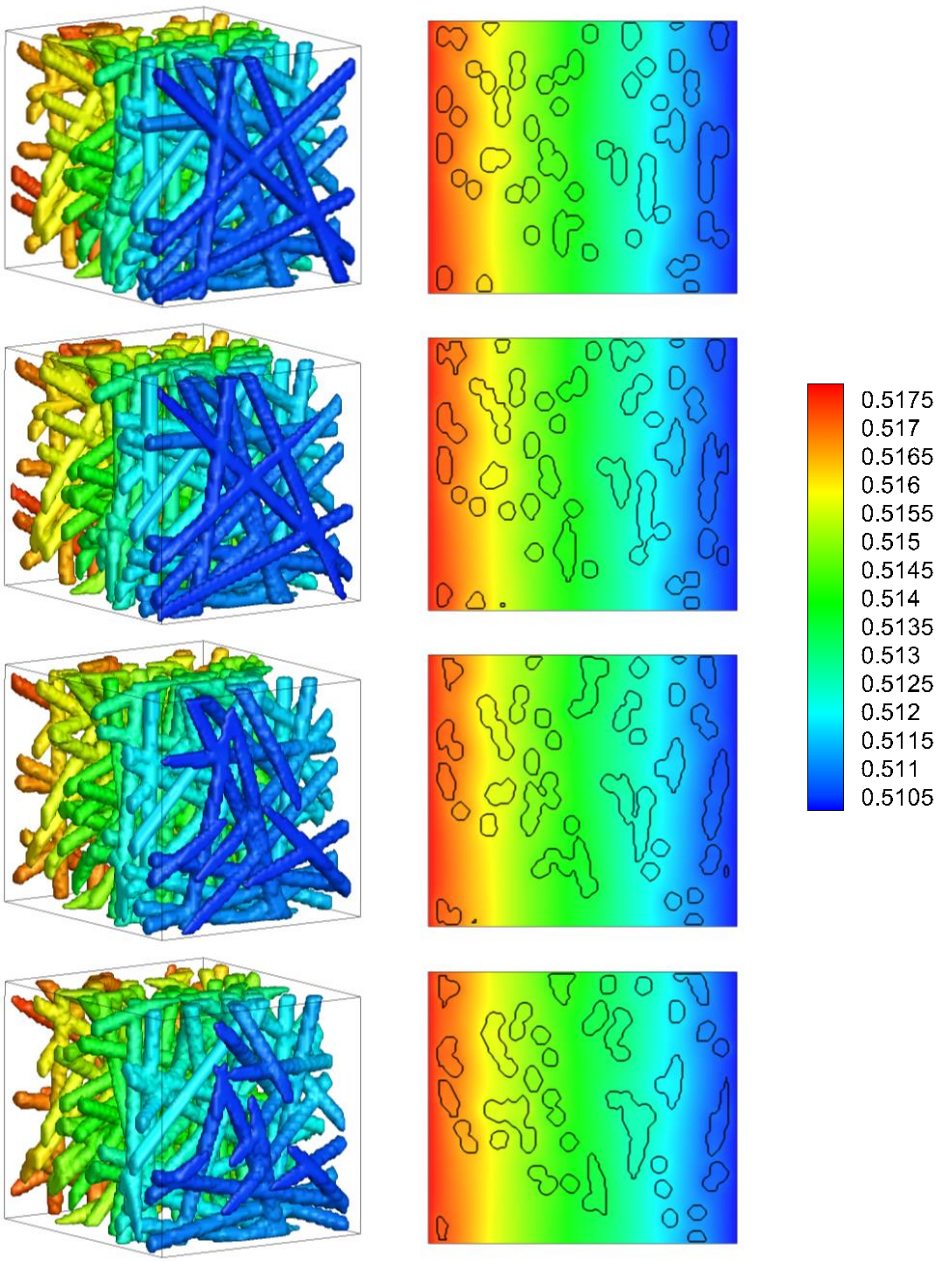

(a) (b)

Fig.4.11. (a) Steady-state temperature distribution of sample #1 with different orientation angles in the through-plane direction, (b) temperature contour of the central cross-section in the through-plane direction (from top: $\pi/2$ ±0°, ±5°, ±15°, and ±25°)

The steady-state temperature distribution is presented in Fig. 4.11 and shows the linear temperature distribution towards the heat flux. As previously described, heat transfer occurs preferably in the area of the overlapping fibers. The temperature gradient of a single fiber becomes more pronounced as the polar angle range increases, even in the in-plane direction at the exact thickness layer location. In all cases, the volume-averaged temperature increases by about $2.44\,℃$ compared to the initial volume-averaged temperature of the GDLs. The temperature drop in the through-plane direction corresponds to $4.445 - 4.523\,℃$ in dry conditions. The volume-averaged temperature and temperature drop do not differ within $0.1\,℃$, but a predicted ETC varies significantly with the applied fiber orientation.

Fig. 4.12 represents the results of the ETC with various polar angle ranges. As shown in Fig. 4.12, the polar angle range widens along the direction of the arrowheads, and the predicted ETC increases with the fiber's allocation in the heat flux direction. This indicates that the heat generated at the CL and GDL interface as a result of a chemical reaction is more easily released by the carbon fiber. When comparing the zero range and $\pm 5°$ range cases, the ETC decrease only occurs between these two cases. In this study, the contact resistance between fibers is not considered. In the case of the 0

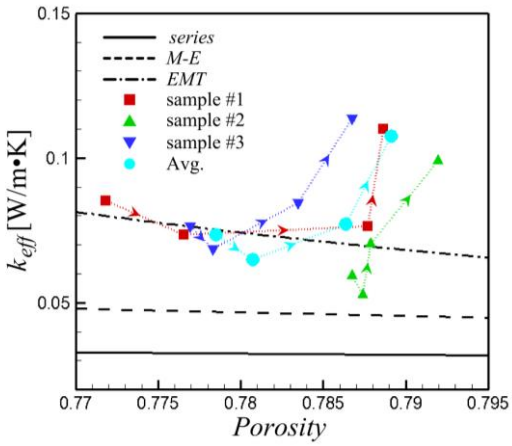

Fig.4.12. The effective thermal conductivity according to the fiber orientation angles in the through-plane direction (Arrowheads indicate the increase of the fiber orientation in the through-plane direction)

range, the fibers are considered perfectly connected in an ideal state for each layer. However, in $\pm 5°$ range cases, a slight gap is made between layers as an applied polar range. Incomplete contact of the fiber layers is compensated by applying a polar range of fibers greater than $\pm 15°$.

The cross-sectional shape of cylindrical fibers has ellipsoidal particles like the real GDLs due to the fiber angle variations in both through- and in-plane directions (Fig. 4.11(b)) (Ke and Duan, 2019). In theoretical methods, it is assumed that the spherical particles are distributed (Maxwell, 1881; Kiradjiev et al., 2019). As a result, the difference between the theoretical models and the predicted values occurs because the cross-sectional shape of the fiber is changed as the polar angle range increases. Even though there is a difference in the absolute predicted value from the theoretical model, based on the same fiber orientation range, ETC's predicted value increases as the porosity decrease in a similar trend to the theoretical model.

Although the measured conditions are not identical (e.g., operating temperature, GDL porosity, and mean fiber diameter), the predicted values, when using the distribution range angle above $\pm 15°$, agree with the experimental results of $0.07121 - 0.132\ \mathrm{W/m \cdot K}$ in the uncompressed dry condition of GDLs (Xu et al., 2014). This result suggests that it is essential to consider the anisotropic properties depending on the orientation angle of the fibers to reflect the effect of the three-dimensional morphological condition (Didari et al., 2012). The results of this thermal analysis model well represent the heat conduction process according to the carbon fiber orientation angle of the anisotropic 3D GDL. In addition, it is suggested to apply the geometric coefficient of the particle cross-section to the ETC model.

4.4.2 Effect of the water content on the ETC

In contrast to the above cases, we adopt a DDF thermal model to consider the water component's influence on the ETC of GDLs. We assume the critical density is initiated on the whole domain for the water component to perform the phase separation. In addition, no additional fluid flows are considered to maintain the

component portion and ensure a specific saturation level of the water component. The density value of the air component is initialized to 0.01. The boundary condition of the thermal model is applied the same as in the previous case. For the additional MCMP model, the bounce-back condition is applied to the carbon fibers and the isothermal walls, and the periodic condition applies to the adiabatic walls.

Furthermore, the wettability of GDLs is also applied in this section, and two scenarios are considered hydrophilic ($\theta_c = 80°$) and hydrophobic ($\theta_c = 140°$) cases. According to Maxwell's construction, a thermal conductivity of $0.598\ \mathrm{W/m \cdot K}$ of liquid water is used at the lattice node when the density of the water component is greater than the intermediate value. Otherwise, consider the node as water vapor and use the thermal conductivity of the air at the node.

The energy source term, including the latent heat due to vapor-liquid phase change (i.e., vapor condensation and liquid evaporation), is defined as follows:

$$S_T = \varepsilon \dot{m}_{H_2 0} H_{fg} \tag{4.10}$$

where ε is porosity, and $\dot{m}_{H_2 0}$ is interfacial phase change mass transfer rate $[\mathrm{kg}/(\mathrm{m}^3 \cdot s)]$. H_{fg} is the latent heat of phase change ($H_{fg} = 307.09(1 - T_r)^{0.35549}[\mathrm{kJ/kg}]$) (Khajeh-Hosseini-Dalasm et al., 2010; Jiao et al., 2021). Although the latent heat is considerable and corresponds to $2{,}441.37 - 2{,}389.48\ \mathrm{kJ/kg}$ in the PEMFC operating temperature ($60 - 80\ ℃$), it is released when vapor condenses, acting opposite to the latent heat of vaporization as simply the additive inverse. The heat used by the fuel cell internally for water evaporation portion, by $5\ \%$ of total generated heat, is negligible in our condition (at very low current density ($< \sim 0.2\ \mathrm{A/cm^2}$)) (Mench, 2008; Islam et al., 2015; Bvumbe et al., 2016). Our computational domain is an isolated system; water components are aggregated into liquid as much as phase-separated into gas. Thus, mass conservation is satisfied and latent heat inhaled and released can be canceled.

4.4.2.1 ETC with various fiber orientations

Figs. 4.13 and 4.14 show the temperature and water component distribution in the GDL, which has zero polar angle ranges at various times. These results also present the heat transfer process during phase segregation of the water component. In this

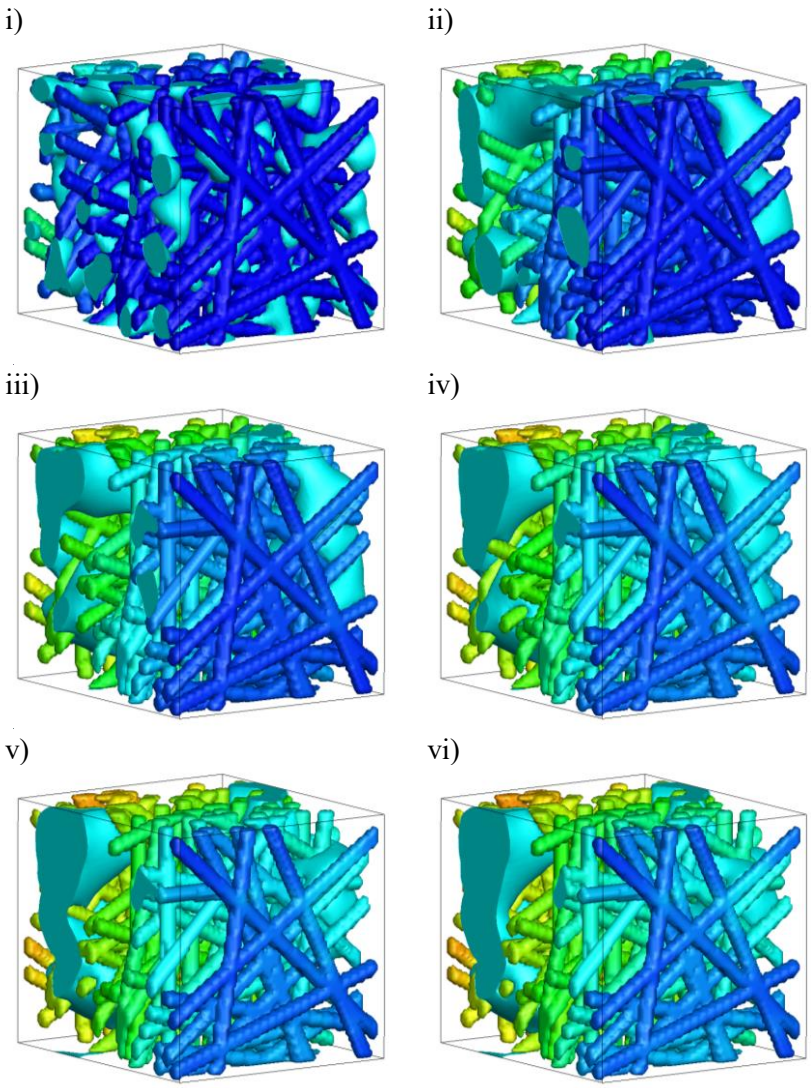

Fig.4.13. Time evolutions of the liquid water droplet and heat transfer through the GDL having $\varphi = \pi/2 \pm 0°$ and $\theta_c = 80°$ ((i) 0.1×10^5 ts, (ii) 1×10^5 ts, (iii) 2×10^5 ts, (iv) 3×10^5 ts, (v) 4×10^5 ts, (vi) 5×10^5 ts)) (10^5 ts indicates 1.25 ms)

study, the phase separation in the unstable region previously described indirectly represents the actual phase change because the density of the water component separates from the initial critical value to a near-saturated vapor or liquid density during phase segregation.

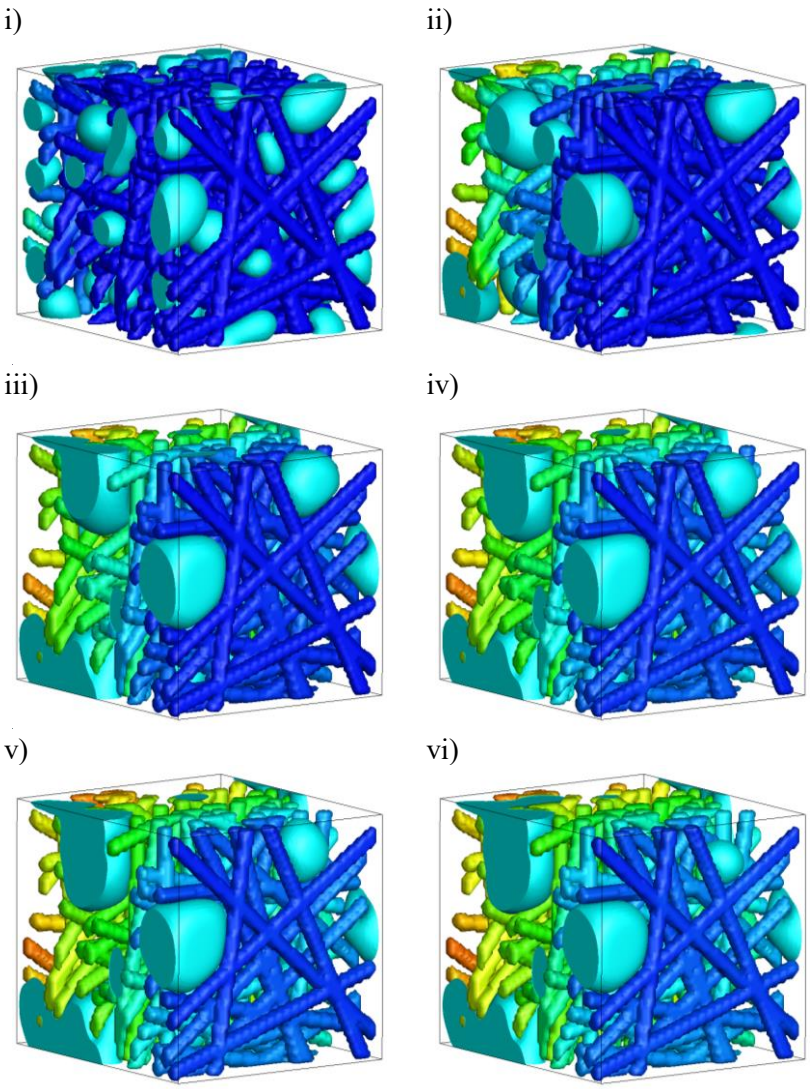

Fig.4.14. Time evolutions of the liquid water droplet and heat transfer through the GDL having $\varphi = \pi/2 \pm 0°$ and $\theta_c = 140°$ ((i) 0.1×10^5 ts, (ii) 1×10^5 ts, (iii) 2×10^5 ts, (iv) 3×10^5 ts, (v) 4×10^5 ts, (vi) 5×10^5 ts)) (10^5 ts indicates 1.25 ms)

When the fibers are hydrophilic, the liquid water agglomerates initially attach to the fiber surface and then merge (Fig. 4.15). When the water component sufficiently forms a specific liquid droplet, it spreads out continuously toward the large pores with a low capillary resistance force ($P_c = -2\gamma cos\theta_c/R$). On the other hand, the size decreases and evaporates when there is insufficient liquid water to maintain its formation. The above series of processes indicates the same phenomena of generation, growth, coalescence, and transport of the liquid droplet on a plane with a uniform contact angle (Feng and Bhushan, 2020; Jiao et al., 2021b).

The water phase segregation and the liquid water droplet formation in the hydrophobic case slightly differ in the hydrophobic condition. The liquid water coheres with each other much more due to the high capillary resistance force corresponding to the contact angle of the fibers. As a result, fewer liquid droplets are formed and accumulate on the carbon fiber surface (Fig. 4.16). In terms of the air component, as the liquid droplet grows and spreads out to relatively large pores, the regions occupied by air are replaced by agglomerated droplets (Figs. 4.17 and 4.18). In addition, it can be seen that the distribution of aggregated liquid water is affected by the pores' shape according to the fiber arrangement, as shown in Appendix, Figs. A1 – A12.

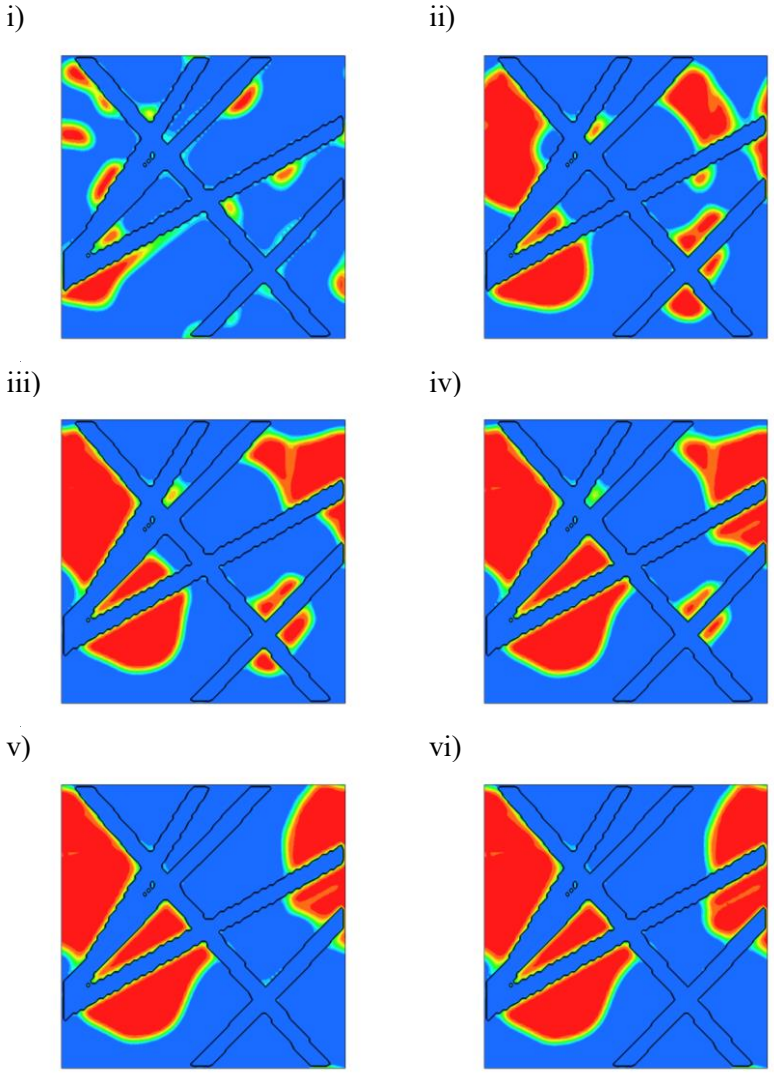

Fig.4.15. Liquid water distribution in a cross-section of the through-plane in the GDL having $\varphi = \pi/2 \pm 0°$ and $\theta_c = 80°$ ((i) 0.1×10^5 ts, (ii) 1×10^5 ts, (iii) 2×10^5 ts, (iv) 3×10^5 ts, (v) 4×10^5 ts, (vi) 5×10^5 ts)) (10^5 ts indicates 1.25 ms)

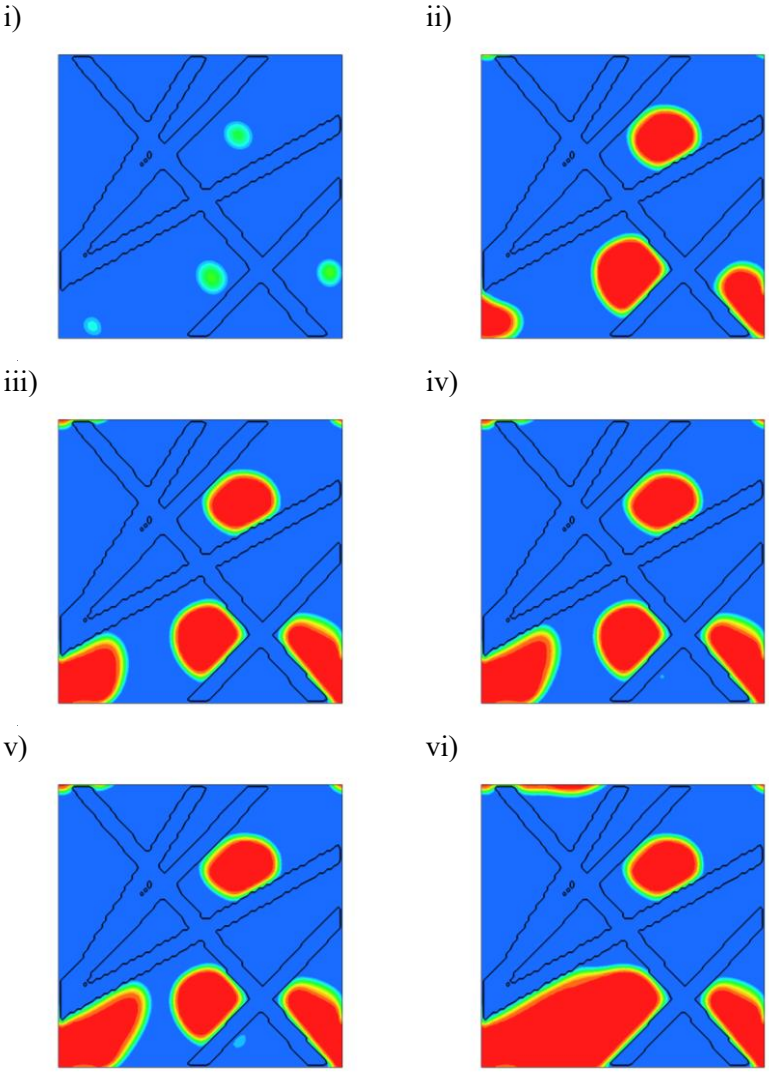

Fig.4.16. Liquid water distribution in a cross-section of the through-plane in the GDL having $\varphi = \pi/2 \pm 0°$ and $\theta_c = 140°$ ((i) 0.1×10^5 ts, (ii) 1×10^5 ts, (iii) 2×10^5 ts, (iv) 3×10^5 ts, (v) 4×10^5 ts, (vi) 5×10^5 ts)) (10^5 ts indicates 1.25 ms)

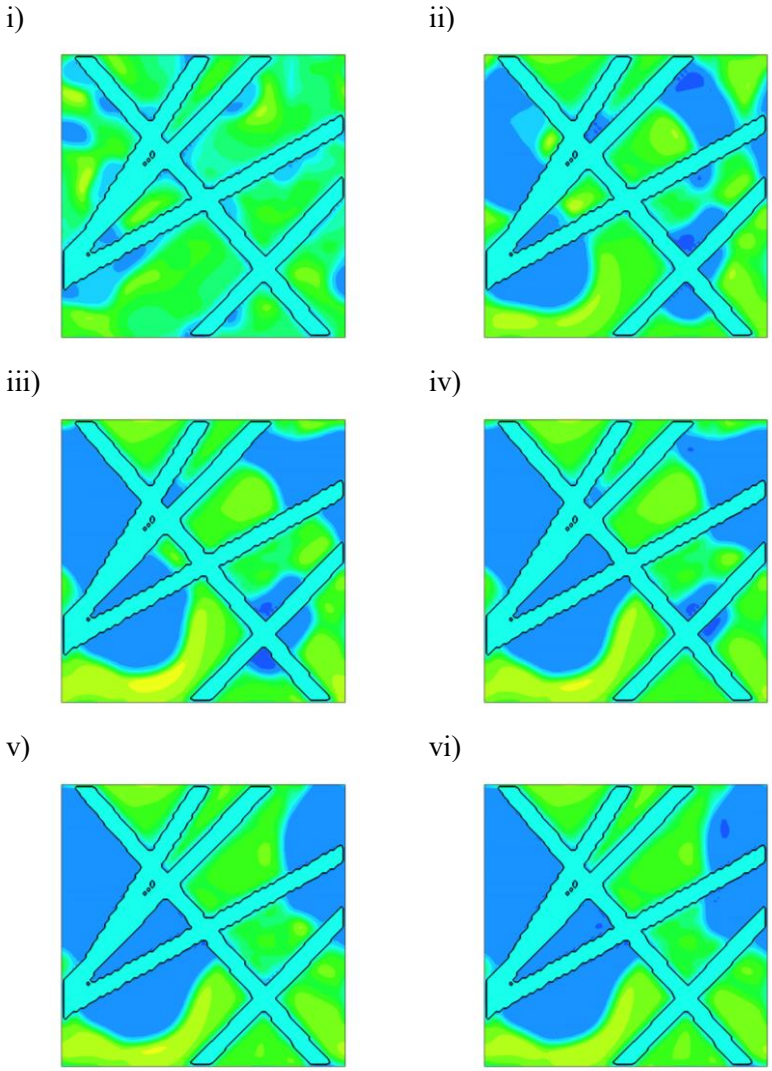

Fig.4.17. Air component distribution in a cross-section of the through-plane in the GDL having $\varphi = \pi/2 \pm 0°$ and $\theta_c = 80°$ ((i) 0.1×10^5 ts, (ii) 1×10^5 ts, (iii) 2×10^5 ts, (iv) 3×10^5 ts, (v) 4×10^5 ts, (vi) 5×10^5 ts)) (10^5 ts indicates 1.25 ms)

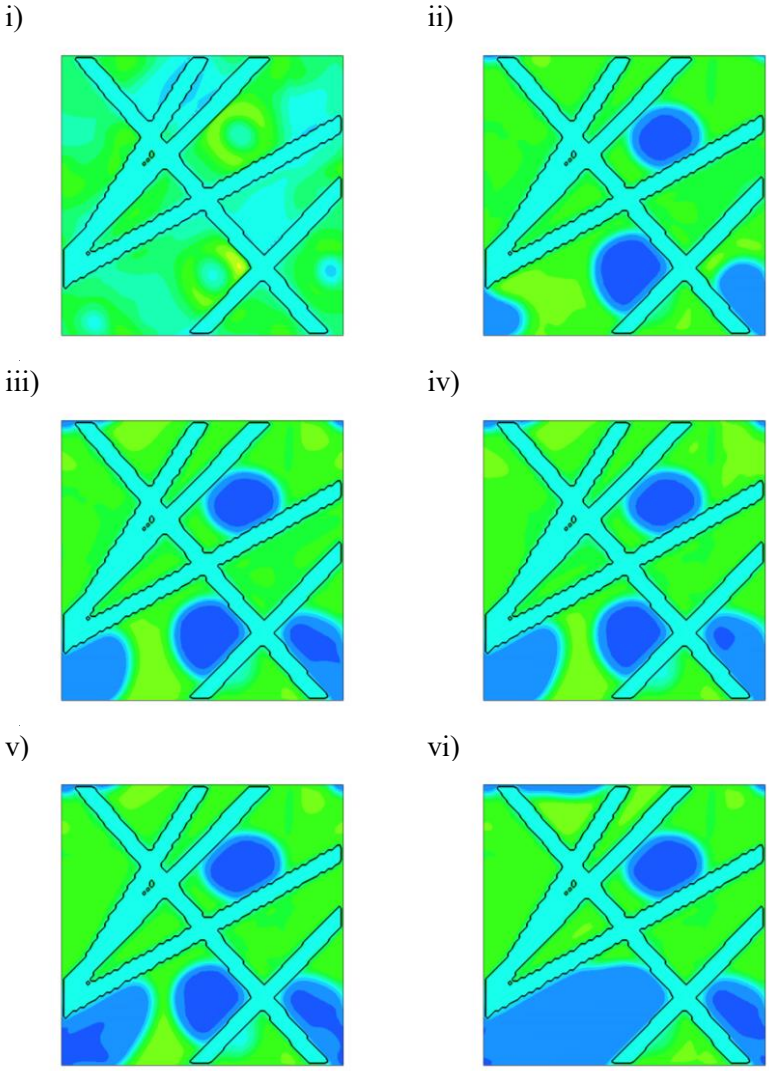

Fig.4.18. Air component distribution in a cross-section of the through-plane in the GDL having $\varphi = \pi/2 \pm 0°$ and $\theta_c = 140°$ ((i) 0.1×10^5 ts, (ii) 1×10^5 ts, (iii) 2×10^5 ts, (iv) 3×10^5 ts, (v) 4×10^5 ts, (vi) 5×10^5 ts)) (10^5 ts indicates 1.25 ms)

As mentioned earlier, when the GDL is hydrophilic, the water droplet fills the pores more widely. Conversely, liquid water is more merged in hydrophobic cases, and a few water droplets are formed. Compared to Ref. Ziegler and Gerteisen (2009), the characteristic of the liquid water formation related to the fiber's wettability is very similar to the experimental result (Fig. 4.19).

In terms of thermal conductivity, the conductivity of liquid water is much higher than that of the air; the heat is transferred along the fibers, which preferably contain attached liquid water (Fig. 4.20). The thermal conductivity mechanism in GDLs with hydrophobicity is similar to that of hydrophilic conditions, as shown in Fig. 4.21. In addition, the temperature gradient appears not only in the heat flux direction but also in the change of position due to the movement of the liquid droplet.

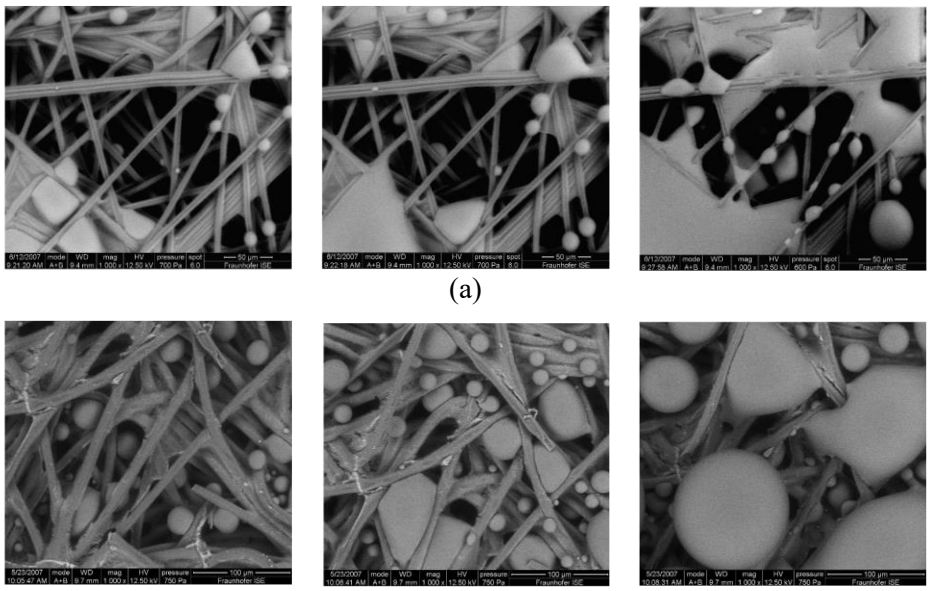

Fig.4.19. Reproduced ESEM images of liquid water from Ref. C. Ziegler and D. Gerteisen (2009) (a) the untreated Toray TGP-H-090 GDL, (b) a hydrophobic Freudenberg H2315 I3 GDL

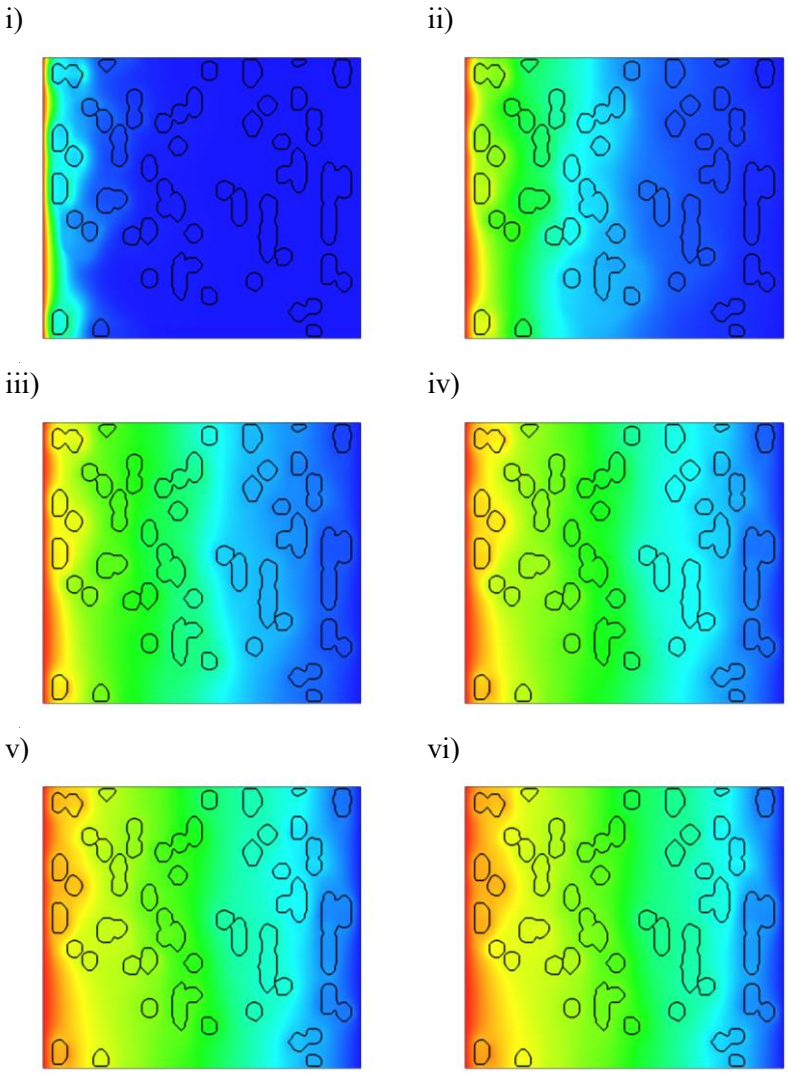

Fig.4.20. Temperature distribution of a cross-section of the in-plane in the GDL having $\varphi = \pi/2 \pm 0°$ and $\theta_c = 80°$ ((i) 0.1×10^5 ts, (ii) 1×10^5 ts, (iii) 2×10^5 ts, (iv) 3×10^5 ts, (v) 4×10^5 ts, (vi) 5×10^5 ts)) (10^5 ts indicates 1.25 ms)

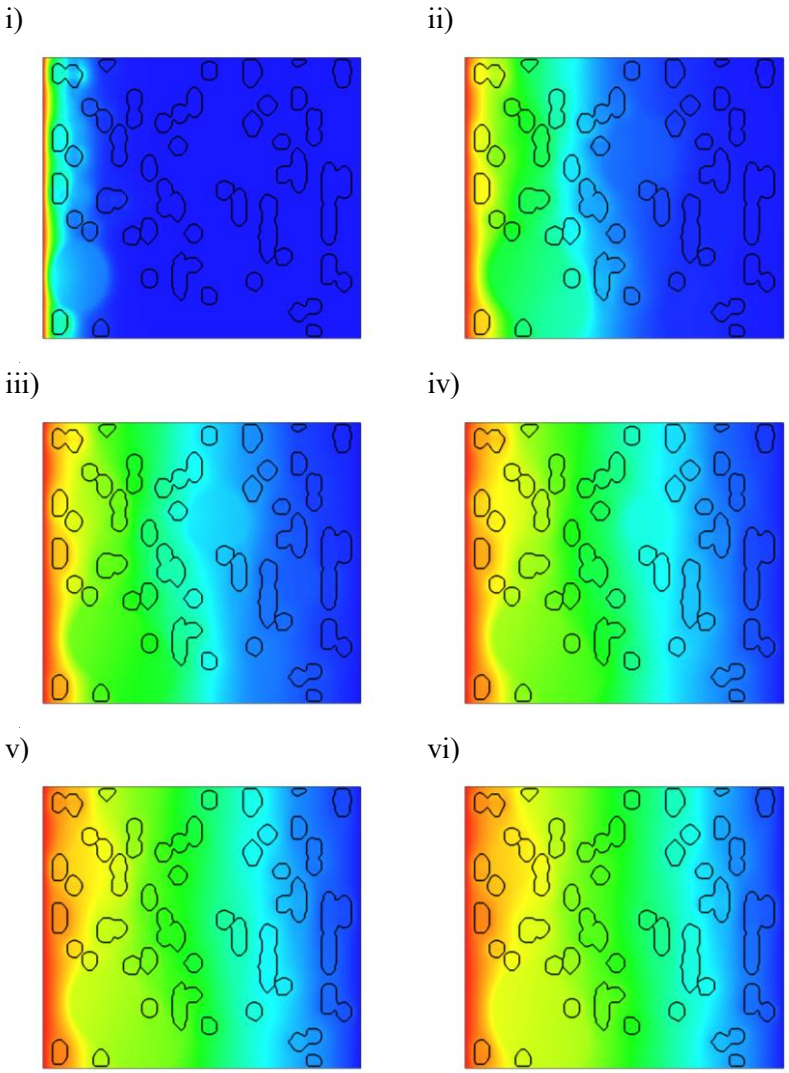

Fig.4.21. Temperature distribution of a cross-section of the in-plane in the GDL having $\varphi = \pi/2 \pm 0°$ and $\theta_c = 140°$ ((i) 0.1×10^5 ts, (ii) 1×10^5 ts, (iii) 2×10^5 ts, (iv) 3×10^5 ts, (v) 4×10^5 ts, (vi) 5×10^5 ts)) (10^5 ts indicates 1.25 ms)

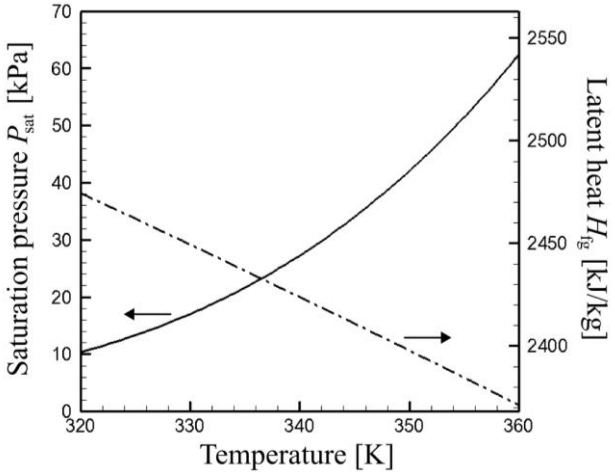

Fig.4.22. Saturation pressure and latent heat *vs*. temperature for water

In wet conditions, the temperature drop according to the GDL's wettability is $3.84 - 4.04$ ℃ at hydrophilic and $4.19 - 4.34$ ℃ at hydrophobic in the through-plane direction, respectively. The vapor saturation pressure, P_{sat} [Pa] has a relationship with the temperature, T [K], and it is expressed as follows in the form commonly seen in the literature (Jithesh et al., 2012; Jiao et al., 2021a).

$$P_{sat} = -2846.4 + 411.24(T - 273.15) - 10.554(T - 273.15)^2 + 0.166636(T - 273.15)^3 \quad (4.11)$$

Eq. (4.11) indicates the reference of the vapor condensation and water evaporation according to the local temperature and pressure. If the local pressure is greater than the saturation pressure for the local temperature, condensation of water vapor occurs, and conversely, evaporation occurs if it is less than the saturation pressure. The saturation pressure difference corresponding to the local temperature drop is approximately $3.46 - 3.95$ kPa at the low operating temperature of 60 ℃.

The volume-averaged temperature of humidified conditions is quite similar to that of dry conditions and likewise increases by 2.33 ℃ up to 2.54 ℃. In addition, the volume-averaged temperature and temperature drop between the dry and humidified conditions do not differ within 0.3 ℃; the saturation pressure difference is also insignificant under this condition.

The morphological state of GDL also plays an essential role in adequately managing heat and mass transfer in GDL. The water content corresponding to the wettability of the GDL acts as a binder linking the fibers, and even though the relative saturation level of the GDL is about the same, the water distribution plays a more critical role in determining the heat transfer of the GDL.

As shown in Fig. 4.23, the water saturation distribution depended on the wettability and pore morphology. The water saturation is averaged by all three samples in each applied polar angle range. The *x*-axis represents the relative position normalized by the GDL thickness and is selected from the center of the first fiber layer to the center of the last fiber layer to ignore the influence of the interface between the isothermal wall and the GDL.

When comparing Figs. 4.23(a) and (b), the higher the hydrophilicity of the fiber, the greater the difference in the distribution of saturated water in each sample. This indicates that the water saturation distribution is more affected by the hydrophilic GDL structure by comparing it with the averaged porosity profile shown in Fig. 4.24. The predicted ETC varies significantly with the applied GDL's wettability. When the GDL has lower wettability, the liquid water saturation level decreases, leading the hydrophobic GDLs to get a lower ETC than the hydrophilic GDLs (Fig. 4.25)

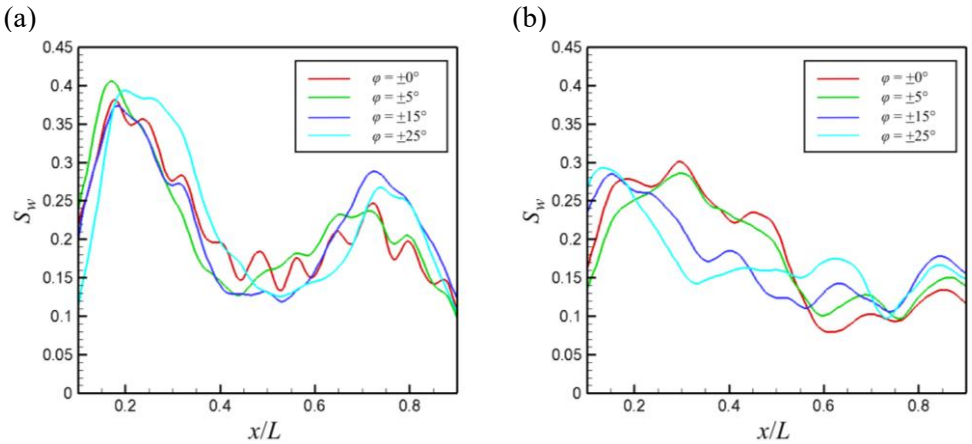

Fig.4.23. Averaged water saturation distribution along the through-plane direction with various polar angle ranges, (a) hydrophilic, (b) hydrophobic

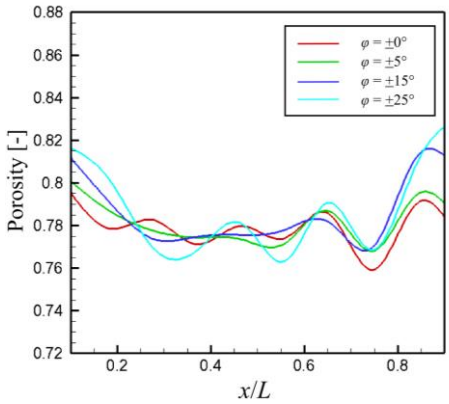

Fig.4.24. Averaged porosity profile along the through-plane direction with various polar angle ranges

(Burheim et al., 2010; Xu et al., 2014; Chen et al., 2020).

Furthermore, when the liquid water is more evenly distributed at similar saturation levels, the generated heat is better dissipated through the carbon fiber, resulting in higher ETC values (Table 4.2 and 4.3). The lowest predicted ETC value and other values were compared for each case. The value differs by at least 1.78 % and up to 35.28 % in the hydrophobic case; in the hydrophilic case, it varies by at least

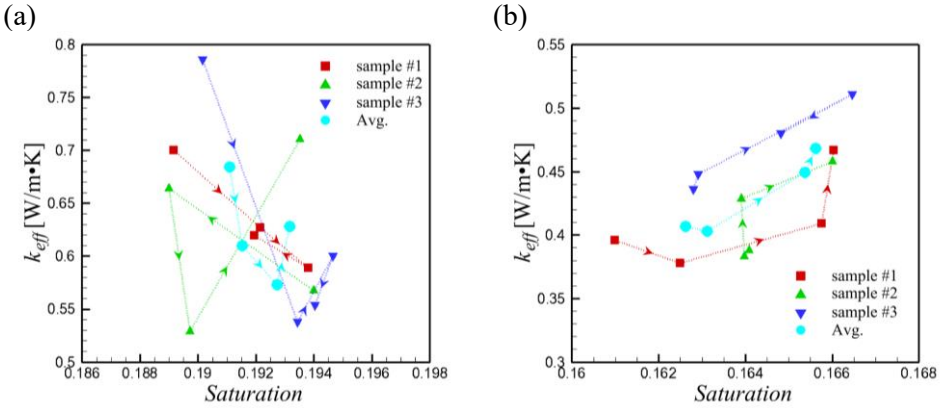

Fig.4.25. The effective thermal conductivity of GDLs which depends on the wettability of carbon fibers and the corresponding saturation level, (a) hydrophilic, (b) hydrophobic, (Arrowheads indicate the increase in the fiber orientation towards the through-plane)

1.47 % and up to 48.67 %.

Table 4.2. The standard deviation of the water saturation distribution along the through-plane direction under hydrophilic conditions

type	π/2 ± 0°		π/2 ± 5°	
sample	$S_{w,avg}$	*deviation*	$S_{w,avg}$	*deviation*
#1	0.19454	0.3559	0.19214	0.3214
#2	0.19045	0.2795	0.18899	0.3470
#3	0.19408	0.3855	0.19343	0.4172
type	π/2 ± 15°		π/2 ± 25°	
sample	$S_{w,avg}$	*deviation*	$S_{w,avg}$	*deviation*
#1	0.19380	0.4071	0.19194	0.4674
#2	0.18972	0.4106	0.19352	0.3378
#3	0.19466	0.4093	0.19404	0.6064

Table 4.3. The standard deviation of the water saturation distribution along the through-plane direction under hydrophobic conditions

type	π/2 ± 0°		π/2 ± 5°	
sample	$S_{w,avg}$	*deviation*	$S_{w,avg}$	*deviation*
#1	0.16301	0.2168	0.16250	0.2712
#2	0.16428	0.5348	0.16397	0.3160
#3	0.16260	0.4190	0.16291	0.1866
type	π/2 ± 15°		π/2 ± 25°	
sample	$S_{w,avg}$	*deviation*	$S_{w,avg}$	*deviation*
#1	0.16576	0.1738	0.16604	0.1538
#2	0.16391	0.2774	0.16601	0.2399
#3	0.16646	0.1298	0.16482	0.2375

4.4.2.2 ETC with various initial mass fractions of water

In this part, we vary the initial mass fraction of the water component to investigate the effect of the absolute saturated water component. For comparison with the previous humidified condition, the water component is set to $0.9\rho_c$ and $1.1\rho_c$,

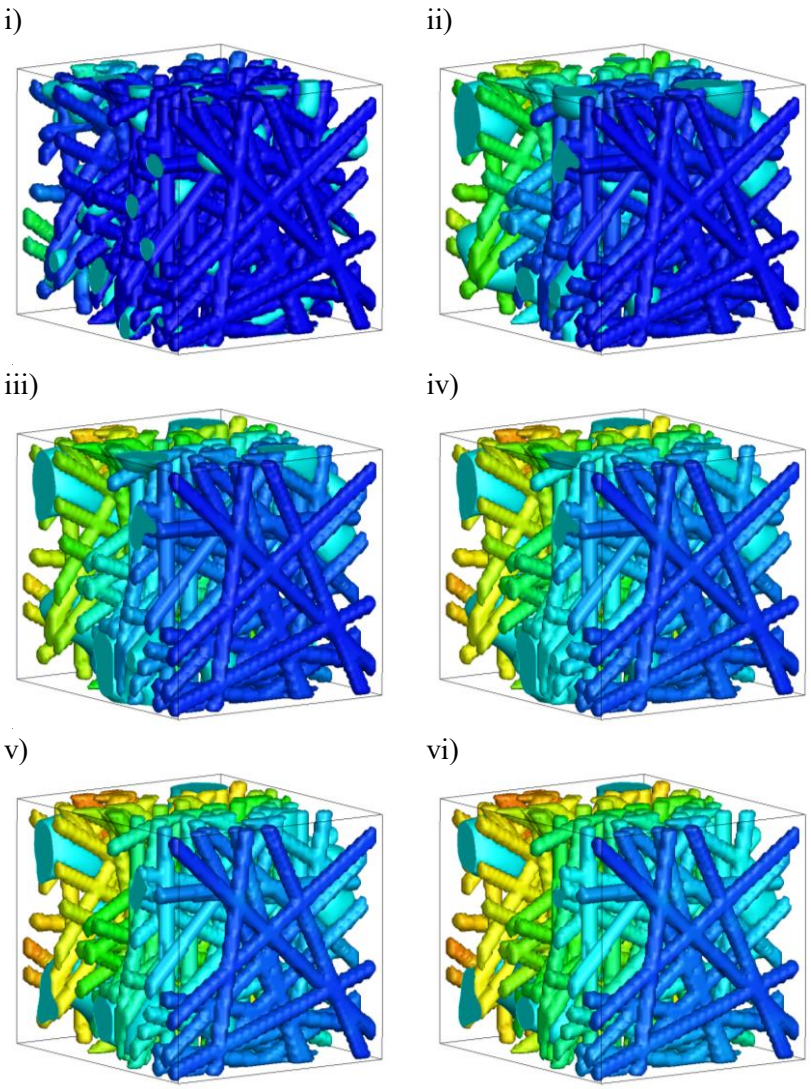

Fig.4.26. Time evolutions of the liquid water droplet and heat transfer through the GDL initialized $\rho_1 = 0.9\rho_c$ and $\theta_c = 80°$ ((i) 0.1×10^5 ts, (ii) 1×10^5 ts, (iii) 2×10^5 ts, (iv) 3×10^5 ts, (v) 4×10^5 ts, (vi) 5×10^5 ts)) (10^5 ts indicates 1.25 ms)

respectively, and the polar angle ranges are not considered. The initial and boundary conditions for temperature and air are the same as the previous conditions.

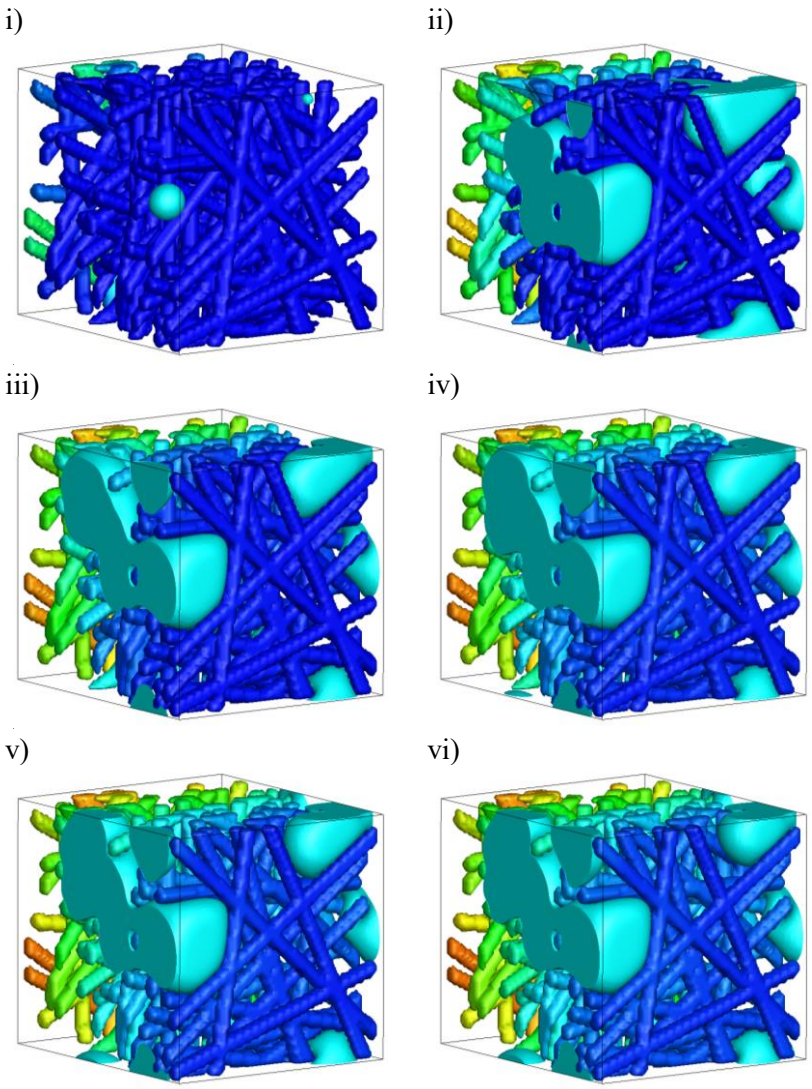

Fig.4.27. Time evolutions of the liquid water droplet and heat transfer through the GDL initialized $\rho_1 = 0.9\rho_c$ and $\theta_c = 140°$ ((i) 0.1×10^5 ts, (ii) 1×10^5 ts, (iii) 2×10^5 ts, (iv) 3×10^5 ts, (v) 4×10^5 ts, (vi) 5×10^5 ts)) (10^5 ts indicates 1.25 ms)

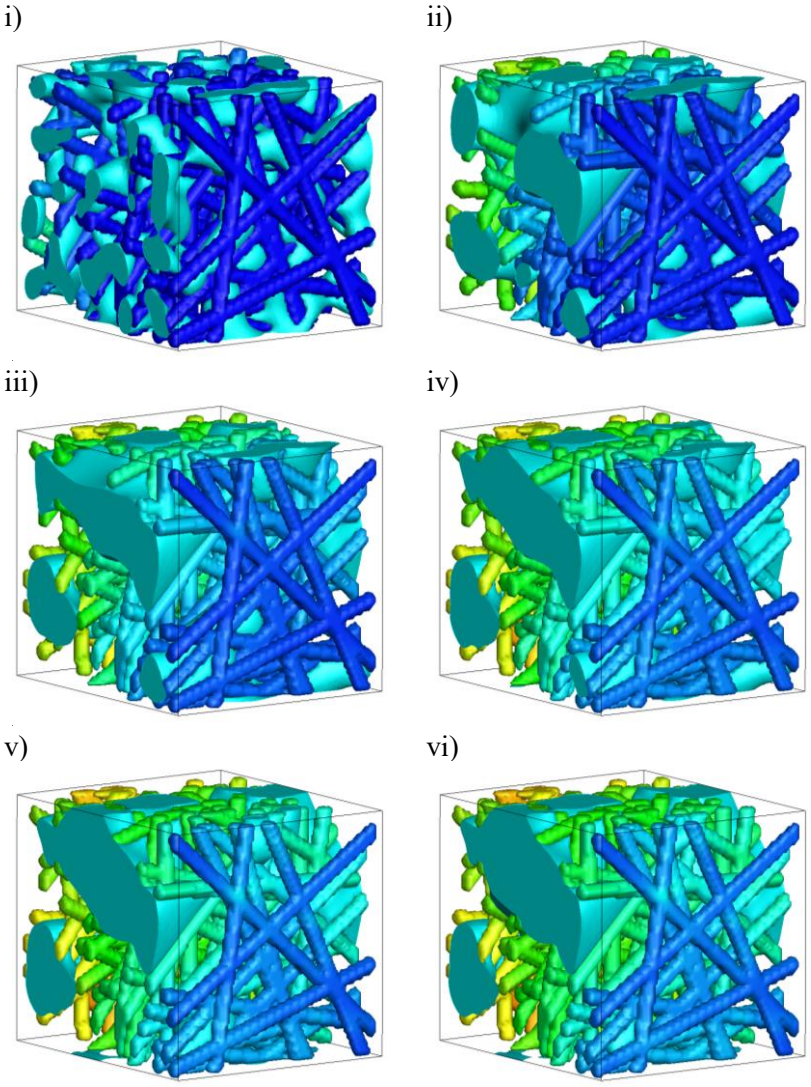

Fig.4.28. Time evolutions of the liquid water droplet and heat transfer through the GDL initialized $\rho_1 = 1.1\rho_c$ and $\theta_c = 80°$ ((i) 0.1×10^5 ts, (ii) 1×10^5 ts, (iii) 2×10^5 ts, (iv) 3×10^5 ts, (v) 4×10^5 ts, (vi) 5×10^5 ts)) (10^5 ts indicates 1.25 ms)

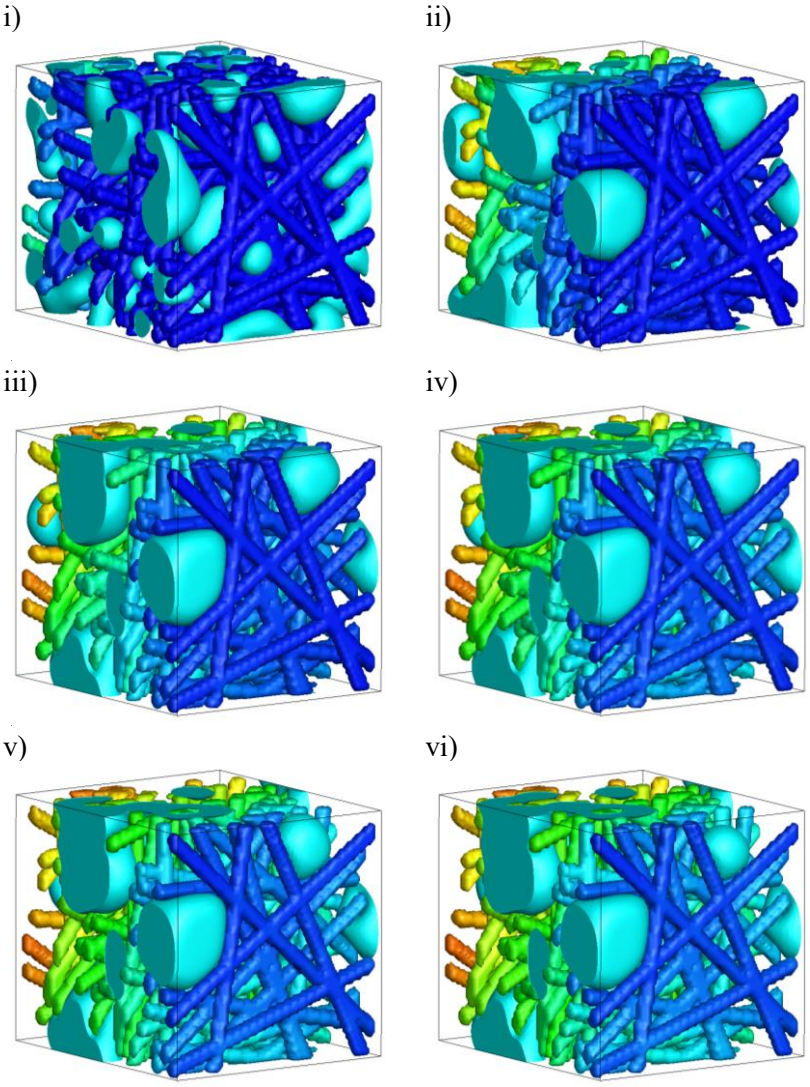

Fig.4.29. Time evolutions of the liquid water droplet and heat transfer through the GDL initialized $\rho_1 = 1.1\rho_c$ and $\theta_c = 140°$ ((i) 0.1×10^5 ts, (ii) 1×10^5 ts, (iii) 2×10^5 ts, (iv) 3×10^5 ts, (v) 4×10^5 ts, (vi) 5×10^5 ts)) (10^5 ts indicates 1.25 ms)

Figs. 4.26 – 4.29 show the temporal temperature and saturated water distribution of GDLs with different carbon fiber's wettability and initial water densities. The heat transfer process and phase separation of the water component are similar to the previous results, except for the location of initially aggregated liquid water droplets.

i) $0.9\rho_c$

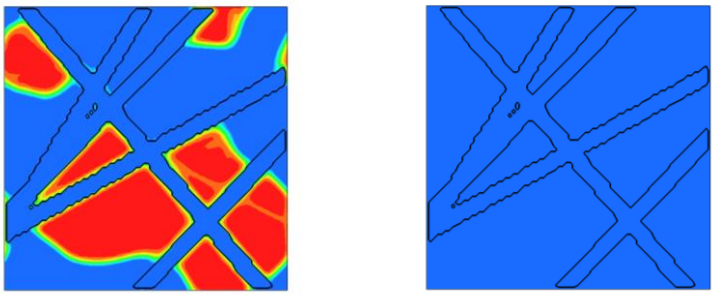

ii) $1.0\rho_c$

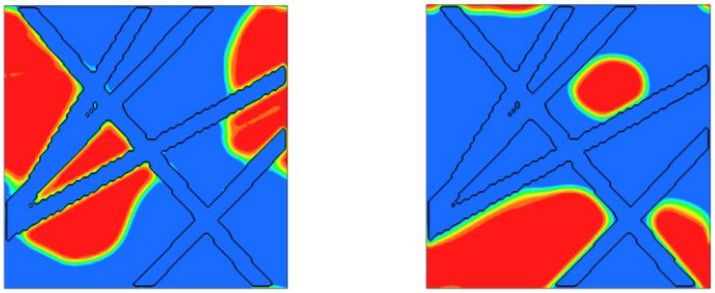

iii) $1.1\rho_c$

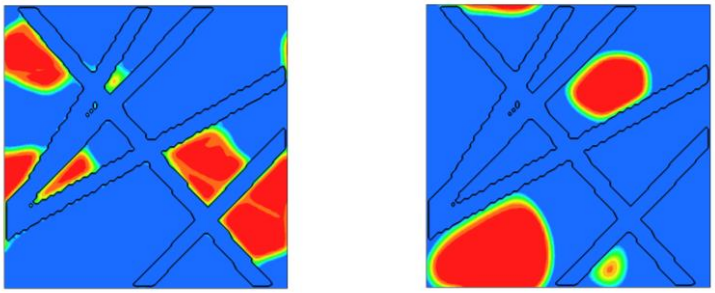

(a) (b)

Fig.4.30. Liquid water distribution in a cross-section of the through-plane in the GDL at 5×10^5 ts (10^5 ts indicates 1.25 ms), (a) hydrophilic, (b) hydrophobic

A significant difference from the previous results is that as the initial mass fraction of the water component increases, the water saturation also increases. In addition, the water component aggregates in certain areas at a low initial mass fraction condition. (Fig. 4.30). Due to the low saturation level, the droplet that plays the binder between fibers decreases, and less heat spreads through the GDL thickness direction simultaneously (Fig. 4.31).

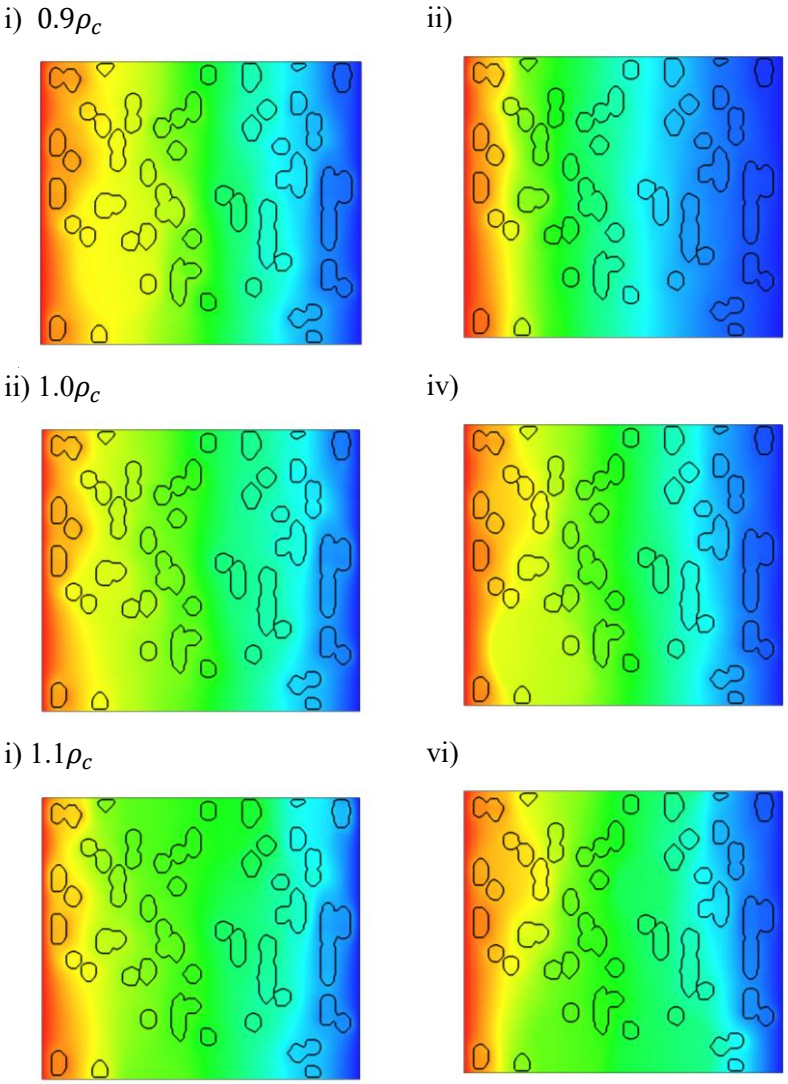

Fig.4.31. Temperature distribution of a cross-section of the in-plane in the GDL at 5×10^5 ts (10^5 ts indicates 1.25 ms), (a) hydrophilic, (b) hydrophobic

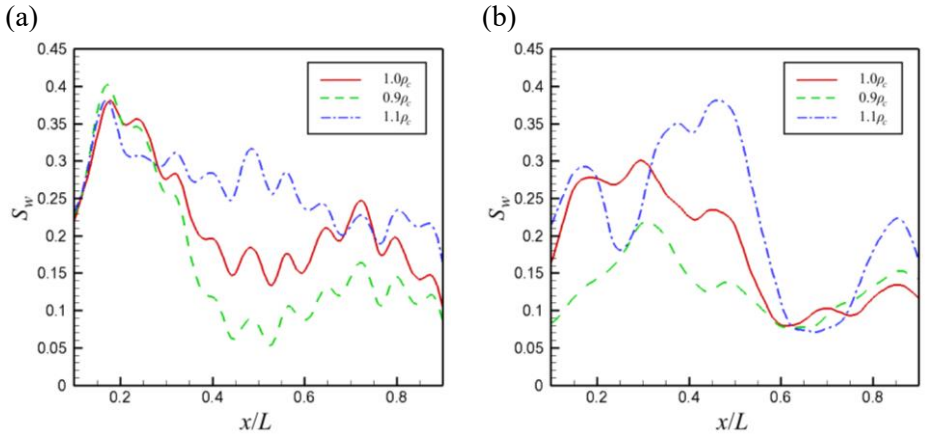

Fig.4.32. Averaged water saturation distribution along the through-plane direction with different initial water densities, (a) hydrophilic, (b) hydrophobic

Fig. 4.32 represents the averaged water distribution in the GDL thickness direction. As in the previous results, the water distribution is averaged by all three samples at each initial water density. Under hydrophilic conditions, the liquid water distributes more uniformly at the high initial mass fraction with a high water saturation level. In contrast, the liquid water spreads more evenly at the lowest initial density having a low average saturation level under hydrophobic conditions. It indicates that the morphological condition of hydrophilic GDL influences the water distribution at a

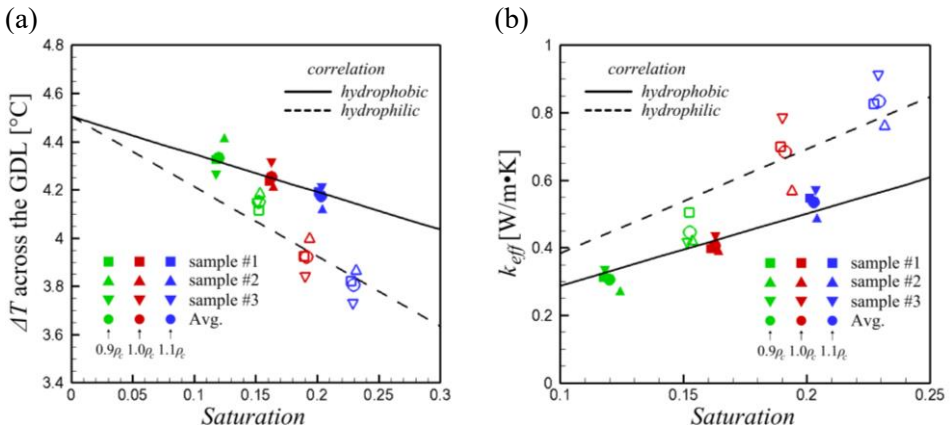

Fig.4.33. (a) Temperature difference across the GDL thickness, (b) predicted ETC as a function of saturation for various initial water densities

low saturation level in the same way as the previous results.

The measured temperature difference and predicted ETC for various initial water densities are presented in Fig. 4.33. The line in each figure represents the correlation as a function of saturation for the average value based on dry conditions. For the identical GDL structure, the predicted ETC increases at high absolute saturation, exhibiting a lower temperature difference along the GDL thickness. As saturation increases, more pores fill with liquid water, and carbon fibers are covered and connected by the liquid droplets. As a result, the heat conduction pathways are created more, and heat transfers more straightforwardly through the path from the catalyst layer to the gas channel. Furthermore, the correlation is more accurate for the hydrophobic condition. It means that the ETC of the hydrophobic GDL is more predictable and controllable than that of hydrophilic GDL.

4.5 Summary

In this chapter, the effective thermal conductivity (ETC) of the gas diffusion layer (GDL) was measured by the lattice Boltzmann method (LBM), and the effect of fiber orientation and water content on its thermal conductivity was investigated. The thermal LBM was coupled with the Peng-Robinson equation of state to consider the water content in the multicomponent. The effect of fiber allocation was performed on dry GDL, and a wide range of polar angles was adopted ($\varphi = \pi/2 \pm 0°, \pm 5°, \pm 15°$, and $\pm 25°$). We applied a one-dimensional initial temperature gradient to make a heat flux in the GDL. It was assumed that there is no additional heat source in other directions, and the simulated condition was low operation temperature, $T_{hot} = 335$ K.

The effect of the water content was obtained by assuming that the specific liquid water is saturated, and the temperature distribution was measured during the segregation and aggregation of the water component. In the LBM, it is conserved that the mass is released by condensation as much as the mass consumed by evaporation, so the latent heat corresponding to the phase change was neglected and considered a

very low current density. We also applied the uniform wettability of the carbon fibers (θ_c = 80° and 140°) to consider the influence of liquid water distribution on the ETC of GDL.

The results show that the ETC of GDLs increases as the fibers are arranged along the through-plane direction. The more the fibers are aligned with the through-plane direction, the easier the heat generated from the catalyst layer is transferred through the fibers. In addition, the expected values using LBM very well represent the thermal properties of the GDL obtained based on the experimental results. Furthermore, the water content significantly influences thermal conduction in the GDL. In hydrophilicity, the liquid water is spread between fibers and acts as a binder, resulting in a high water saturation level. Since the thermal conductivity of the liquid is much higher than that of air, it shows a higher ETC in hydrophobic and hydrophilic cases compared to dry conditions.

The water distribution also affects the ETC of GDL, and the morphological state of GDL influences it. The ETC increases as the fibers are hydrophobic and have a wide polar range, showing a more uniform water distribution. On the other hand, in the case of hydrophilicity, liquid water is distributed in a specific layer with relatively large pores, and more outstanding heat transfer occurs. This indicates that the pore structure significantly influences the heat and water transfer of hydrophilic GDLs.

In terms of the mass fraction of the water component, the water saturation increases under the high mass fraction. It represents that the high relative humidity in the GDL affects the predicted ETC. The path for heat conduction in the GDL is made more as more liquid water occupies and covers the pores and carbon fiber. Furthermore, the ETC of the hydrophobic GDL shows a more accurate correlation and expectation with water saturation. Therefore, the results suggest that obtaining the hydrophobic wettability by coating the PTFE in an uncompressed region would help maintain the pore for the flow of reaction gases and improve thermal management in various humidity conditions.

CHAPTER 5
CONCLUSIONS

5.1 Conclusions

In this dissertation, numerical studies on heat and mass transport characteristics in the GDL of PEMFC are carried out using the multicomponent multiphase (MCMP) lattice Boltzmann method (LBM). A summary of each chapter follows.

In Chapter 2, the fundamental theories of the MCMP LBM and thermal LBM were introduced, and two different forcing schemes were proposed to investigate the interaction force between the multicomponent and solid wall. The first proposed model was the Shan-Chen (SC) model. It is appropriate to investigate immiscible two-component flows with negligible density and viscosity ratios with very low capillary flows, and this model was used in Chapter 3. The second one was the exact difference method (EDM) model. It was combined with the thermal LBM model to consider the high-density ratio between components and phase change source term dependence on temperature. The EDM model was improved to approximate the physical density ratio of liquid water and air by applying the Peng-Robinson equation of state for a non-ideal gas. However, it did not include the latent heat due to phase change in the thermal analysis but considered the phase separation of the water component at various temperature ranges. The comprehensive analysis of phase separation and heat transfer using the EDM model was applied in Chapter 4.

In Chapter 3, the stochastic reconstruction method was used to generate the 3D GDL microstructure. The forcing terms in the SC model and regenerated GDL were verified by comparing them with theoretical analysis and experimental results. The effect of carbon fiber orientation on liquid water transport in GDL was conducted using the SC model, and various polar angle ranges were applied. The observed water invasion patterns showed the "capillary fingering" flow to corresponding the small capillary number, $Ca \sim 10^{-5} – 10^{-8}$. Contrary to expectations, the preferential pathway for liquid water breakthrough in GDL did not differ significantly depending on the

applied polar angle ranges. The results revealed that liquid water transport in the GDL is still critically influenced by the pressure drop through the GDL thickness direction. Furthermore, the averaged water saturations in all cases were also represented at a similar level. However, as the applied polar angle range was broadened, the interface between the GC and GDL was more occupied by liquid water as growing the liquid droplet. As a result, the apparent angle was affected, and the lowest was measured in the case with the polar range was $\varphi = \pi/2 \pm 15°$.

In Chapter 4, an advanced 3D MCMP model coupled with thermal LBM was developed to include the phase change depending on the temperature and high-density ratio between each component. The EDM model was suitable to include additional interaction forces that indicate phase separation of non-ideal components. Although the phase separation in MCMP was not the ultimate objective of the proposed model in this dissertation, the proposed model well presented the phase segregation in the unstable region according to Maxwell's construction and could simulate the density ratio between multicomponent, up to 764.21 at $T_r = 0.51$. However, considering the phase change with an appropriate physical density ratio remains challenging.

The effective thermal conductivity (ETC) of the GDL was investigated to determine the effect of fiber orientation and water content on its thermal conductivity. Two different simulation scenarios were applied as dry and humidified conditions. The three-phase conductive heat transfer of solid-liquid-gas in multicomponent was particularly well described in the second scenario. In all conditions, the volume-averaged temperature difference of the GDL was 2.44 ℃ in dry conditions and 2.33 ℃ to 2.54 ℃ in humidified conditions, and there was no significant difference according to the applied fiber orientation. The saturation pressure corresponding to the temperature difference was also negligible, about $3.46 - 3.95$ kPa. However, the predicted ETC of GDL varied and increased when the fibers were more parallel to the heat flux direction under the dry condition.

On the other hand, humidified GDL was more affected by the saturated liquid water than the morphological conditions. Up to 35.28 % and 48.67 % higher ETC was

predicted under the same wettability of GDL as more liquid water uniformly adhered between the fibers as the binder. Furthermore, the pore structure significantly influenced the heat and water transfer of hydrophilic GDLs. The ETC of the hydrophobic GDLs is also more predictable under the various water saturation level than that of the hydrophilic GDLs. Thus, coating the GDL with a hydrophobic material such as PTFE was more proper to maintain the pore for the flow of reaction gases and improve the efficiency of thermal control in various humidity conditions.

5.2 Future Works

Using the stochastic reconstruction method and the SC model, 3D microstructure with various polar ranges were applied to investigate the water transportation characteristics in anisotropic GDL. It was identified that the invasion pattern in GDL was still significantly affected by the capillary pressure in the through-plane direction corresponding to the mean pore size formed in the through-plane. If the mean pore size distributed in GDL is enough to break through and make a preferential path for liquid water, the fiber orientation in the in-planes is not crucial to removing liquid water through the GDL.

Future research should focus not only on the parameters determining the mean pore size distribution in the through-plane, such as the fiber diameter and number with a stochastic model, but also on the non-uniform wettability of GDL and pressure difference along the GDL thickness. Furthermore, the gas flow considering the rib structure should also be considered as future work. The apparent angle formed after breaking through the GDL in GC significantly depended on the surface's fiber orientation. The results could not be confirmed in the conventional 2D geometry. Thus, the azimuthal angle of carbon fiber in the GDL surface layer should also be considered with gas flow direction in the GC using the 3D stochastic reconstruction method.

In addition, it was identified that the ETC of GDL was much more affected by saturated water distribution in GDL using the thermal coupled MCMP model. However, the proposed EDM model with thermal LBM was used in many restrictions

and assumptions to investigate the influence of the water component on the heat transfer of GDL. Thus, future research should develop the proposed model to include the neglected terms (velocity and phase change source) and conduct the condensation/evaporation in various relative humidity by initializing the density of the water component differently. Furthermore, by applying the multi-boundary conditions to each direction (i.e., in-plane for the gas component, through-plane for the liquid component), the effect of the convective heat transfer by cooling gas flow in the in-plane direction can be applied using the developed model in this dissertation.

Finally, the proposed model in this dissertation provides a framework that provides comprehensive understanding by simultaneous analysis of thermal and phase segregation in multicomponent. The results could not be done ever in the existing MCMP LBM model. The results presented in this dissertation can be used as a guideline in manufacturing the GDL of PEMFC.

APPENDIX

A. The Time evolutions of the liquid water droplet and heat transfer through the various GDLs

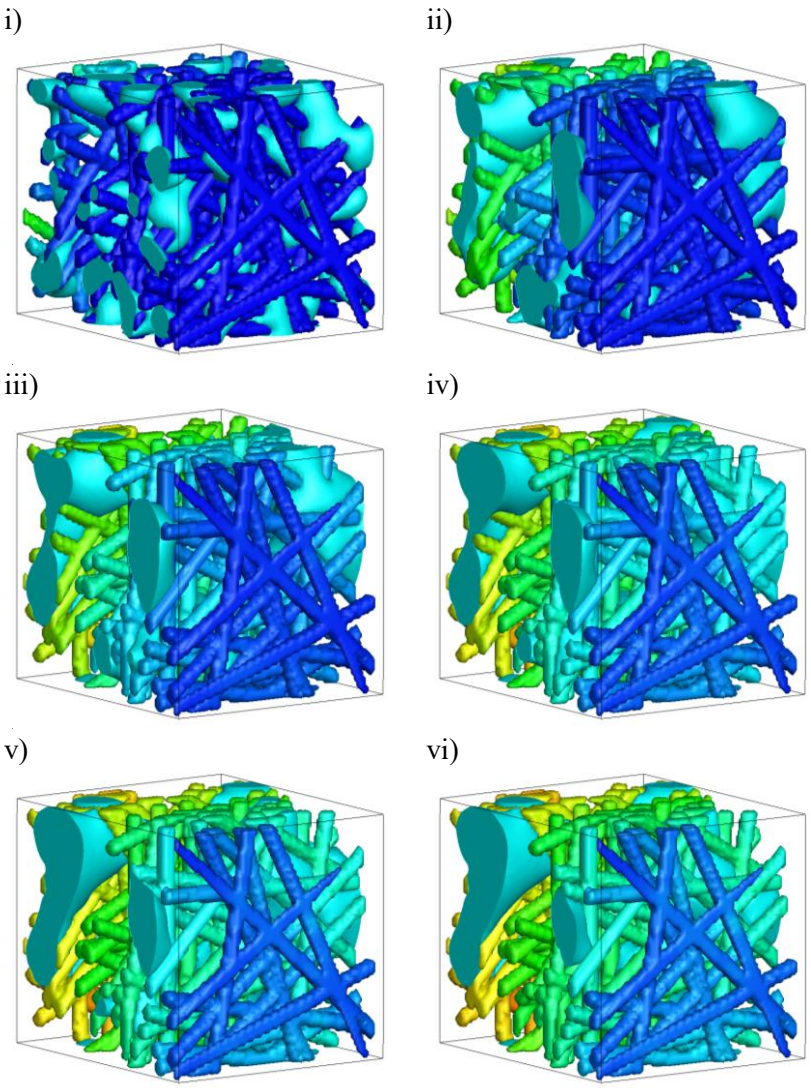

Fig.A1. Time evolutions of the liquid water droplet and heat transfer through the GDL having $\varphi = \pi/2 \pm 5°$ and $\theta_c = 80°$ ((i) 0.1×10^5 ts, (ii) 1×10^5 ts, (iii) 2×10^5 ts, (iv) 3×10^5 ts, (v) 4×10^5 ts, (vi) 5×10^5 ts)) (10^5 ts indicates 1.25 ms)

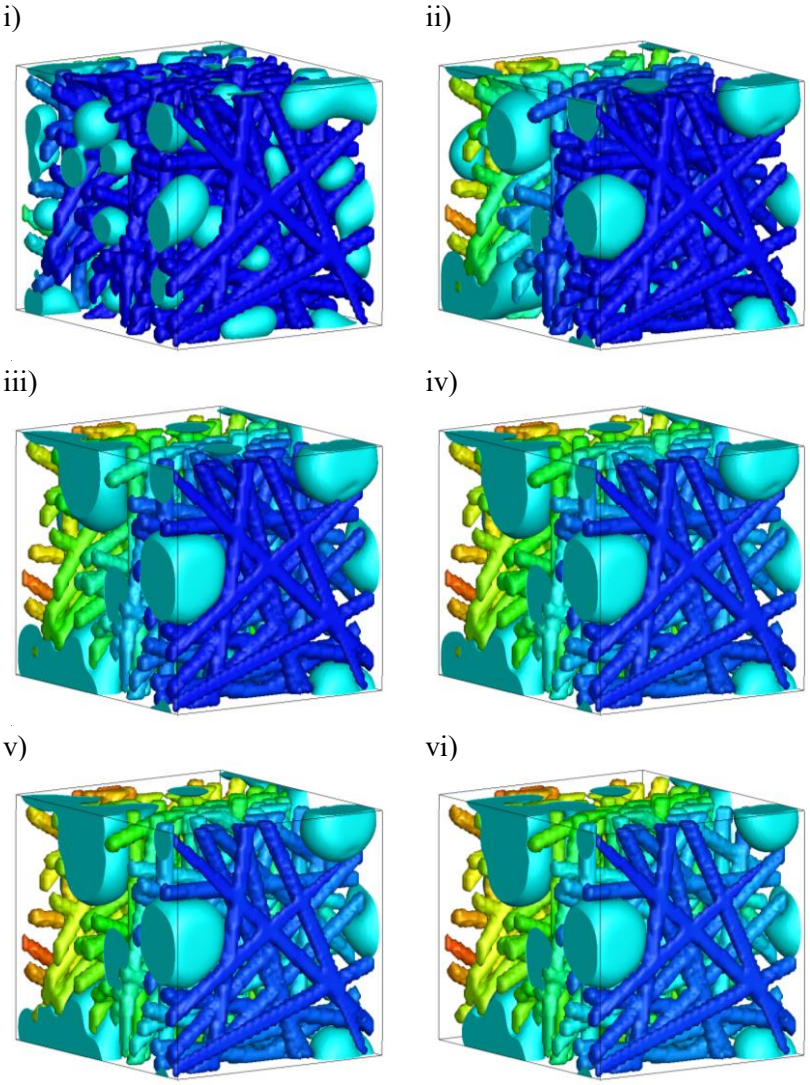

Fig.A2. Time evolutions of the liquid water droplet and heat transfer through the GDL having $\varphi = \pi/2 \pm 5°$ and $\theta_c = 140°$ ((i) 0.1×10^5 ts, (ii) 1×10^5 ts, (iii) 2×10^5 ts, (iv) 3×10^5 ts, (v) 4×10^5 ts, (vi) 5×10^5 ts)) (10^5 ts indicates 1.25 ms)

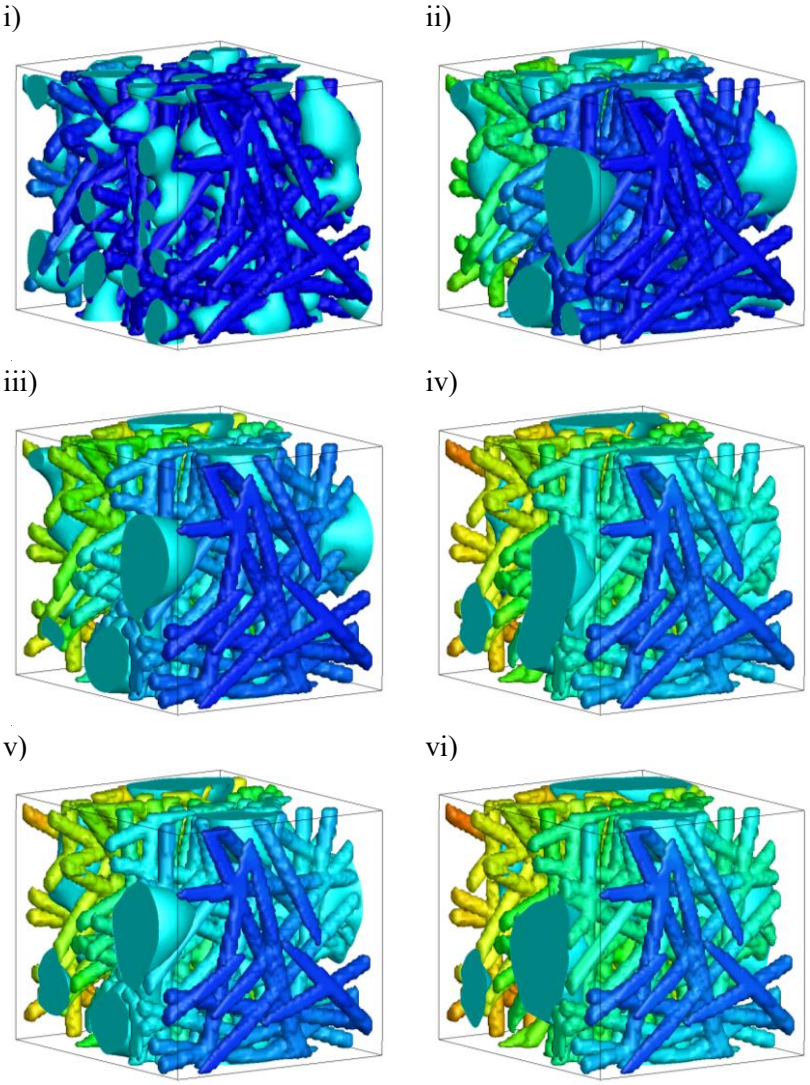

Fig.A3. Time evolutions of the liquid water droplet and heat transfer through the GDL having $\varphi = \pi/2 \pm 15°$ and $\theta_c = 80°$ ((i) 0.1×10^5 ts, (ii) 1×10^5 ts, (iii) 2×10^5 ts, (iv) 3×10^5 ts, (v) 4×10^5 ts, (vi) 5×10^5 ts)) (10^5 ts indicates 1.25 ms)

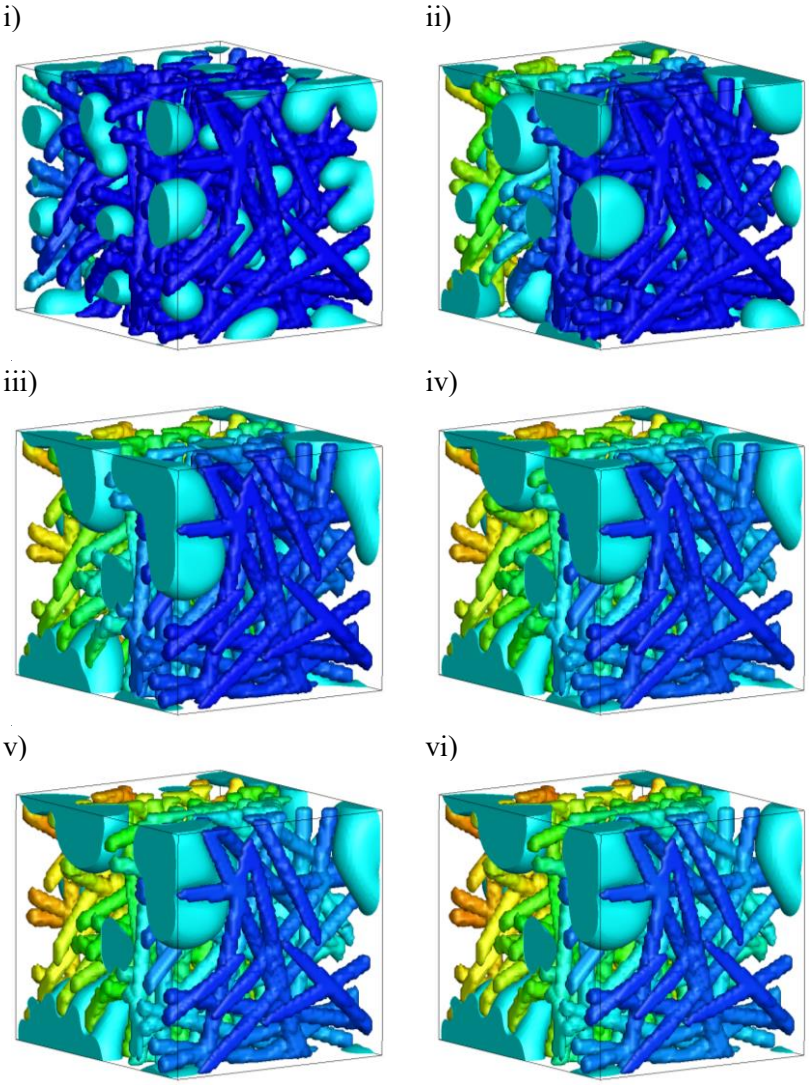

Fig.A4. Time evolutions of the liquid water droplet and heat transfer through the GDL having $\varphi = \pi/2 \pm 15°$ and $\theta_c = 140°$ ((i) 0.1×10^5 ts, (ii) 1×10^5 ts, (iii) 2×10^5 ts, (iv) 3×10^5 ts, (v) 4×10^5 ts, (vi) 5×10^5 ts)) (10^5 ts indicates 1.25 ms)

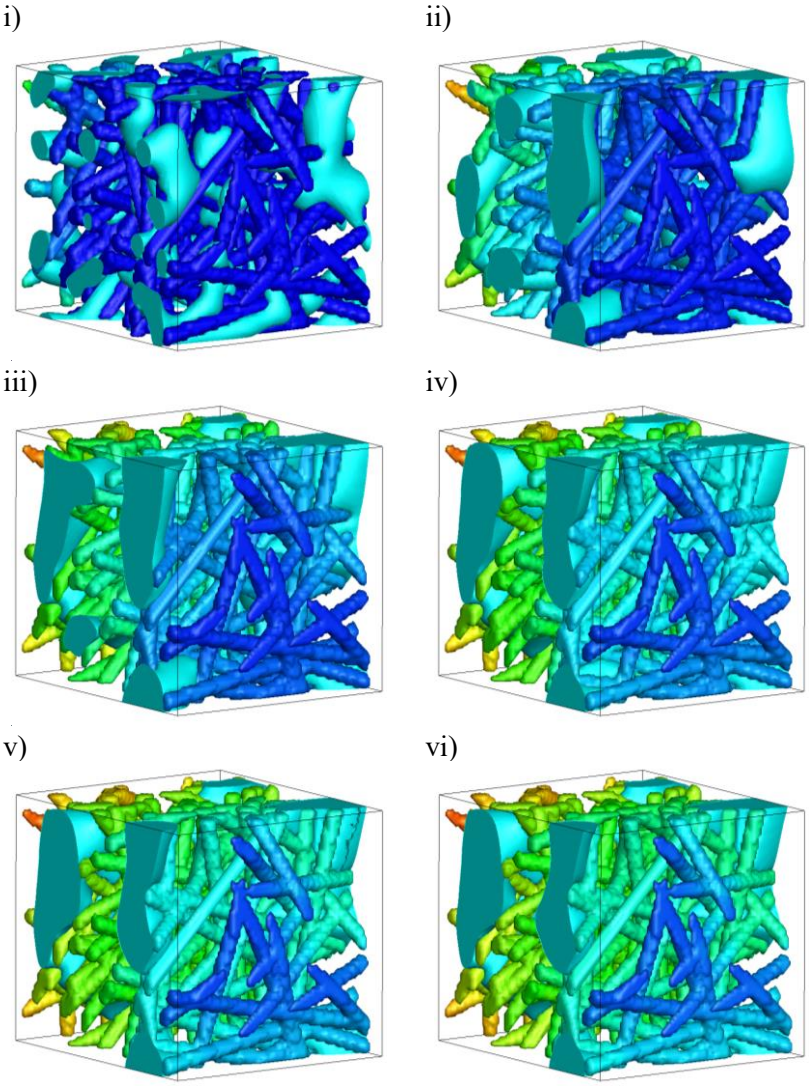

Fig.A5. Time evolutions of the liquid water droplet and heat transfer through the GDL having $\varphi = \pi/2 \pm 25°$ and $\theta_c = 80°$ ((i) 0.1×10^5 ts, (ii) 1×10^5 ts, (iii) 2×10^5 ts, (iv) 3×10^5 ts, (v) 4×10^5 ts, (vi) 5×10^5 ts)) (10^5 ts indicates 1.25 ms)

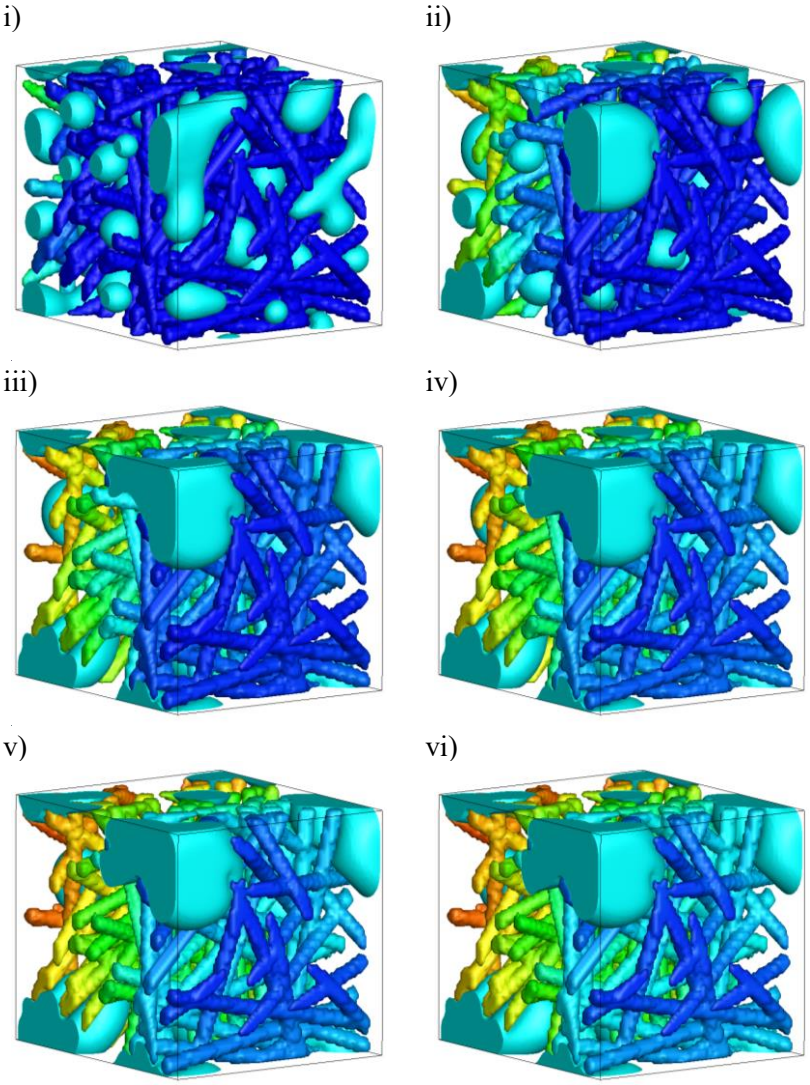

Fig.A6. Time evolutions of the liquid water droplet and heat transfer through the GDL having $\varphi = \pi/2 \pm 25°$ and $\theta_c = 140°$ ((i) 0.1×10^5 ts, (ii) 1×10^5 ts, (iii) 2×10^5 ts, (iv) 3×10^5 ts, (v) 4×10^5 ts, (vi) 5×10^5 ts)) (10^5 ts indicates 1.25 ms)

B. Liquid water distribution in a cross-section of the through-plane in the various GDLs

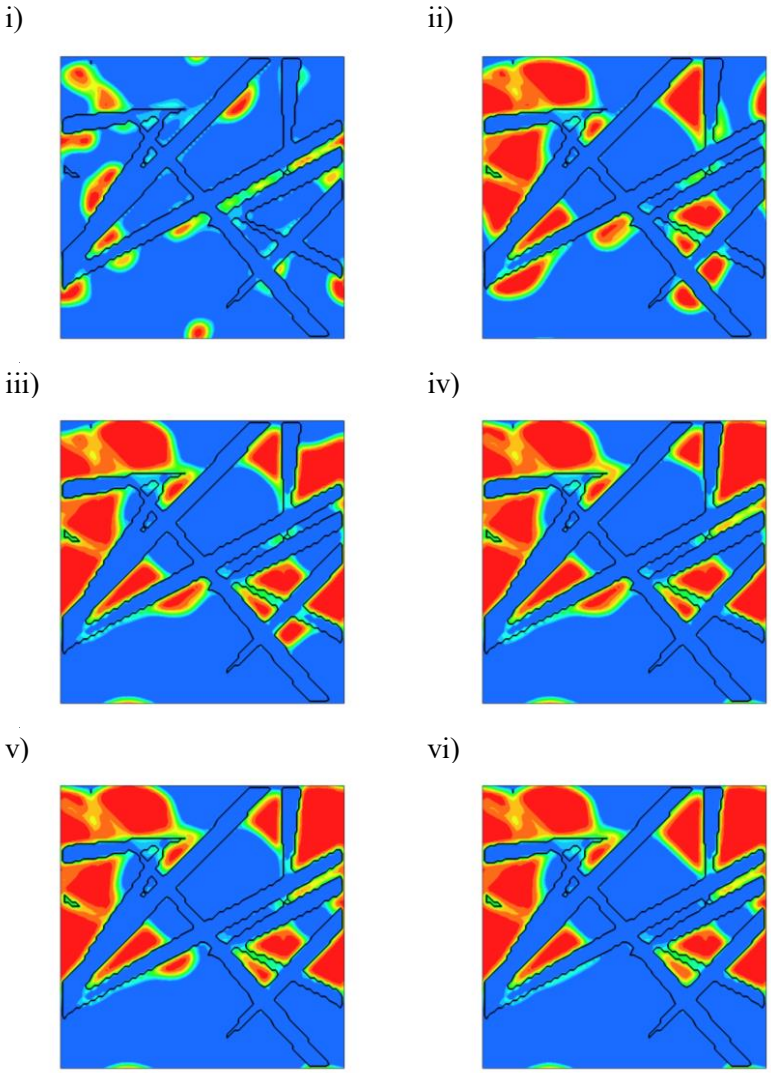

Fig.A7. Liquid water distribution in a cross-section of the through-plane in the GDL having $\varphi = \pi/2 \pm 5°$ and $\theta_c = 80°$ ((i) 0.1×10^5 ts, (ii) 1×10^5 ts, (iii) 2×10^5 ts, (iv) 3×10^5 ts, (v) 4×10^5 ts, (vi) 5×10^5 ts)) (10^5 ts indicates 1.25 ms)

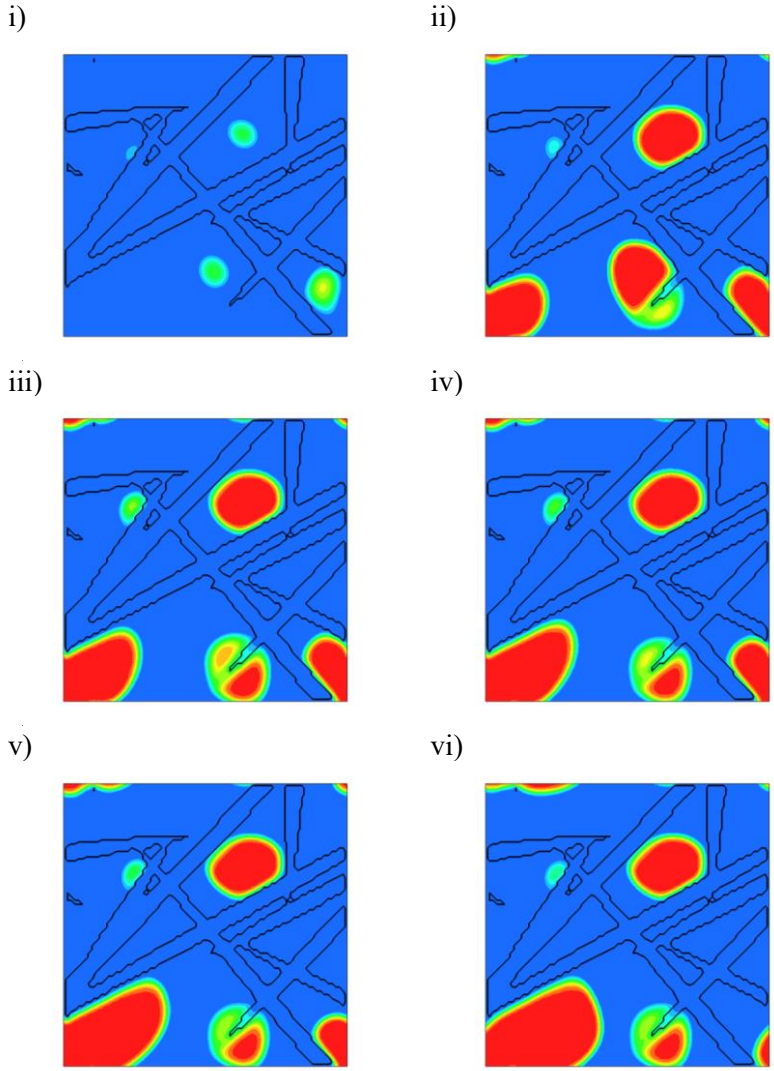

Fig.A8. Liquid water distribution in a cross-section of the through-plane in the GDL having $\varphi = \pi/2 \pm 5°$ and $\theta_c = 140°$ ((i) 0.1×10^5 ts, (ii) 1×10^5 ts, (iii) 2×10^5 ts, (iv) 3×10^5 ts, (v) 4×10^5 ts, (vi) 5×10^5 ts)) (10^5 ts indicates 1.25 ms)

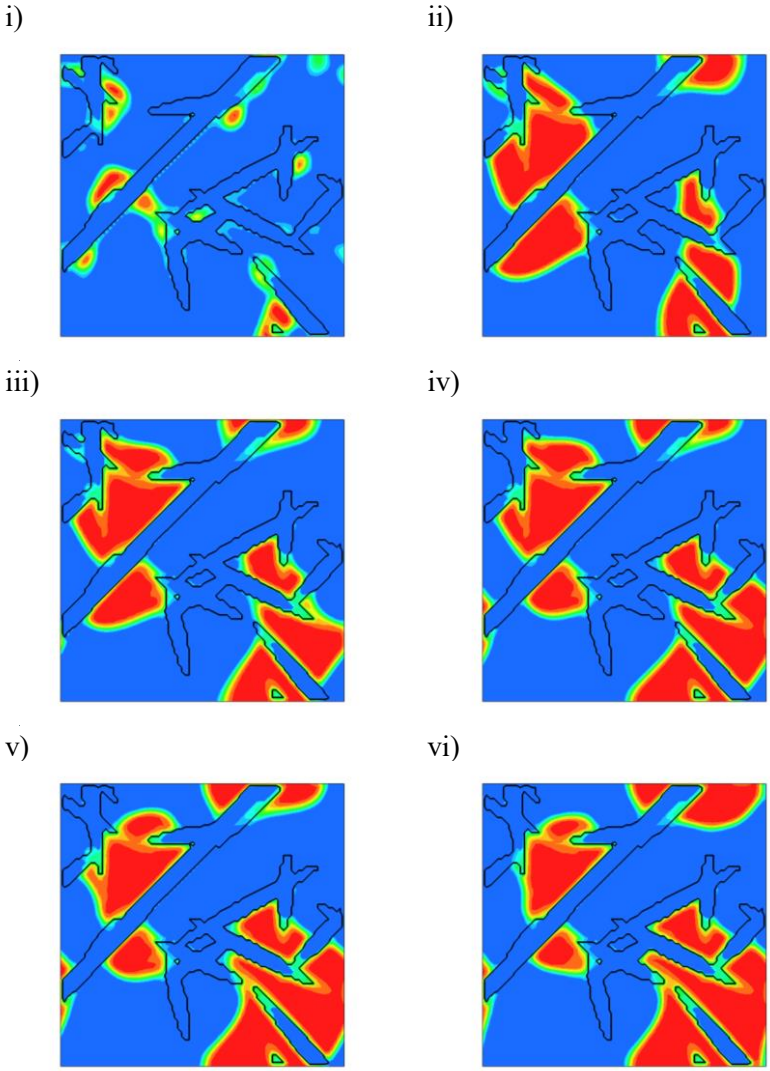

Fig.A9. Liquid water distribution in a cross-section of the through-plane in the GDL having $\varphi = \pi/2 \pm 15°$ and $\theta_c = 80°$ ((i) 0.1×10^5 ts, (ii) 1×10^5 ts, (iii) 2×10^5 ts, (iv) 3×10^5 ts, (v) 4×10^5 ts, (vi) 5×10^5 ts)) (10^5 ts indicates 1.25 ms)

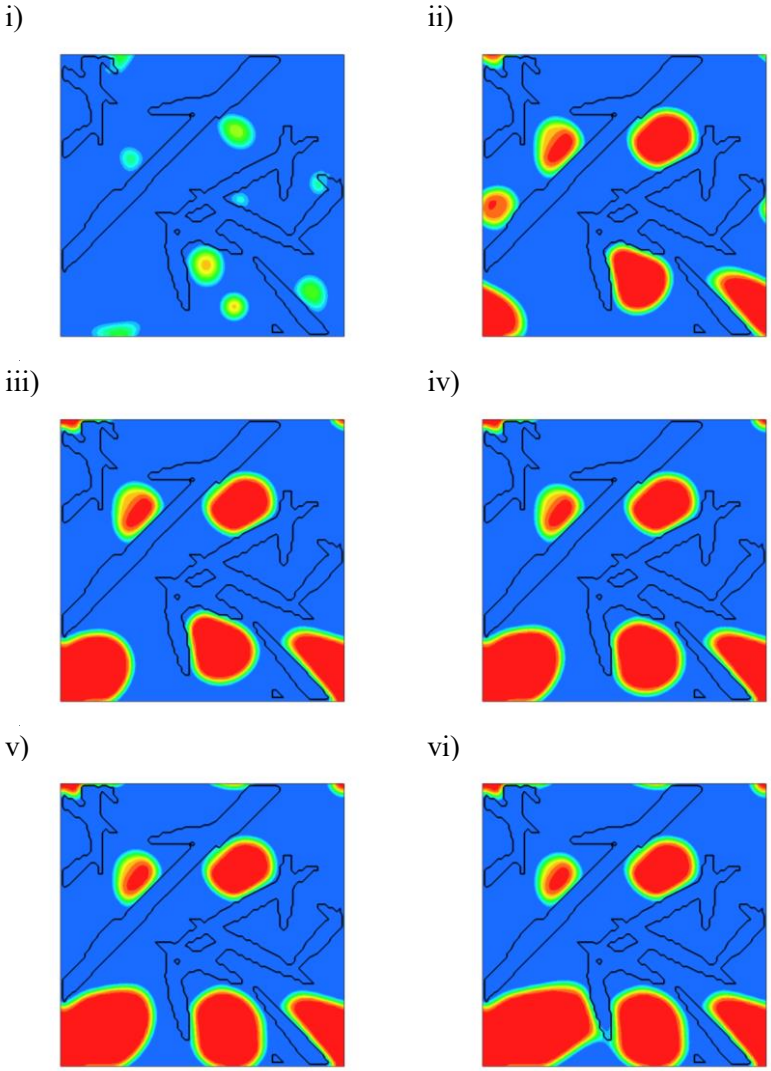

Fig.A10. Liquid water distribution in a cross-section of the through-plane in the GDL having $\varphi = \pi/2 \pm 15°$ and $\theta_c = 140°$ ((i) 0.1×10^5 ts, (ii) 1×10^5 ts, (iii) 2×10^5 ts, (iv) 3×10^5 ts, (v) 4×10^5 ts, (vi) 5×10^5 ts)) (10^5 ts indicates 1.25 ms)

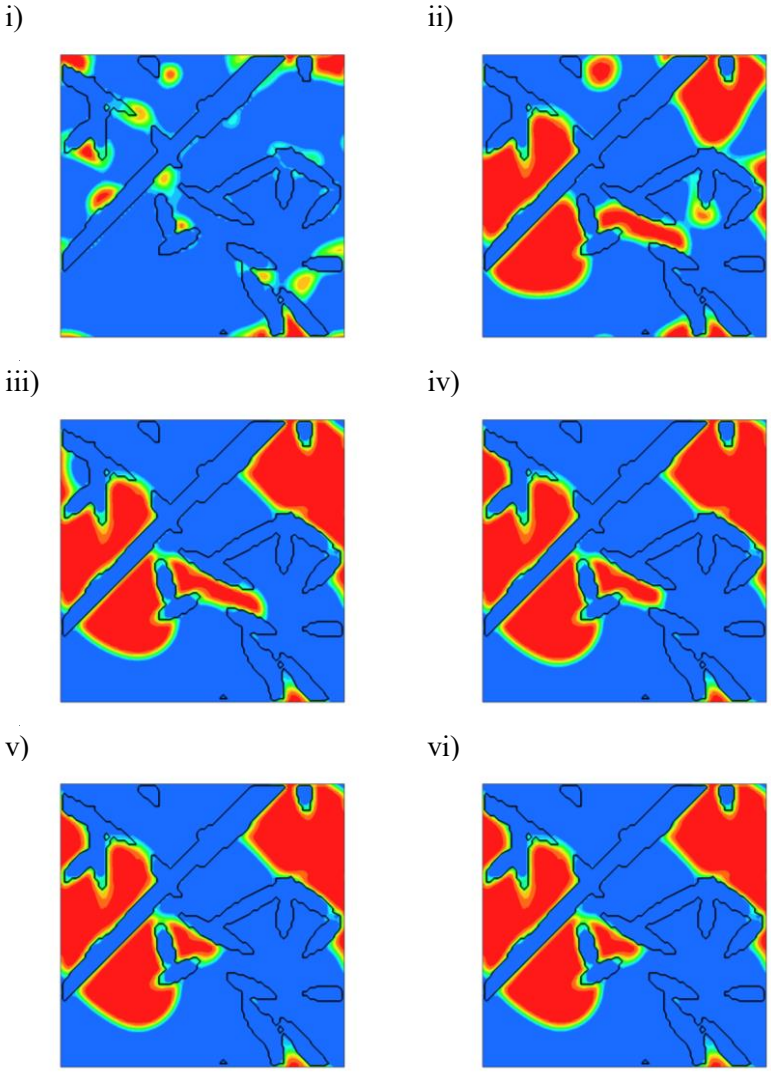

Fig.A11. Liquid water distribution in a cross-section of the through-plane in the GDL having $\varphi = \pi/2 \pm 25°$ and $\theta_c = 80°$ ((i) 0.1×10^5 ts, (ii) 1×10^5 ts, (iii) 2×10^5 ts, (iv) 3×10^5 ts, (v) 4×10^5 ts, (vi) 5×10^5 ts)) (10^5 ts indicates 1.25 ms)

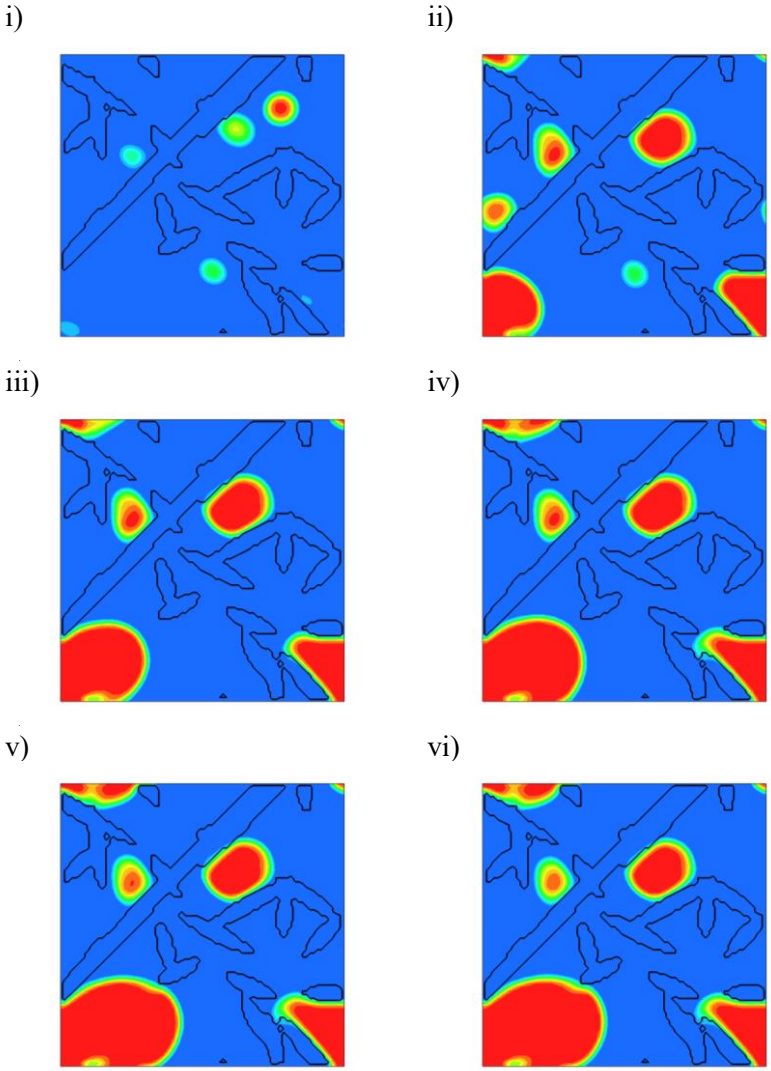

Fig.A12. Liquid water distribution in a cross-section of the through-plane in the GDL having $\varphi = \pi/2 \pm 25°$ and $\theta_c = 140°$ ((i) 0.1×10^5 ts, (ii) 1×10^5 ts, (iii) 2×10^5 ts, (iv) 3×10^5 ts, (v) 4×10^5 ts, (vi) 5×10^5 ts)) (10^5 ts indicates 1.25 ms)

C. Temperature distribution of cross-section of in-plane in the various GDLs

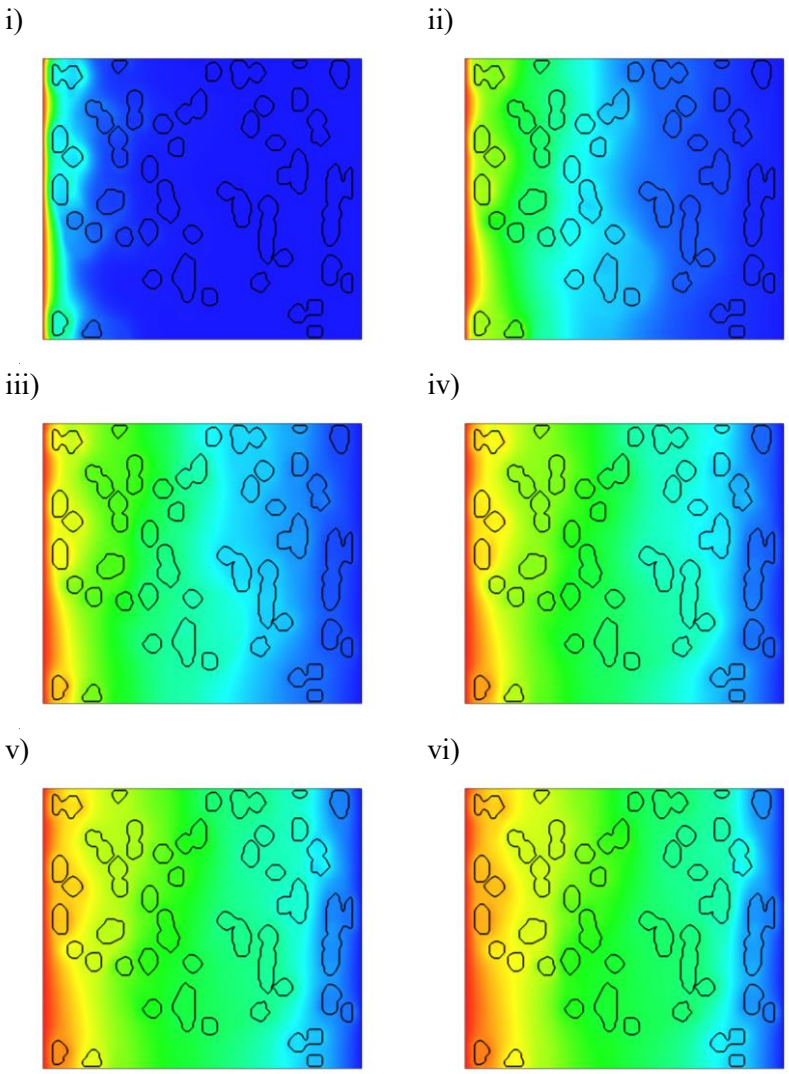

Fig.A13. Temperature distribution of a cross-section of the in-plane in the GDL having $\varphi = \pi/2 \pm 5°$ and $\theta_c = 80°$ ((i) 0.1×10^5 ts, (ii) 1×10^5 ts, (iii) 2×10^5 ts, (iv) 3×10^5 ts, (v) 4×10^5 ts, (vi) 5×10^5 ts)) (10^5 ts indicates 1.25 ms)

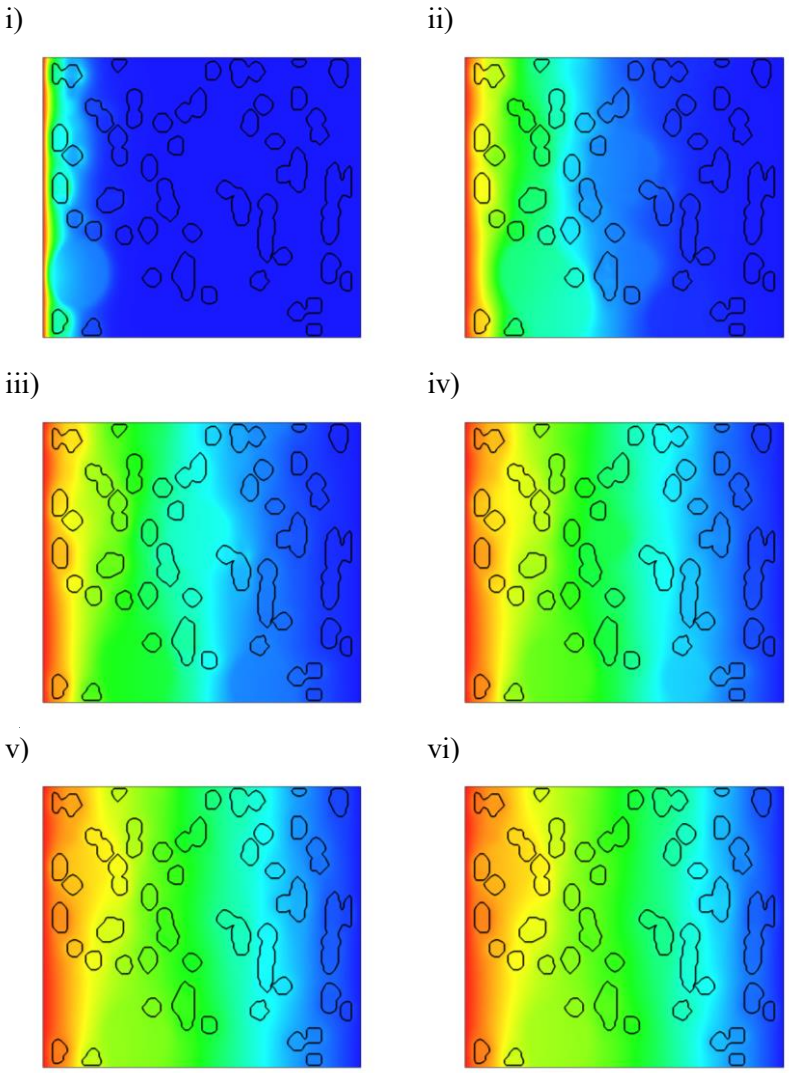

Fig.A14. Temperature distribution of a cross-section of the in-plane in the GDL having $\varphi = \pi/2 \pm 5°$ and $\theta_c = 140°$ ((i) 0.1×10^5 ts, (ii) 1×10^5 ts, (iii) 2×10^5 ts, (iv) 3×10^5 ts, (v) 4×10^5 ts, (vi) 5×10^5 ts)) (10^5 ts indicates 1.25 ms)

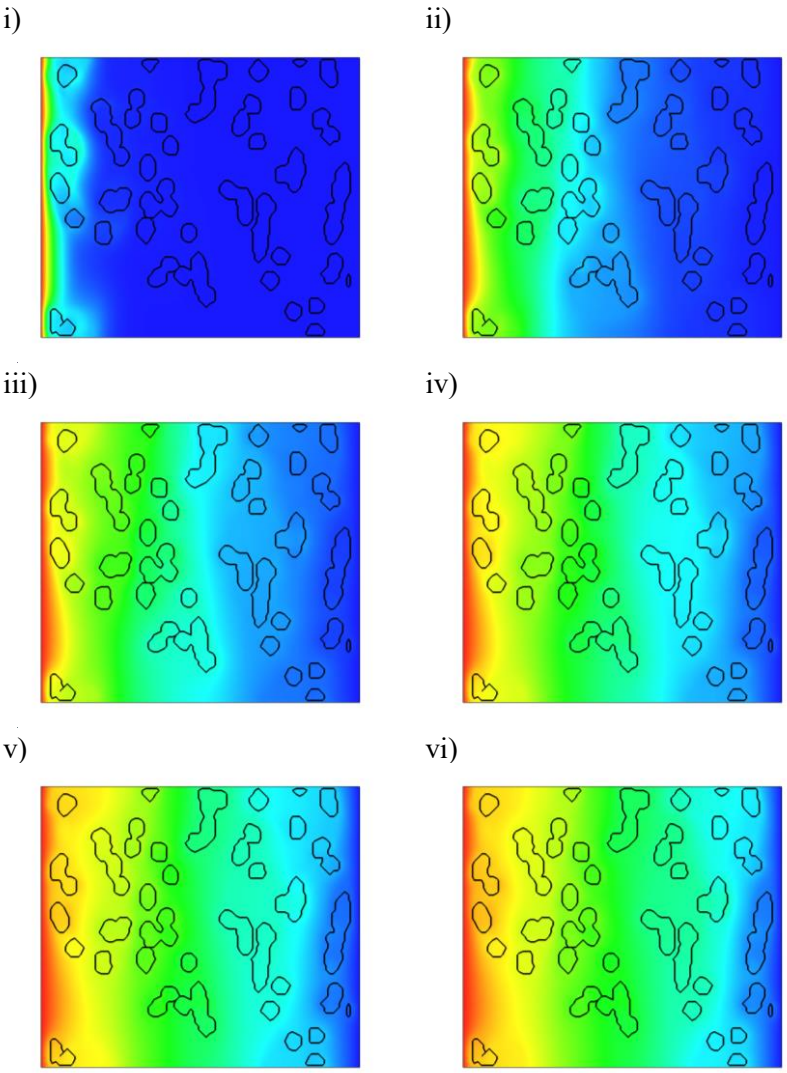

Fig.A15. Temperature distribution of a cross-section of the in-plane in the GDL having $\varphi = \pi/2 \pm 15°$ and $\theta_c = 80°$ ((i) 0.1×10^5 ts, (ii) 1×10^5 ts, (iii) 2×10^5 ts, (iv) 3×10^5 ts, (v) 4×10^5 ts, (vi) 5×10^5 ts)) (10^5 ts indicates 1.25 ms)

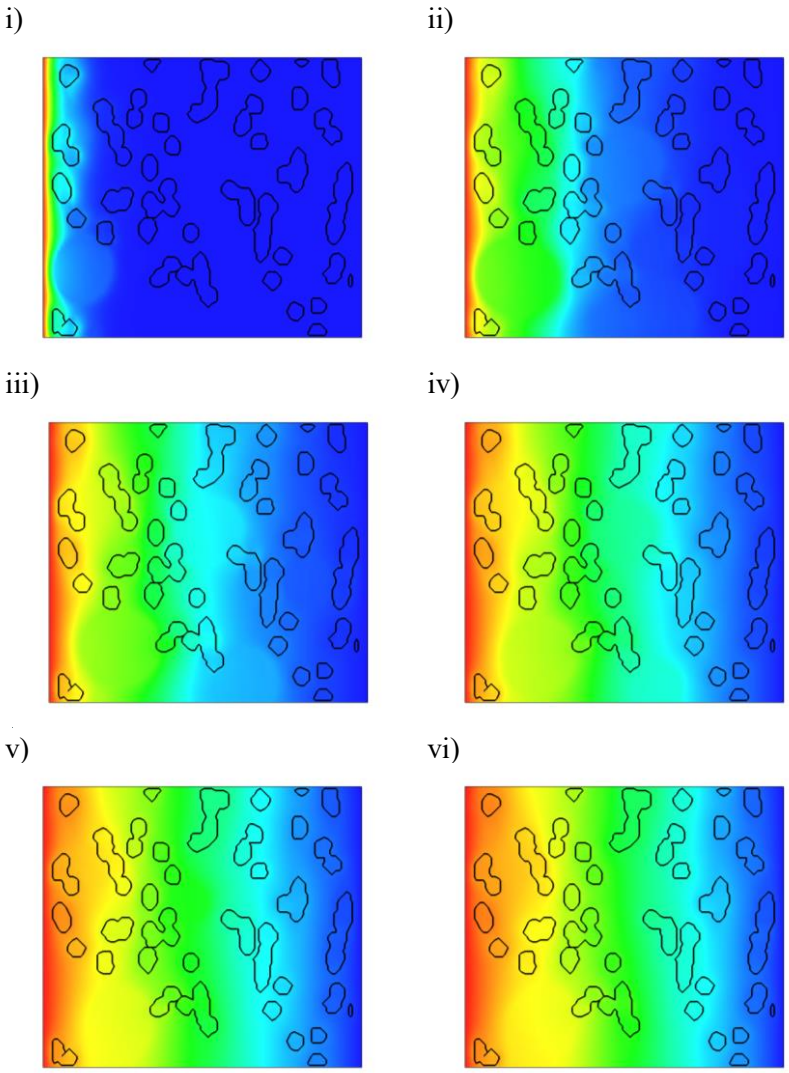

Fig.A16. Temperature distribution of a cross-section of the in-plane in the GDL having $\varphi = \pi/2 \pm 15°$ and $\theta_c = 140°$ ((i) 0.1×10^5 ts, (ii) 1×10^5 ts, (iii) 2×10^5 ts, (iv) 3×10^5 ts, (v) 4×10^5 ts, (vi) 5×10^5 ts)) (10^5 ts indicates 1.25 ms)

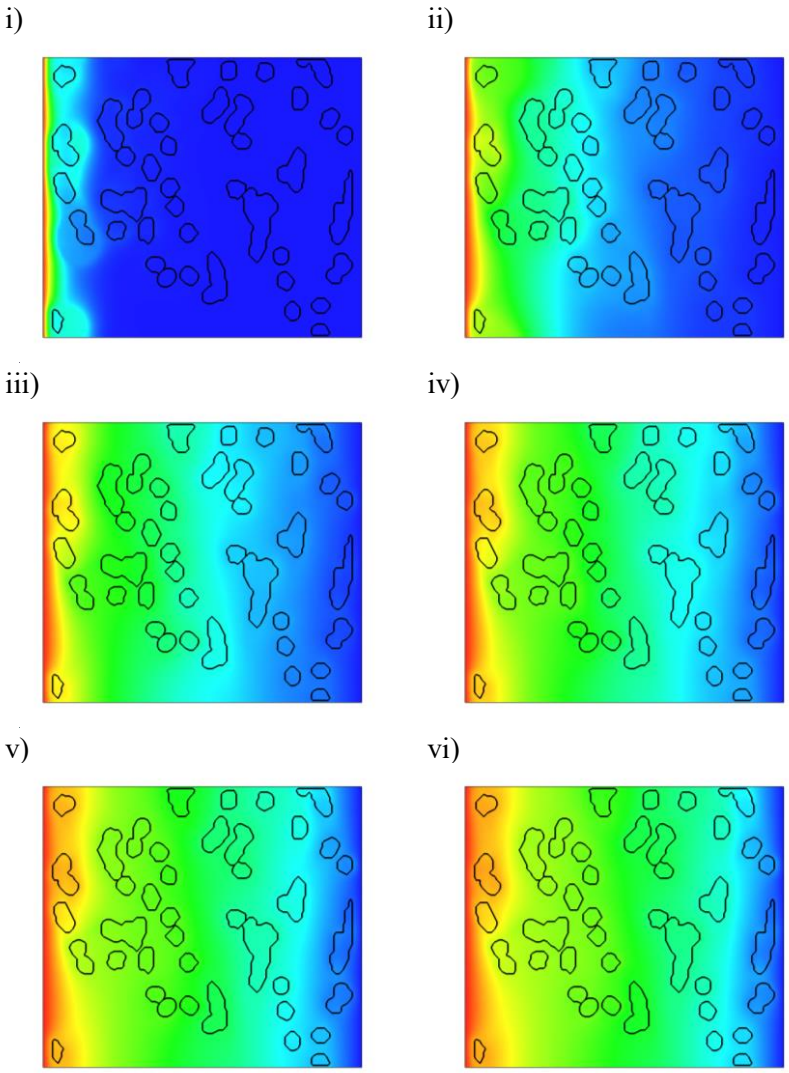

Fig.A17. Temperature distribution of a cross-section of the in-plane in the GDL having $\varphi = \pi/2 \pm 25°$ and $\theta_c = 80°$ ((i) 0.1×10^5 ts, (ii) 1×10^5 ts, (iii) 2×10^5 ts, (iv) 3×10^5 ts, (v) 4×10^5 ts, (vi) 5×10^5 ts)) (10^5 ts indicates 1.25 ms)

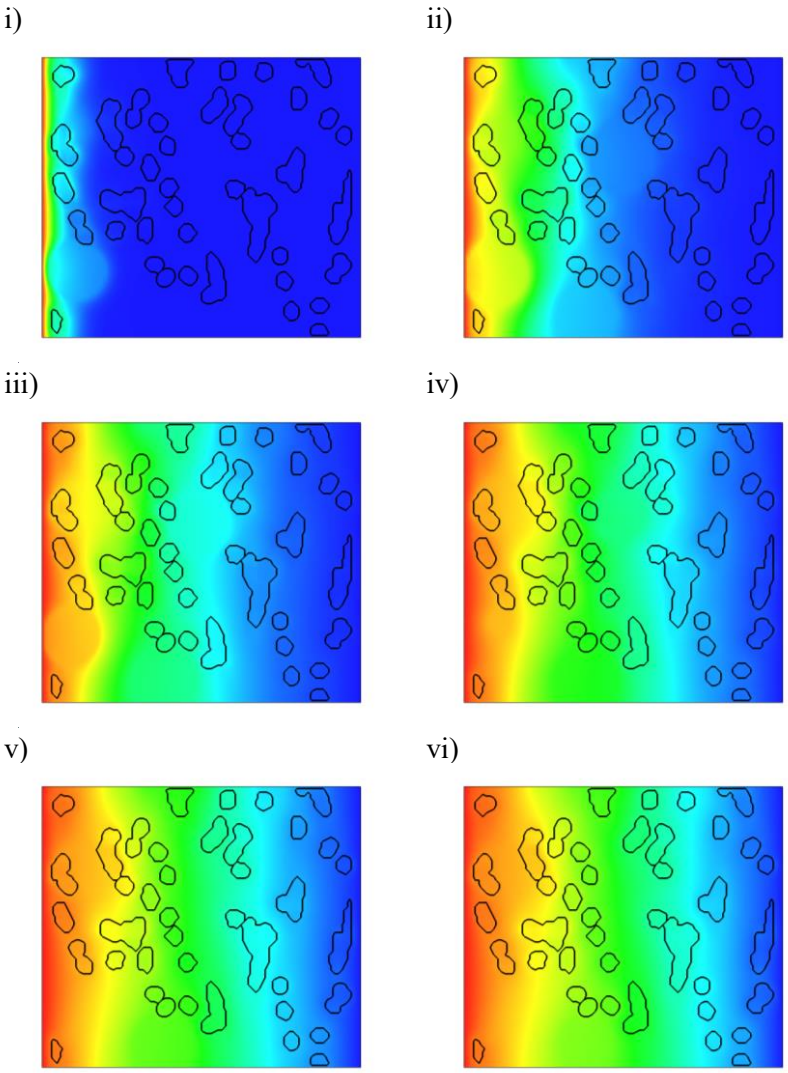

Fig.A18. Temperature distribution of a cross-section of the in-plane in the GDL having $\varphi = \pi/2 \pm 25°$ and $\theta_c = 140°$ ((i) 0.1×10^5 ts, (ii) 1×10^5 ts, (iii) 2×10^5 ts, (iv) 3×10^5 ts, (v) 4×10^5 ts, (vi) 5×10^5 ts)) (10^5 ts indicates 1.25 ms)

References

Banerjee, R., Hinebaugh, J., Liu, H., Yip, R., Ge, N., Bazylak, A. (2016). Heterogeneous porosity distributions of polymer electrolyte membrane fuel cell gas diffusion layer materials with rib-channel compression. *International Journal of Hydrogen Energy* **41**(**33**), 14885–14896.

Bock, R., Shum, A. D., Xiao, X., Karoliussen, H., Seland, F., Zenyuk, I. V., Burheim, O. S. (2018). Thermal Conductivity and Compaction of GDL-MPL interfacial composite material. *Journal of The Electrochemical Society* **165**(**7**), F514.

Burheim, O., Vie, P. J. S., Pharoah, J. G., Kjelstrup, S. (2010). Ex situ measurements of through-plane thermal conductivities in a polymer electrolyte fuel cell. *Journal of Power Sources* **195**(**1**), 249–256.

Bvumbe, T., Bujlo, P., Tolj, I., Mouton, K., Swart, G., Pasupathi, S., Pollet, B. (2016). Review on management, mechanisms and modelling of thermal processes in PEMFC. *Hydrogen and Fuel Cells* **1**, 1–20.

Chen, L., Luan, H.-B., He, Y.-L., Tao, W.-Q. (2012a). Pore-scale flow and mass transport in gas diffusion layer of proton exchange membrane fuel cell with interdigitated flow fields. *International Journal of Thermal Sciences* **51**, 132–144.

Chen, L., Luan, H.-B., He, Y.-L., Tao, W.-Q. (2012b). Numerical investigation of liquid water transport and distribution in porous gas diffusion layer of a proton exchange membrane fuel cell using lattice Boltzmann method. *Russian journal of electrochemistry* **48**(**7**), 712–726.

Chen, L., Luan, H.-B., Tao, W.-Q. (2010). Liquid water dynamic behaviors in the GDL and GC of PEMFCS using lattice Boltzmann method. *Frontiers in Heat and Mass Transfer (FHMT)* **1**(**2**).

Chen, L., Wang, Y.-F., Tao, W.-Q. (2020). Experimental study on the effect of temperature and water content on the thermal conductivity of gas diffusion layers in

proton exchange membrane fuel cell. *Thermal Science and Engineering Progress* **19**, 100616.

Chen, S., Doolen, G. D. (1998). Lattice Boltzmann method for fluid flows. *Annual review of fluid mechanics* **30**(**1**), 329–364.

Chen, W., Jiang, F. (2016). Impact of PTFE content and distribution on liquid–gas flow in PEMFC carbon paper gas distribution layer: 3D lattice Boltzmann simulations. *International journal of hydrogen energy* **41**(**20**), 8550–8562.

Deissler, R. G., Boegli, J. S. (1958). An investigation of effective thermal conductivities of powders in various gases. *Transactions of the American Society of Mechanical Engineers* **80**(**7**), 1417–1423.

Deng, H., Hou, Y., Jiao, K. (2019). Lattice Boltzmann simulation of liquid water transport inside and at interface of gas diffusion and micro-porous layers of PEM fuel cells. *International Journal of Heat and Mass Transfer* **140**, 1074–1090.

Didari, S., Harris, T. A., Huang, W., Tessier, S. M., Wang, Y. (2012). Feasibility of periodic surface models to develop gas diffusion layers: A gas permeability study. *International journal of hydrogen energy* **37**(**19**), 14427–14438.

Eller, J., Roth, J., Marone, F., Stampanoni, M., Büchi, F. N. (2016). Operando properties of gas diffusion layers: saturation and liquid permeability. *Journal of The Electrochemical Society* **164**(**2**), F115.

Fadzillah, D. M., Rosli, M. I., Talib, M. Z. M., Kamarudin, S. K., Daud, W. R. W. (2017). Review on microstructure modelling of a gas diffusion layer for proton exchange membrane fuel cells. *Renewable and sustainable energy reviews* **77**, 1001–1009.

Feng, W., Bhushan, B. (2020). Multistep wettability gradient in bioinspired triangular patterns for water condensation and transport. *Journal of Colloid and Interface Science* **560**, 866–873.

Feser, J. P., Prasad, A. K., Advani, S. G. (2006). On the relative influence of convection in serpentine flow fields of PEM fuel cells. *Journal of Power Sources* **161**(**1**), 404–412.

Froning, D., Brinkmann, J., Reimer, U., Schmidt, V., Lehnert, W., Stolten, D. (2013). 3D analysis, modeling and simulation of transport processes in compressed fibrous microstructures, using the Lattice Boltzmann method. *Electrochimica Acta* **110**, 325–334.

Gao, Y., Jin, T., Wu, X., Zhang, T. (2019). The effect of fiber orientation on stochastic reconstruction and permeability of a carbon paper gas diffusion layer. *Energies* **12**(**14**), 2808.

Gao, Y., Zhang, X., Rama, P., Chen, R., Ostadi, H., Jiang, K. (2013). Lattice Boltzmann simulation of water and gas flow in porous gas diffusion layers in fuel cells reconstructed from micro-tomography. *Computers & Mathematics with Applications* **65**(**6**), 891–900.

Gao, Y., Zhang, X. X., Rama, P., Liu, Y., Chen, R., Ostadi, H., Jiang, K. (2012). Modeling Fluid Flow in the Gas Diffusion Layers in PEMFC Using the Multiple Relaxation-time Lattice Boltzmann Method. *Fuel Cells* **12**(**3**), 365–381.

Gong, S., Cheng, P. (2013). Lattice Boltzmann simulation of periodic bubble nucleation, growth and departure from a heated surface in pool boiling. *International Journal of Heat and Mass Transfer* **64**, 122–132.

Gostick, J. T., Fowler, M. W., Pritzker, M. D., Ioannidis, M. A., Behra, L. M. (2006). In-plane and through-plane gas permeability of carbon fiber electrode backing layers. *Journal of Power sources* **162**(**1**), 228–238.

Gunstensen, A. K., Rothman, D. H., Zaleski, S., Zanetti, G. (1991). Lattice Boltzmann model of immiscible fluids. *Phys. Rev. A* **43**(**8**), 4320–4327.

Hao, L., Cheng, P. (2010). Lattice Boltzmann simulations of water transport in gas diffusion layer of a polymer electrolyte membrane fuel cell. *Journal of Power Sources* **195**(**12**), 3870–3881.

Hao, L., Cheng, P. (2009a). Lattice Boltzmann simulations of anisotropic permeabilities in carbon paper gas diffusion layers. *Journal of Power Sources* **186**(**1**), 104–114.

Hao, L., Cheng, P. (2009b). Lattice Boltzmann simulations of liquid droplet dynamic behavior on a hydrophobic surface of a gas flow channel. *Journal of Power Sources* **190**(**2**), 435–446.

He, X., Luo, L.-S. (1997). Theory of the lattice Boltzmann method: From the Boltzmann equation to the lattice Boltzmann equation. *Phys. Rev. E* **56**(**6**), 6811–6817.

Hinebaugh, J., Bazylak, A. (2017). Stochastic modeling of polymer electrolyte membrane fuel cell gas diffusion layers–Part 1: Physical characterization. *International Journal of Hydrogen Energy* **42**(**24**), 15861–15871.

Hosseinzadeh, E., Rokni, M., Rabbani, A., Mortensen, H. H. (2013). Thermal and water management of low temperature proton exchange membrane fuel cell in fork-lift truck power system. *Applied energy* **104**, 434–444.

Hottinen, T., Mikkola, M., Lund, P. (2004). Evaluation of planar free-breathing polymer electrolyte membrane fuel cell design. *Journal of Power Sources* **129**(**1**), 68–72.

Hou, Y., Deng, H., Zamel, N., Du, Q., Jiao, K. (2020). 3D lattice Boltzmann modeling of droplet motion in PEM fuel cell channel with realistic GDL microstructure and fluid properties. *International Journal of Hydrogen Energy* **45**(**22**), 12476–12488.

Huang, H., Li, Z., Liu, S., Lu, X. (2009). Shan-and-Chen-type multiphase lattice Boltzmann study of viscous coupling effects for two-phase flow in porous media. *International journal for numerical methods in fluids* **61**(**3**), 341–354.

Huang, J., Bao, C., Jiang, Z., Zhang, X. (2019). A general approach of unit conversion system in lattice Boltzmann method and applications for convective heat

transfer in tube banks. *International Journal of Heat and Mass Transfer* **135**, 873–884.

Ikeda, M. K., Rao, P. R., Schaefer, L. A. (2014). A thermal multicomponent lattice Boltzmann model. *Computers & fluids* **101**, 250–262.

Inoue, G., Matsukuma, Y., Minemoto, M. (2006). Effect of gas channel depth on current density distribution of polymer electrolyte fuel cell by numerical analysis including gas flow through gas diffusion layer. *Journal of Power Sources* **157**(**1**), 136–152.

Islam, M. R., Shabani, B., Rosengarten, G., Andrews, J. (2015). The potential of using nanofluids in PEM fuel cell cooling systems: A review. *Renewable and Sustainable Energy Reviews* **48**, 523–539.

Jiao, D., Jiao, K., Du, Q. (2021a). Numerical investigations of vapor condensation and water transport in gas diffusion layers of PEMFC. *International Journal of Heat and Mass Transfer* **177**, 121543.

Jiao, D., Jiao, K., Du, Q. (2021b). Vapor condensation in reconstructed gas diffusion layers of proton exchange membrane fuel cell. *International Journal of Energy Research* **45**(**3**), 4466–4478.

Jithesh, P. K., Bansode, A. S., Sundararajan, T., Das, S. K. (2012). The effect of flow distributors on the liquid water distribution and performance of a PEM fuel cell. *International Journal of Hydrogen Energy*, HySafe 1 **37**(**22**), 17158–17171.

Kakaee, A. H., Molaeimanesh, G. R., Garmaroudi, M. E. (2018). Impact of PTFE distribution across the GDL on the water droplet removal from a PEM fuel cell electrode containing binder. *International Journal of Hydrogen Energy* **43**(**32**), 15481–15491.

Kandlikar, S. G., Garofalo, M. L., Lu, Z. (2011). Water management in a pemfc: water transport mechanism and material degradation in gas diffusion layers. *Fuel Cells* **11**(**6**), 814–823.

Karimi, G., Li, X., Teertstra, P. (2010). Measurement of through-plane effective thermal conductivity and contact resistance in PEM fuel cell diffusion media. *Electrochimica Acta* **55**(**5**), 1619–1625.

Kaviany, M. (2012). Principles of heat transfer in porous media. Springer Science & Business Media.

Ke, X., Duan, Y. (2019). A spatially-varying relaxation parameter Lattice Boltzmann Method (SVRP-LBM) for predicting the effective thermal conductivity of composite material. *Computational Materials Science* **169**, 109080.

Khajeh-Hosseini-Dalasm, N., Fushinobu, K., Okazaki, K. (2010). Phase change in the cathode side of a proton exchange membrane fuel cell. *Journal of Power Sources* **195**(**20**), 7003–7010.

Kim, K. N., Kang, J. H., Lee, S. G., Nam, J. H., Kim, C.-J. (2015). Lattice Boltzmann simulation of liquid water transport in microporous and gas diffusion layers of polymer electrolyte membrane fuel cells. *Journal of Power Sources* **278**, 703–717.

Kiradjiev, K. B., Halvorsen, S. A., Van Gorder, R. A., Howison, S. D. (2019). Maxwell-type models for the effective thermal conductivity of a porous material with radiative transfer in the voids. *International Journal of Thermal Sciences* **145**, 106009.

Kupershtokh, A. L., Medvedev, D. A. (2006). Lattice Boltzmann equation method in electrohydrodynamic problems. *Journal of electrostatics* **64**(**7–9**), 581–585.

Kupershtokh, A. L., Medvedev, D. A., Karpov, D. (2009). On equations of state in a lattice Boltzmann method. *Computers & Mathematics with Applications* **58**(**5**), 965–974.

Ladd, A. J. (1994a). Numerical simulations of particulate suspensions via a discretized Boltzmann equation. Part 1. Theoretical foundation. *Journal of fluid mechanics* **271**, 285–309.

Ladd, A. J. (1994b). Numerical simulations of particulate suspensions via a discretized Boltzmann equation. Part 2. Numerical results. *Journal of fluid mechanics* **271**, 311–339.

Lee, T., Lin, C.-L. (2005). A stable discretization of the lattice Boltzmann equation for simulation of incompressible two-phase flows at high density ratio. *Journal of Computational Physics* **206**(**1**), 16–47.

Lenormand, R. (1990). Liquids in porous media. *J. Phys.: Condens. Matter* **2**(**S**), SA79–SA88.

Li, L., Mei, R., Klausner, J. F. (2017). Lattice Boltzmann models for the convection-diffusion equation: D2Q5 vs D2Q9. *International Journal of Heat and Mass Transfer* **108**, 41–62.

Li, L., Mei, R., Klausner, J. F. (2014). Heat transfer evaluation on curved boundaries in thermal lattice Boltzmann equation method. *Journal of heat transfer* **136**(**1**), 012403.

Li, M., Huber, C., Mu, Y., Tao, W. (2017). Lattice Boltzmann simulation of condensation in the presence of noncondensable gas. *International Journal of Heat and Mass Transfer* **109**, 1004–1013.

Li, Q., Luo, K. H., Li, X. J. (2012). Forcing scheme in pseudopotential lattice Boltzmann model for multiphase flows. *Phys. Rev. E* **86**(**1**), 016709.

Li, W. Q., Qu, Z. G. (2015). Experimental study of effective thermal conductivity of stainless steel fiber felt. *Applied Thermal Engineering* **86**, 119–126.

Liu, C., Qian, R., Liu, Z., Liu, G., Zhang, Y. (2020). Multi-scale modelling of thermal conductivity of phase change material/recycled cement paste incorporated cement-based composite material. *Materials & Design* **191**, 108646.

Liu, H. (2020). The Maxwell crossover and the van der Waals equation of state. *arXiv preprint arXiv:2010.14739*.

Liu, J., Shin, S., Um, S. (2019). Comprehensive statistical analysis of heterogeneous transport characteristics in multifunctional porous gas diffusion layers using lattice Boltzmann method for fuel cell applications. *Renewable Energy* **139**, 279–291.

Liu, W., Wu, C.-Y. (2020). Modelling Complex Particle–Fluid Flow with a Discrete Element Method Coupled with Lattice Boltzmann Methods (DEM-LBM). *ChemEngineering* **4**(**4**), 55.

Lu, J., Kan, A., Zhu, W., Yuan, Y. (2021). Numerical investigation on effective thermal conductivity of fibrous porous medium under vacuum using Lattice-Boltzmann method. *International Journal of Thermal Sciences* **160**, 106682.

Lu, Z., Daino, M. M., Rath, C., Kandlikar, S. G. (2010). Water management studies in PEM fuel cells, part III: Dynamic breakthrough and intermittent drainage characteristics from GDLs with and without MPLs. *International Journal of Hydrogen Energy* **35**(**9**), 4222–4233.

Maxwell, J. C. (1881). A treatise on electricity and magnetism: Pt. III. Magnetism. pt. IV. Electromagnetism. Clarendon press.

Mench, M. M. (2008). Fuel cell engines. John Wiley & Sons.

Mohamad, A. A. (2011). Lattice boltzmann method. Springer.

Molaeimanesh, G. R., Akbari, M. H. (2014). Impact of PTFE distribution on the removal of liquid water from a PEMFC electrode by lattice Boltzmann method. *International journal of hydrogen energy* **39**(**16**), 8401–8409.

Moqaddari, M. R., Shojaeefard, M. H., Molaeimanesh, G. R. (2020). Impact of carbon paper anisotropy on water droplet movement through the electrodes of proton-exchange membrane fuel cells. *Energy & Fuels* **34**(**8**), 10039–10049.

Moriyama, K., Inamuro, T. (2011). Lattice Boltzmann simulations of water transport from the gas diffusion layer to the gas channel in PEFC. *Communications in Computational Physics* **9**(**5**), 1206–1218.

Mortazavi, M., Tajiri, K. (2014). Liquid water breakthrough pressure through gas diffusion layer of proton exchange membrane fuel cell. *international journal of hydrogen energy* **39**(**17**), 9409–9419.

Mukherjee, P. P., Wang, C.-Y., Kang, Q. (2009). Mesoscopic modeling of two-phase behavior and flooding phenomena in polymer electrolyte fuel cells. *Electrochimica Acta* **54**(**27**), 6861–6875.

Nam, J. H., Lee, K.-J., Hwang, G.-S., Kim, C.-J., Kaviany, M. (2009). Microporous layer for water morphology control in PEMFC. *International Journal of Heat and Mass Transfer* **52**(**11**), 2779–2791.

Nazemian, M., Molaeimanesh, G. R. (2020). Impact of carbon paper structural parameters on the performance of a polymer electrolyte fuel cell cathode via lattice Boltzmann method. *Acta Mechanica Sinica* **36**(**2**), 367–380.

Neale, G. H., Nader, W. K. (1973). Prediction of transport processes within porous media: diffusive flow processes within an homogeneous swarm of spherical particles. *AIChE Journal* **19**(**1**), 112–119.

Niu, Z., Wang, Y., Jiao, K., Wu, J. (2018). Two-Phase Flow Dynamics in the Gas Diffusion Layer of Proton Exchange Membrane Fuel Cells: Volume of Fluid Modeling and Comparison with Experiment. *J. Electrochem. Soc.* **165**(**9**), F613–F620.

Omrani, R., Shabani, B. (2017). Gas diffusion layer modifications and treatments for improving the performance of proton exchange membrane fuel cells and electrolysers: A review. *International Journal of Hydrogen Energy* **42**(**47**), 28515–28536.

Ostadi, H., Rama, P., Liu, Y., Chen, R., Zhang, X. X., Jiang, K. (2010). 3D reconstruction of a gas diffusion layer and a microporous layer. *Journal of Membrane Science* **351**(**1–2**), 69–74.

Pfrang, A., Veyret, D., Tsotridis, G. (2011). Computation of thermal conductivity of gas diffusion layers of PEM fuel cells. *Convection and Conduction Heat Transfer* **10**, 232–215.

Pharoah, J. G. (2005). On the permeability of gas diffusion media used in PEM fuel cells. *Journal of Power Sources* **144**(**1**), 77–82.

Pournemat, A., Wilhelm, F., Scholta, J. (2019). Effect of Current Density on the Dynamical Evolution of Liquid Water Distribution within the Gas Diffusion Layers of PEMFC Employing a Multi-Timescale Kinetic Monte Carlo Method. *J. Electrochem. Soc.* **166**(**4**), F334–F342.

Qin, X., Cai, J., Zhou, Y., Kang, Z. (2020). Lattice Boltzmann simulation and fractal analysis of effective thermal conductivity in porous media. *Applied Thermal Engineering* **180**, 115562.

Ramousse, J., Didierjean, S., Lottin, O., Maillet, D. (2008). Estimation of the effective thermal conductivity of carbon felts used as PEMFC Gas Diffusion Layers. *International Journal of Thermal Sciences* **47**(**1**), 1–6.

Ross-Jones, J., Gaedtke, M., Sonnick, S., Rädle, M., Nirschl, H., Krause, M. J. (2019). Conjugate heat transfer through nano scale porous media to optimize vacuum insulation panels with lattice Boltzmann methods. *Computers & Mathematics with Applications* **77**(**1**), 209–221.

Sadeghifar, H., Djilali, N., Bahrami, M. (2014). Effect of Polytetrafluoroethylene (PTFE) and micro porous layer (MPL) on thermal conductivity of fuel cell gas diffusion layers: Modeling and experiments. *Journal of Power Sources* **248**, 632–641.

Sakaida, S., Tabe, Y., Chikahisa, T. (2017). Large scale simulation of liquid water transport in a gas diffusion layer of polymer electrolyte membrane fuel cells using the lattice Boltzmann method. *Journal of Power Sources* **361**, 133–143.

Satjaritanun, P., Hirano, S., Shum, A. D., Zenyuk, I. V., Weber, A. Z., Weidner, J. W., Shimpalee, S. (2018). Fundamental Understanding of Water Movement in Gas

Diffusion Layer under Different Arrangements Using Combination of Direct Modeling and Experimental Visualization. *J. Electrochem. Soc.* **165**(**13**), F1115–F1126.

Satjaritanun, P., Weidner, J. W., Hirano, S., Lu, Z., Khunatorn, Y., Ogawa, S., Litster, S. E., Shum, A. D., Zenyuk, I. V., Shimpalee, S. (2017). Micro-Scale Analysis of Liquid Water Breakthrough inside Gas Diffusion Layer for PEMFC Using X-ray Computed Tomography and Lattice Boltzmann Method. *J. Electrochem. Soc.* **164**(**11**), E3359–E3371.

Schladitz, K., Peters, S., Reinel-Bitzer, D., Wiegmann, A., Ohser, J. (2006). Design of acoustic trim based on geometric modeling and flow simulation for non-woven. *Computational Materials Science* **38**(**1**), 56–66.

Schulz, V. P., Becker, J., Wiegmann, A., Mukherjee, P. P., Wang, C.-Y. (2007). Modeling of two-phase behavior in the gas diffusion medium of PEFCs via full morphology approach. *Journal of the Electrochemical Society* **154**(**4**), B419.

Shan, X. (1997). Simulation of Rayleigh-Bénard convection using a lattice Boltzmann method. *Phys. Rev. E* **55**(**3**), 2780–2788.

Shan, X., Chen, H. (1994). Simulation of nonideal gases and liquid-gas phase transitions by the lattice Boltzmann equation. *Physical Review E* **49**(**4**), 2941.

Shan, X., Chen, H. (1993). Lattice Boltzmann model for simulating flows with multiple phases and components. *Phys. Rev. E* **47**(**3**), 1815–1819.

Shen, L. Y., Tang, G. H., Li, Q., Shi, Y. (2019). Hybrid wettability-induced heat transfer enhancement for condensation with noncondensable gas. *Langmuir* **35**(**29**), 9430–9440.

Shojaeefard, M. H., Molaeimanesh, G. R., Nazemian, M., Moqaddari, M. R. (2016). A review on microstructure reconstruction of PEM fuel cells porous electrodes for pore scale simulation. *International Journal of Hydrogen Energy* **41**(**44**), 20276–20293.

Shum, A. D., Parkinson, D. Y., Xiao, X., Weber, A. Z., Burheim, O. S., Zenyuk, I. V. (2017). Investigating phase-change-induced flow in gas diffusion layers in fuel cells with X-ray computed tomography. *Electrochimica Acta* **256**, 279–290.

Sinha, P. K., Wang, C.-Y. (2007). Pore-network modeling of liquid water transport in gas diffusion layer of a polymer electrolyte fuel cell. *Electrochimica Acta* **52**(**28**), 7936–7945.

Stiles, C. D., Xue, Y. (2016). High density ratio lattice Boltzmann method simulations of multicomponent multiphase transport of H2O in air. *Computers & Fluids* **131**, 81–90.

Sukop, M. C. (2006). DT Thorne, Jr. Lattice Boltzmann Modeling Lattice Boltzmann Modeling.

Swift, M. R., Orlandini, E., Osborn, W. R., Yeomans, J. M. (1996). Lattice Boltzmann simulations of liquid-gas and binary fluid systems. *Phys. Rev. E* **54**(**5**), 5041–5052.

Tabe, Y., Lee, Y., Chikahisa, T., Kozakai, M. (2009). Numerical simulation of liquid water and gas flow in a channel and a simplified gas diffusion layer model of polymer electrolyte membrane fuel cells using the lattice Boltzmann method. *Journal of Power Sources* **193**(**1**), 24–31.

Tahir, M. A., Vahedi Tafreshi, H. (2009). Influence of fiber orientation on the transverse permeability of fibrous media. *Physics of Fluids* **21**(**8**), 083604.

Tayarani-Yoosefabadi, Z., Harvey, D., Bellerive, J., Kjeang, E. (2016). Stochastic microstructural modeling of fuel cell gas diffusion layers and numerical determination of transport properties in different liquid water saturation levels. *Journal of Power Sources* **303**, 208–221.

Teertstra, P., Karimi, G., Li, X. (2011). Measurement of in-plane effective thermal conductivity in PEM fuel cell diffusion media. *Electrochimica Acta* **56**(**3**), 1670–1675.

Thiedmann, R., Fleischer, F., Hartnig, C., Lehnert, W., Schmidt, V. (2008). Stochastic 3D modeling of the GDL structure in PEMFCs based on thin section detection. *Journal of the Electrochemical Society* **155**(**4**), B391.

Wang, D., Shen, J., Liu, Z., Liu, W. (2014). Simulation of Multiphase Flow and Heat Transfer in Porous Media Using Lattice Boltzmann Method.

Wang, N., Kaur, I., Singh, P., Li, L. (2021). Prediction of effective thermal conductivity of porous lattice structures and validation with additively manufactured metal foams. *Applied Thermal Engineering* **187**, 116558.

White, R. T., Eberhardt, S. H., Singh, Y., Haddow, T., Dutta, M., Orfino, F. P., Kjeang, E. (2019). Four-dimensional joint visualization of electrode degradation and liquid water distribution inside operating polymer electrolyte fuel cells. *Sci Rep* **9**(**1**), 1843.

Wu, H.-W., Shih, G.-J., Chen, Y.-B. (2018). Effect of operational parameters on transport and performance of a PEM fuel cell with the best protrusive gas diffusion layer arrangement. *Applied Energy* **220**, 47–58.

Xu, G., LaManna, J. M., Clement, J. T., Mench, M. M. (2014). Direct measurement of through-plane thermal conductivity of partially saturated fuel cell diffusion media. *Journal of Power Sources* **256**, 212–219.

Yablecki, J., Hinebaugh, J., Bazylak, A. (2012a). Effect of liquid water presence on PEMFC GDL effective thermal conductivity. *Journal of The Electrochemical Society* **159**(**12**), F805.

Yablecki, J., Nabovati, A., Bazylak, A. (2012b). Modeling the effective thermal conductivity of an anisotropic gas diffusion layer in a polymer electrolyte membrane fuel cell. *Journal of The Electrochemical Society* **159**(**6**), B647.

Yiotis, A. G., Kainourgiakis, M. E., Charalambopoulou, G. C., Stubos, A. K. (2016). Microscale characterisation of stochastically reconstructed carbon fiber-based Gas Diffusion Layers; effects of anisotropy and resin content. *Journal of Power Sources* **320**, 153–167.

Yu, J., Froning, D., Reimer, U., Lehnert, W. (2018). Apparent contact angles of liquid water droplet breaking through a gas diffusion layer of polymer electrolyte membrane fuel cell. *International Journal of Hydrogen Energy* **43**(**12**), 6318–6330.

Zamel, N., Litovsky, E., Li, X., Kleiman, J. (2011a). Measurement of the through-plane thermal conductivity of carbon paper diffusion media for the temperature range from- 50 to+ 120° C. *international journal of hydrogen energy* **36**(**19**), 12618–12625.

Zamel, N., Litovsky, E., Shakhshir, S., Li, X., Kleiman, J. (2011b). Measurement of in-plane thermal conductivity of carbon paper diffusion media in the temperature range of- 20° C to+ 120° C. *Applied energy* **88**(**9**), 3042–3050.

Zenyuk, I. V., Parkinson, D. Y., Connolly, L. G., Weber, A. Z. (2016). Gas-diffusion-layer structural properties under compression via X-ray tomography. *Journal of Power Sources* **328**, 364–376.

Zenyuk, I. V., Parkinson, D. Y., Hwang, G., Weber, A. Z. (2015). Probing water distribution in compressed fuel-cell gas-diffusion layers using X-ray computed tomography. *Electrochemistry Communications* **53**, 24–28.

Zhang, C., Cheng, P. (2017). Mesoscale simulations of boiling curves and boiling hysteresis under constant wall temperature and constant heat flux conditions. *International Journal of Heat and Mass Transfer* **110**, 319–329.

Zhang, C., Cheng, P., Minkowycz, W. J. (2017). Lattice Boltzmann simulation of forced condensation flow on a horizontal cold surface in the presence of a non-condensable gas. *International Journal of Heat and Mass Transfer* **115**, 500–512.

Zhang, D., Li, S., Li, Y., Mei, N., Pu, H., Jiao, S. (2020). Numerical investigation on the mechanism of multicomponent boiling in porous media using lbm at pore scale. *ES Energy & Environment* **12**(**2**), 108–116.

Zhang, X.-M., Zhang, X.-X. (2014). Impact of Compression on Effective Thermal Conductivity and Diffusion Coefficient of Woven Gas Diffusion Layers in Polymer Electrolyte Fuel Cells. *Fuel Cells* **14**(2), 303–311.

Zhu, W., Wang, M., Chen, H. (2017). Study on multicomponent pseudo-potential model with large density ratio and heat transfer. *International Communications in Heat and Mass Transfer* **87**, 183–191.

Ziegler, C., Gerteisen, D. (2009). Validity of two-phase polymer electrolyte membrane fuel cell models with respect to the gas diffusion layer. *Journal of Power Sources* **188**(**1**), 184–191.

요 약 문

격자 볼츠만 법을 이용한
고분자 전해질막 연료전지의 기체확산층의
열 및 물질 전달 특성에 대한 수치해석

고분자 전해질막 연료전지(PEMFC)는 친환경적이고, 높은 효율과 높은 출력밀도를 띠며, 작동 온도 또한 상대적으로 낮다는 장점을 갖는다. 이러한 장점으로 인해 PEMFC 는 운송수단 및 고정식 발전소 그리고 휴대용 전력과 같이 많은 응용 분야에서 가장 촉망받는 대체 에너지원으로 각광받고 있다. 지난 수십 년 동안 PEMFC 성능을 개선하기 위한 연구가 수행되었으며, 셀 성능을 향상하고 효율적인 셀 작동을 위해선 각 셀 구성요소에서 발생하는 전기화학적 현상을 이해하는 것이 필수적이다.

셀 작동 중 전기화학반응으로 발생하는 수증기와 열은 기체확산층(GDL)을 통해 기체 채널(GC)로 빠져나가기 때문에 셀 구성요소 중에서 GDL 은 PEMFC 의 성능을 좌우하는 매우 중요한 요소라 할 수 있다. 과도하게 생성된 수분은 GDL 를 침수시켜 PEMFC 성능에 악영향을 미치며, 과열된 온도는 탈수를 유발하여 성능저하를 일으킨다. 반대로 건조한 상태는 이온 전도도의 효율을 낮추며, 낮은 온도는 반응 속도를 느리게 하고 포화압력을 낮추어 수증기 응결을 유발한다. 따라서, PEMFC 의 더 나은 성능과 효율을 얻기 위해선 GDL 내부의 적절한 열 및 수분 관리가 필요하다.

본 논문에서는 GDL 의 물질전달 특성을 분석하기 위해 다성분 다상(MCMP) 격자 볼츠만법(LBM)을 이용하여 GDL 내부로의 액상수분의 침입 과정을 연구하였다. 이방성 특징을 띠는 GDL 의 형상학적 특성을 고려하기위해 확률적 재생성 방법으로 재구성된 3 차원 형상이 적용되었으며, 투과율 해석을 통해 재구성된 GDL 형상에 대한 이방성 특징을 검증하였다. 총 네 가지의 섬유 극각범위를 채택하여 액상수분 전달에 대한 탄소 섬유 배향의 영향을 규명하였고, 탄소

섬유에 대한 젖음성은 소수성 물질로 균일하게 도포된 상태로 가정되어 140°의 접촉각이 적용되었다.

액상수분의 침투 패턴은 소수성 젖음성으로 인해 모세관 핑거링(capillary fingering)의 유동 형태를 나타냈으며, GDL 내부에 형성되는 액상수분의 동적 거동과 평균 수분 포화도는 모든 조건에서 거의 유사하게 나타났다. 탄소 섬유의 극각을 제외한 나머지 형상학적 조건과 젖음성은 동일하기 때문에, 액상 침투과정에서 형성되는 주류는 통과면(through-plane) 방향의 모세관압 차이에 더 큰 영향을 받는 것으로 분석되었다. 이와 함께 액상수분이 GDL 을 통과한 이후 GDL 표면에 형성하는 액상수분 물방울의 겉보기 각도를 측정하였다. 모든 경우에서 섬유에 적용된 접촉각보다 낮은 각도로 겉보기 각도가 형성되는 것을 관찰하였고, 이는 섬유 배향에 따라 형성되는 GDL 탄소섬유의 표면 변화에 의한 영향으로 분석되었다.

더불어 본 논문에서는 GDL 의 열전달 특성을 파악하기위해 유효 열전도율(ETC)을 조사하였으며, 이와 함께 ETC 에 대한 액상수분 함량의 영향을 함께 분석하였다. 열전달과 유동현상을 동시에 해석하기 위해 열해석모델과 유동해석모델이 양방향으로 결합된 MCMP LBM 모델을 개발하였다. 열해석에서도 3 차원 GDL 형상이 적용되었으며, GDL 의 건조한 상태와 습윤한 상태에 대해 각각 조사되었다. 추가적으로 습윤한 상태에 대해선 친수성의 접촉각 80°와 소수성의 접촉각 140°가 적용되었다.

본 논문은 열전도에 따른 온도 분포와 물 성분의 응집 및 분리현상의 시간적 변화를 제시하며, GDL 의 ETC 는 GDL 내부에 형성되는 액상수분 함량과 분포에 많은 영향을 받는 것을 확인하였다. 또한, 초기 물성분의 질량분율이 높을수록 GDL 의 액상수분 함량이 증가하였다. 액상수분 방울은 탄소 섬유 사이를 연결하는 바인더 역할을 하는 것을 관찰하였으며, 액상수분의 전도도는 공기의 전도도보다 높기 때문에 액상 수분이 더 많이 분포될수록 높은 ETC 값을 띠는 것으로 분석되었다. 탄소 섬유의 젖음성이 동일한 경우 GDL 내부의 액상수분 함량은 유사하였으며, 절대적인 액상수분의 함량보다 액상수분의

분포도가 GDL 의 ETC 를 결정하는 데 더 중요한 역할을 하는 것을 규명하였다.

마지막으로 본 논문은 섬유 배향을 고려하여 재구성된 3 차원 GDL 형상을 적용하여 종래의 2 차원 형상에서 확인할 수 없었던 GDL 의 물질 전달의 이방성 특징을 잘 나타내고 있으며, GDL 내부의 형상학적 조건이외에 GC 와 GDL 의 경계면의 탄소섬유 형상에 대한 중요성 또한 제시한다. 이와 더불어 본 논문은 GDL 의 열전달 과정 해석에서 온도변화에 따른 액상수분의 상변화는 고려하지 않지만, 이에 준하는 액상수분의 상분리 현상을 포함하고 있다. 이에 따라 본 논문에서 개발된 해석모델은 기존의 MCMP LBM 모델에서 할 수 없었던 다성분에서의 열해석과 유체의 상분리 해석을 동시에 수행할 수 있는 framework 을 제공한다.

주요어 : 고분자 전해질막 연료전지; 기체 확산층; 격자 볼츠만 법; 다성분 다상 모델; 탄소 섬유 배향; 액상 수분 전달; 유효 열전도율; 상분리

학 번 : 2014-21840